

UNIVERSITÀ
DI PAVIA

UNIVERSITY OF PAVIA
FACULTY OF ENGINEERING
DEPARTMENT OF ELECTRICAL, COMPUTER AND BIOMEDICAL ENGINEERING

MASTER'S DEGREE IN ELECTRICAL ENGINEERING

MASTER THESIS

# BIBLIOGRAPHIC REVIEW IN THE PHOTOVOLTAIC SECTOR WITH PARTICULAR ATTENTION TO DC-DC CONVERTERS AND THE MOST RECENT MAXIMUM POWER POINT TRACKING ALGORITHM AVAILABLE IN THE LITERATURE

Candidate:
Mehdi Alizadeh

Supervisor:
Prof. Lucia Frosini

Co-supervisor:
Dr. Lorenzo Mantione

A.Y. 2025/2026

# Abstract

Photovoltaic (PV) generation has become the largest single source of new electricity-generating capacity worldwide, yet a photovoltaic generator has no intrinsic mechanism for operating at its point of maximum power: that point moves continuously with irradiance and temperature and, under partial shading, splits into several local maxima of which only one is global. Extracting the power actually available under these conditions is the joint task of a DC–DC converter, which acts as the actuator of the system, and a Maximum Power Point Tracking (MPPT) algorithm, which commands it. This thesis provides a structured, critical bibliographic review of both bodies of literature. Chapter 1 establishes the photovoltaic and control-theoretic background: the physics of the photovoltaic effect, the single- and double-diode equivalent-circuit models, the electrical characteristics of the generator, and the environmental and shading conditions that make tracking necessary. Chapter 2 surveys DC–DC converter topologies for photovoltaic applications, from the classical non-isolated converters through the high step-up families developed to overcome the classical boost converter's voltage-gain ceiling, and develops a set of converter-selection criteria that include the converter's behaviour as the actuator of a control loop. Chapter 3, the central chapter of the thesis, surveys the state of the art in MPPT algorithms: the classical perturb-and-observe and incremental-conductance methods and their refinements; the advanced and intelligent methods based on fuzzy logic, artificial neural networks and metaheuristic optimisation; and the most recent techniques reported in the literature, including hybrid two-stage architectures, machine-learning and reinforcement-learning approaches, model predictive control, and sliding-mode control. Chapter 4 brings the two surveys together in a comparative and critical discussion, arguing - on evidence drawn from studies that vary the converter and the algorithm jointly - that the converter and the tracking algorithm are best understood, and where possible selected, as a single co-designed system rather than as two independently optimised components, and closes with the directions the recent literature suggests for future work.

**Keywords:** photovoltaic systems; DC–DC converters; Maximum Power Point Tracking; MPPT algorithms; perturb and observe; incremental conductance; metaheuristic optimisation; machine learning; model predictive control; sliding-mode control.

# Table of Contents

1 CHAPTER 1 - INTRODUCTION AND PHOTOVOLTAIC SYSTEMS ..... 18
1.1 Motivation and Background ..... 18
1.2 The Photovoltaic Effect and the Solar Cell ..... 20
1.2.1 Physical mechanism ..... 20
1.2.2 From cell to module to array ..... 21
1.3 Equivalent-Circuit Model of the PV Generator ..... 22
1.3.1 The single-diode model ..... 23
1.3.2 The double-diode model and model choice as an experimental variable ..... 24
1.4 Electrical Characteristics of the PV Generator ..... 25
1.5 Environmental Dependence and the Need for Tracking ..... 27
1.5.1 Irradiance and temperature ..... 27
1.5.2 The maximum power point as a moving target ..... 29
1.5.3 Partial shading and the multi-peak characteristic ..... 30
1.6 Photovoltaic System Configurations ..... 33
1.7 The Role of Power Electronics: the Converter as Actuator ..... 35
1.8 Scope and Objectives of the Thesis ..... 37
1.9 Organisation of the Thesis ..... 38
2 CHAPTER 2 - DC-DC CONVERTERS FOR PHOTOVOLTAIC APPLICATIONS ..... 39
2.1 Classification and Analytical Toolkit ..... 39
2.1.1 The isolation and switching-regime axes ..... 39
2.1.2 Steady-state balance, gain laws and the conduction-mode boundary ..... 42
2.2 Non-Isolated Converter Topologies ..... 45
2.3 Isolated Converter Topologies ..... 50
2.4 High Step-Up Non-Isolated Converters ..... 54
2.4.1 Motivation and boosting techniques ..... 54
2.4.2 Combined structures and the photovoltaic reading ..... 58

2.4.3 Cost and Reliability Economics ..... 60
2.5 Converter Selection Criteria ..... 61
2.5.1 Power-processing criteria ..... 61
2.5.2 The converter as MPPT actuator: seven additional criteria ..... 62
2.6 Interaction Between the Converter and the MPPT Controller ..... 63
3 CHAPTER 3 - MAXIMUM POWER POINT TRACKING: STATE OF THE ART ..... 67
3.1 The Maximum Power Point as a Tracking Problem ..... 67
3.1.1 MPPT as real-time optimisation ..... 67
3.1.2 Performance criteria ..... 68
3.1.3 Mathematical Background ..... 69
3.2 Conventional MPPT Algorithms ..... 70
3.2.1 Perturb and Observe (P&O) ..... 70
3.2.2 Incremental Conductance (INC) ..... 74
3.2.3 Constant-Voltage and Constant-Current Methods ..... 76
3.2.4 Fractional Open-Circuit Voltage and Short-Circuit Current ..... 77
3.2.5 Comparative summary of conventional methods ..... 79
3.2.6 Sensing and Practical Implementation Considerations ..... 81
3.3 Advanced and Intelligent MPPT Algorithms ..... 83
3.3.1 Fuzzy Logic Control ..... 83
3.3.2 Artificial Neural Networks and Neuro-Fuzzy Methods ..... 85
3.3.3 Metaheuristic and Optimisation-Based Methods ..... 87
3.4 Most Recent MPPT Algorithms in the Literature ..... 91
3.4.1 Hybrid MPPT Algorithms ..... 92
3.4.2 Machine Learning and Deep Learning-Based MPPT ..... 95
3.4.3 Reinforcement Learning Approaches ..... 97
3.4.4 Model Predictive Control ..... 99
3.4.5 Sliding-Mode Control ..... 101

3.4.6 Case Study: Pelican Optimisation Algorithm on a High-Gain Converter ..... 106
3.4.7 Computational Platforms Across the Surveyed Families ..... 111
3.5 Synthesis: MPPT Performance Under Key Operating Conditions ..... 112
4 CHAPTER 4 - COMPARATIVE ANALYSIS, DISCUSSION AND CONCLUSIONS ..... 116
4.1 Comparative Analysis of MPPT Algorithms ..... 116
4.2 Converter Topology and MPPT Implementation ..... 118
4.3 Critical Discussion ..... 121
4.3.1 Which approaches perform well, and under what conditions ..... 121
4.3.2 Limitations of conventional methods and the value added by advanced methods ..... 122
4.3.3 Trade-offs between performance and computational complexity ..... 122
4.3.4 Suitability for practical applications ..... 122
4.3.5 Unresolved challenges ..... 123
4.3.6 Evidence Quality in the Most Recent Literature ..... 124
4.3.7 Answering the Thesis Objective ..... 125
4.4 Future Perspectives ..... 125
4.5 Conclusions ..... 127
4.6 Recommendations for Future Research ..... 129

# List of Figures

Figure 1-1: The three deployment contexts contrasted in this section, which rarely share the same power-electronic architecture, and two of the components that distinguish them: (a) a residential rooftop array on a private house in Los Angeles [104]; (b) a commercial rooftop installation on a storage facility in Gilroy, California [105]; (c) part of the 15 MW utility-scale plant at Nellis Air Force Base, Nevada, comprising approximately 70,000 modules [106]; (d) a 1 MW / 4 MWh containerized battery energy storage system in Pullman, Washington [107]; (e) a commercial all-in-one off-grid hybrid inverter (MPP Solar LV2424-MSD), which combines a built-in MPPT solar charger, a battery charger and an inverter in one enclosure [108, 109] ..... 19

Figure 1-2: Physical realization of the cell–module–string–array hierarchy: (a) close-up of the series-interconnected cells of a polycrystalline module (photograph by G. Vellut, CC BY 2.0) [110]; (b) schematic of the internal interconnection of standard modules: left, a single string of 36 cells in series; right, two sub-matrices in parallel, each of 60 half-cut cells in series (C. Domínguez, CC BY-SA 4.0) [111]; (c) a 67 kW array at the Mesa Verde Visitor and Research Center, Colorado, formed by 286 modules of 235 W wired as 22 parallel strings of 13 series-connected modules (photograph by D. Schroeder/NREL, Public Domain Mark 1.0) [112] ..... 21

Figure 1-3: Single-diode equivalent-circuit model of a photovoltaic cell/module: a light-generated current source in parallel with a diode, a shunt resistance $R_p$, and a series resistance $R_s$ [13], [15] ..... 23

Figure 1-4: Double-diode equivalent-circuit model of a photovoltaic cell. The second diode $D_2$, in parallel with $D_1$, represents recombination in the depletion region, which a single diode cannot reproduce at low voltage and low irradiance. $I_{ph}$ is the light-generated current, $R_s$ the series resistance and $R_p$ the shunt resistance [15], [16] ..... 25

Figure 1-5: Current–voltage (I–V) and power–voltage (P–V) characteristics of the photovoltaic module of Table 1-3 at Standard Test Conditions, computed from the single-diode model of equation (1.2) [13], [15].. ..... 26

Figure 1-6: Effect of irradiance on the power–voltage characteristic of the module of Table 1-3 at a fixed cell temperature of 25 °C; markers indicate the maximum power point of each curve [13], [15] ..... 28

Figure 1-7: Effect of cell temperature on the current–voltage characteristic of the module of Table 1-3 at a fixed irradiance of 1000 W/m² [13], [15], [11] ..... 29

Figure 1-8: Temperature distribution in a locally shaded crystalline-silicon module at an irradiance of 750 W/m² with half of one cell shaded (shading ratio R = 1/2), obtained by thermal simulation and validated against infrared measurements. The module map (top left) marks two line scans, whose temperature profiles are plotted along the module length (right) and across the row containing the shaded cell (bottom left), each with its three-dimensional cross-section. The unshaded part of the shaded cell forms a hot spot of 77.66 °C, about 22.5 °C ($\Delta T_2$) above the surrounding cells, while the shaded part forms a cold spot about 7.5 °C ($\Delta T_1$) below them. Reproduced from [113], Fig. 5. ..... 31
Figure 1-9: (a) Power–voltage characteristic of a string of three series-connected modules of the type in Table 1-3, each protected by a bypass diode, under irradiances of 1000, 600 and 300 W/m², compared with the uniformly illuminated case. Three local maxima appear; the global maximum lies at the central peak [13], [15]; bypass-diode behaviour as described in [20-23]. (b) The same multi-peak characteristic as reported for a partially shaded array, with two local peaks and the global peak; (reproduced from [122], Fig. 2.) ..... 31
Figure 1-10: Circuit schemes of the two grid-connected architectures. (a) Single-stage: the array feeds the inverter bridge S1–S4 directly, the input capacitor Cpv also acting as the DC link, so one controller must perform maximum power point tracking and grid-current regulation simultaneously [11]. (b) Two-stage: a boost converter (L, S, D) tracks the array and charges the DC-link capacitor Cdc, from which the inverter operates; the link capacitor decouples the tracking problem from grid-current control, and each stage carries its own controller [28, 29]. Lf is the grid-side filter inductance. ..... 31
Figure 1-11: Two-stage photovoltaic conversion chain, showing the DC–DC converter as the actuator through which the MPPT controller imposes the operating point of the array.[32, 33] ..... 36
Figure 2-1: The isolation axis illustrated on the same conversion function. (a) Inverting buck–boost converter without isolation: input and output share a single return path, and the gain $|M| = D/(1 - D)$ is set by the duty cycle alone [31], [33], [119]. (b) Its isolated counterpart, the flyback converter, in which the inductor becomes a coupled inductor with turns ratio 1 : n: the isolation barrier separates the primary and secondary grounds, the gain $M = nD/(1 - D)$ acquires the duty-cycle-independent factor n, and the leakage inductance Llk requires a clamp (Dc, Cc, Rc) to absorb the voltage spike at switch turn-off [31], [34], [115]. ..... 40
Figure 2-2: The switching-regime axis illustrated on three complete converters, each with the commutation waveforms reported for it [34, 37]. (a) Hard switching in a boost converter [116]: at turn-off the switch voltage vA rises to Vo while the current iA is still flowing, and at turn-on the

current, including the reverse-recovery charge Qr of D1, rises while the voltage is still high; the shaded overlap pA = vAiA is the energy lost per commutation. (b) Zero-voltage switching in a buck quasi-resonant converter [117]: Cr in parallel with S slows the voltage rise at turn-off, the Lr–Cr resonance returns vCr to zero, and S is turned on while its antiparallel diode D1 conducts, that is, at zero voltage; the peak switch voltage is VS + Z0Io. (c) Zero-current switching in a half-wave L-type buck quasi-resonant converter (QRC) [118]: Lr in series with Q1 limits the current slope at turn-on, the resonance with Cr returns iLr to zero, and the series diode D1 blocks reverse current, so that Q1 is turned off at zero current. Waveforms are qualitative and not to scale .....41
Figure 2-3: Circuit diagrams of the basic non-isolated converters in a common notation, with source and load: (a) buck, (b) boost, (c) inverting buck–boost, (d) Ćuk, (e) SEPIC and (f) Zeta. S: switch; D: diode; L, L1, L2: inductors; C1: energy-transfer capacitor; Co: output capacitor; R: load. Drawn by the author; SEPIC and Zeta topologies as in [100], Ćuk topology as in [17]. Buck, boost and buck–boost topologies as in [28, 33] .....47
Figure 2-4: Photovoltaic-fed zero-voltage-switching (ZVS) Zeta converter with its MPPT control loop: the MPPT algorithm (P&O or INC) processes the measured array voltage and current and sets the duty cycle $D$ of switch S; $L_r$, $C_r$ and $D_r$ form the resonant network that provides zero-voltage turn-on [100].....47
Figure 2-5: Solar-fed zero-voltage-switching (ZVS) SEPIC converter with its MPPT control loop: the measured array voltage and current feed the MPPT algorithm, which sets the duty cycle of switch S; the capacitor $C_r$ and the diode connected in parallel with S, together with the inductor $L_r$ in series with it, provide zero-voltage switching [100], Fig. 2(b).....48
Figure 2-6: Active-clamp flyback converter. (a) [120], Fig. 3: the clamp branch formed by the auxiliary switch $S_c$ and the clamp capacitor $C_c$, operated complementarily to the main switch S, recovers the energy stored in the leakage inductance $L_{lk}$ instead of dissipating it in a resistive snubber; $L_m$ is the magnetizing inductance, and both switches are shown with their body diodes. (b) Qualitative waveforms over two switching periods, [120]: complementary gate signals with dead time; the primary current $i_{Lk}$, which rises linearly while S conducts and, during the off interval, resonates with $C_c$ through zero to a negative value, so that the body diode of S conducts before S is turned on, at zero voltage; and the switch voltage $v_S$, clamped at $V_{in} + V_o/n$, compared with the unclamped turn-off spike and ringing (dashed) [29, 34].....48
Figure 2-7: (a) A flyback DC–DC stage with MPPT feeds a single-phase full-bridge inverter; the energy buffer can be placed at the module (Cdec) or at a regulated intermediate DC link (Cdc). (b) Instantaneous power delivered to a single-phase grid at unity power factor, $p_{ac}(t) = P(1 - \cos 2\omega t)$, which pulsates at twice the line frequency around the constant power Ppv extracted from the

module; the buffer stores the difference in the hatched intervals and releases it in the shaded ones. (c) A commercial module-level microinverter (Enphase M190) mounted on the racking rail, with the frame grounding conductor attached, before the PV module is placed over it [114]. Panels (a) and (b) [29, 34]. ..... 52
Figure 2-8: Two-stage isolated converter with a resonant output stage, adapted from [121], Fig. 1, with the photovoltaic module in place of the rectified AC input: the boost stage (L, S, D) regulates the intermediate capacitor C, so that the half-bridge (S1, S2) and the LLC tank (Lr, Cr, Lm) can operate close to the resonant frequency fr = 1/(2π√(LrCr)); during each dead time the resonant current discharges the output capacitance CS1 or CS2 of the incoming switch, whose body diode DS1 or DS2 then conducts, so that the switches turn on at zero voltage; the centre-tapped secondary of the transformer T is rectified by Do1 and Do2 ..... 53
Figure 2-9: Various topology configurations of Voltage Multiplier Cells (VMCs), (a)–(f), built from diodes D and capacitors C, with an inductor L in (c), (e) and (f) and an auxiliary switch S in (d) [35, 52]. ..... 52
Figure 2-10: Representative circuits of five high step-up techniques, drawn by the author: (a) interleaved two-phase boost, whose ideal gain remains M = 1/(1 − D); (b) coupled-inductor boost, in which the second winding N2 raises the gain according to the turns ratio N2/N1; (c) switched-capacitor (charge-pump) doubler, in which the flying capacitor Cf is charged in parallel with the source through S1 and S3 and discharged in series with it through S2 and S4, ideally doubling the input voltage at a fixed ratio; (d) switched-inductor boost, with L1 and L2 charged in parallel and discharged in series, M = (1 + D)/(1 − D); (e) two cascaded boost stages, M = 1/(1 − D)2 [34, 53] (a), [34, 38, 39] (b), [54] (c, d) and [34, 55] (e) ..... 56
Figure 2-11: Generalized schematic of a DC-DC boost converter equipped with a Voltage Lift (VL) cell, inserted between the switch node and the output diode [35, 52]. ..... 55
Figure 2-12: Variations in VL cell topology: (a) basic cell, (b) elementary-lift cell, (c) self-lift cell, and (d) double self-lift cell [35, 52]. ..... 56
Figure 2-13: Ideal continuous-conduction-mode voltage-gain laws of the principal non-isolated boosting routes: conventional boost (eq. 2.2), switched-inductor boost, boost with one voltage-multiplier stage, and quadratic (cascaded) boost. Markers indicate the duty cycle each route requires for a tenfold gain. Computed by the gain laws of Section 2.4 [34, 35, 39]. ..... 57
Figure 3-1: Generic Maximum Power Point Tracking control loop: the algorithm senses the array terminal voltage and current and issues a duty-cycle command *D* to the converter's PWM stage [17, 24, 64]. ..... 68

Figure 3-2: Flowchart of the perturb-and-observe (P&O) algorithm in its compact sign form, equation (3.2) [23, 24, 61] ..... 71
Figure 3-3: Circuit-level schematic of perturb-and-observe tracking on a boost stage, with its control system. (a) Fixed-step P&O in the direct duty-cycle structure: the measured array voltage $v_{pv}$ and current $i_{pv}$ (current sensor CS) give P(k) and ΔP(k), and equation (3.2) updates the duty cycle with a fixed perturbation ΔD, the previous increment ΔD(k) being held in memory ($z^{-1}$). (b) Variable-step and self-predictive P&O: the step is scaled with the power–voltage gradient, and a mode logic switches to a predictive stage after the first oscillation and holds D while |ΔP| stays below a noise-referenced threshold $\Delta P_{th}$, as described in Section 3.2.1 [23, 24, 61] (a) and [40, 41, 46, 64] (b) ..... 73
Figure 3-4: Flowchart of the Incremental Conductance (INC) algorithm, testing the conductance-equality condition of equation (3.3) [17, 51, 64, 68-70]. ..... 74
Figure 3-5: Circuit-level schematic of Incremental Conductance tracking on a boost stage in the direct duty-cycle structure: the finite differences ΔV and ΔI of the measured array voltage and current form the conductance test $g = \Delta I/\Delta V + I/V$ of equation (3.3), compared with the tolerance band $\pm\varepsilon$; since $v_{pv} = (1 - D)V_o$ for a boost stage, raising $v_{pv}$ means decreasing D, hence $D(k+1) = D(k) \mp \Delta D$. The ΔV = 0 branch of the flowchart is omitted for clarity [17, 51, 64, 68-70]. ..... 75
Figure 3-6: Circuit-level schematics of the constant-voltage and constant-current methods in the reference-based structure. (a) Constant voltage: a single voltage sensor and a proportional–integral loop hold $v_{pv}$ at a fixed reference $V_{ref}$ chosen near $V_{mpp}$ at rated conditions. (b) Constant current: a single current sensor (CS) and a proportional–integral loop hold $i_{pv}$ at a fixed fraction of $I_{sc}$. Neither method searches for the maximum power point [64-66, 71].. ..... 76
Figure 3-7: Circuit-level schematics of the fractional methods of equation (3.4) in the reference-based structure. (a) Fractional open-circuit voltage: every update period $T_u$ a timer briefly opens $S_{oc}$, so that the voltage sensor reads $V_{oc}$, which is held and scaled by $k_1$ to give $V_{ref}$. (b) Fractional short-circuit current: the timer opens $S_{oc}$ and closes $S_{sc}$, so that the current sensor reads $I_{sc}$, which is held and scaled by $k_2$ to give $I_{ref}$; opening $S_{oc}$ also keeps $C_{in}$ from discharging through $S_{sc}$. The array delivers no power while it is sampled, and a pilot cell can replace the switches [43, 64, 66, 69, 72, 73] ..... 78
Figure 3-8: The two canonical MPPT control structures of Table 3-2: (a) direct duty-cycle structure, in which the algorithm output drives the PWM stage directly; (b) reference-based structure, in which the algorithm generates a voltage reference $V_{ref}$ enforced by an inner proportional–integral (PI) loop [17, 25, description in Section 3.2.6]. ..... 82
Figure 3-9: : Classification of MPPT algorithm families surveyed in this chapter [24, 64, 66] ... 83

Figure 3-10: Circuit-level schematics of fuzzy-logic MPPT on a boost stage in the direct duty-cycle structure. The measured array voltage and current give the slope error E = ΔP/ΔV and its increment ΔE, which are fuzzified with typically five to seven membership functions per input (sketched from negative big, NB, to positive big, PB) and processed by a rule table. (a) Mamdani inference: the rules activate fuzzy output sets, which are defuzzified, for example by the centroid method, into the duty-cycle increment ΔD. (b) Takagi–Sugeno inference: the consequent of each rule is a direct function $z_i = f_i(E, \Delta E)$ of the inputs, and ΔD is the average of the consequents weighted by the rule firing strengths $w_i$, which is cheaper to compute online [64, 65, 74, 75]....84
Figure 3-11: : Circuit-level schematics of neural and neuro-fuzzy MPPT on a boost stage in the reference-based structure. (a) A feed-forward network with one or two hidden layers, trained offline, maps the measured irradiance G and module temperature T to the maximum-power voltage, which serves as the reference $V_{ref}$ of a conventional proportional–integral inner loop. (b) Neuro-fuzzy (ANFIS-type) arrangement: a trained network generates the reference, and a fuzzy controller acting on the error e and its increment Δe enforces it, its membership functions and rule weights being tuned by training rather than by hand [65, 86] (a) and [76] (b). .....86
Figure 3-12: Circuit-level schematic of particle swarm optimisation MPPT on a boost stage in the direct duty-cycle structure. Each of the N particles is a candidate duty cycle $d_i$, applied through the PWM stage; after the settling time of equation (2.9), the measured power $P_i = v_{pv}i_{pv}$ is its fitness. The personal and global bests are updated, and equations (3.5)–(3.6) generate the next candidates, kept within the fractional band of Section 3.2.4 as in the hardware design discussed in the text. Once the swarm has converged, D is held at $g_{best}$ until a power change exceeding a threshold restarts the search [73].....88
Figure 3-13: Update blocks of the other population-based methods and of golden-section search, each taking the place of the PSO update block in the loop of Figure 3-12: each receives the measured fitness $P_i$ of the current candidates and returns the next candidate duty cycles. (a) Grey wolf optimisation: the three best candidates (α, β, δ) guide the rest within a contracting radius, often followed by a P&O hand-over. (b) Genetic algorithm: selection, crossover and mutation produce each new generation; its most durable role is the offline tuning of a fuzzy controller. (c) Ant colony optimisation: new candidates are sampled near archive members with a probability proportional to their pheromone $\tau_j$. (d) Bat, cuckoo and firefly algorithms: family-specific stochastic steps. (e) Golden-section search: a deterministic bracket [a, b] around the peak is reduced by the golden ratio, reusing one evaluation per iteration [64] (a), [78] (b), [79] (c), [77, 80-82] (d) and [83] (e).....90

Figure 3-14: Generic two-stage (hybrid) MPPT structure and its supervisory logic: a global or coarse stage relocates the operating point near the correct peak, a local stage refines it, and two thresholds - the handover condition and the re-search trigger - coordinate the stages [64, 69, 72, description in Section 3.4.1]. ..... 93
Figure 3-15: Circuit-level schematic of a hybrid (global + local) tracker on a boost stage: a global or coarse stage (fractional estimate, model inversion or population search) and a local refinement stage (small-step P&O or INC) each propose a duty cycle, and the supervisor selects which of them commands the converter, applying the handover condition and the re-search trigger described in Section 3.4.1 [16, 64, 69, 72, 84]. ..... 94
Figure 3-16: Circuit-level schematic of a sensorless machine-learning tracker on a boost stage in the reference-based structure: a buffer of recent terminal voltage and current samples feeds a sequence-aware deep network (for example a long short-term memory or attention-based network), whose prediction of the maximum-power voltage is enforced by a proportional–integral inner loop. The network is trained offline and must be retrained as the array drifts away from its training conditions [65, 86, 87]. ..... 96
Figure 3-17: Circuit-level schematic of an actor–critic reinforcement-learning tracker on a boost stage in the direct duty-cycle structure: the actor maps the state (terminal voltage, current and their recent history) to a duty-cycle adjustment $a_k$, limited by safe-exploration bounds, while the critic estimates the value of the actor's choices from a reward built on the extracted power and supplies the learning signal. Every learning step is a physical excursion of the operating point [37, 65, 88]. ..... 98
Figure 3-18: Circuit-level control structures, on a boost stage, of (a) finite-control-set model predictive control, in which a prediction model fed by the measured $v_{pv}$ and $i_L$ and the cost function of equation (3.7) select the switch state directly, and (b) sliding-mode control, in which a discontinuous switching law drives the system onto a sliding surface defined on the tracking objective [91, 96, 97, descriptions in Sections 3.4.4–3.4.5]. ..... 103
Figure 3-19: Circuit-level schematics of the two variants described in Sections 3.4.4–3.4.5: (a) fixed-switching model predictive control, in which a predictive observer of the photovoltaic model supplies the optimal reference to a conventional proportional–integral regulator and modulator, so that the switching frequency stays constant; (b) super-twisting sliding-mode control, in which the discontinuous action is applied to the derivative of the sliding variable, so that the duty-cycle command passed to the modulator is continuous [91] (a) and [98] (b). ..... 104
Figure 3-20: Flowchart of the Pelican Optimisation Algorithm (POA) applied to MPPT [102] (Fig. 5) under a CC BY 4.0 licence. ..... 104

Figure 3-21: Stand-alone photovoltaic system of a partially shaded PV array with bypass diodes feeding a single-switch high-gain DC–DC converter whose duty cycle is set by the POA-based MPPT controller [102] (Fig. 6) under a CC BY 4.0 licence. ..... 108
Figure 3-22: Experimental hardware used to validate the POA-based MPPT in (a) prototype board of the DC–DC converter and PIC-microcontroller-based MPPT controller, with the schematic of the converter; (b) laboratory set-up with the 2S-2P array of four PV panels (partial shading produced by a thin plastic sheet), resistive load, host PC and digital storage oscilloscope (DSO). Adapted from [102] (Figs. 13 and 14) under a CC BY 4.0 licence. ..... 109
Figure 3-23: : Measured transient response for irradiance steps of 1000 → 800 → 600 W/m² with (a) POA, settling in 82.2 ms, and (b) PSO, settling in 99.2 ms (oscilloscope traces of array voltage, current and computed power; math scale 10 W/div) [102] (Fig. 15) under a CC BY 4.0 licence ..... 110

# List of Tables

Table 1-1: Indicative electrical quantities for a conventional crystalline-silicon cell, module and string at Standard Test Conditions. Values are order-of-magnitude illustrations rather than product specifications (compiled from [7]). ..... 22
Table 1-2: Comparison of the single-diode and double-diode equivalent-circuit models. References are given in the last column. ..... 25
Table 1-3: Single-diode model parameters used to compute Figure 1-5, and the resulting characteristic quantities at STC [13], [15]. ..... 26
Table 1-4: Conversion granularity in grid-connected photovoltaic systems (compiled from [28, 29]). ..... 35
Table 2-1: Photovoltaic assessment of the six basic non-isolated converters. ..... 47
Table 2-2: General comparison of the non-isolated and isolated converter families for photovoltaic service. ..... 53
Table 2-3: The principal non-isolated voltage-boosting techniques and what each costs. ..... 59
Table 2-4: Converter selection criteria relevant to MPPT implementation. ..... 62
Table 2-5: Converter-level summary of the topologies surveyed in this chapter, grouped by family, with the quantitative indicators reported in the sources. ..... 65
Table 3-1: Comparative summary of conventional MPPT methods. ..... 80
Table 3-2: The two canonical MPPT control structures compared [25] ..... 82
Table 3-3: Comparative summary of intelligent (fuzzy-logic, ANN, neuro-fuzzy) MPPT methods ..... 87
Table 3-4: Metaheuristic and population-based MPPT methods. ..... 91
Table 3-5: Sliding-mode control and model predictive control compared for photovoltaic MPPT service. ..... 105
Table 3-6: Critical comparison of the most recent MPPT techniques surveyed in Section 3.4 .. 106
Table 3-7: Performance of the POA-based MPPT and of four benchmark algorithms on the high-gain converter (MATLAB/Simulink simulation; values transcribed from Table 4 of [102]) ..... 109
Table 3-8: Method-level summary of the MPPT methods surveyed in this chapter, grouped by family, with the quantitative indicators reported in the sources; all verdicts are conditional on the shading pattern, irradiance profile and converter of the underlying studies. ..... 114

Table 4-1: Comparative overview of the classical and intelligent MPPT tiers against the performance criteria of Chapter 3. For detailed per-method evidence and references, see Table 3-1 (Conventional, Constant V/I) and Table 3-3 (Intelligent). ..... 117
Table 4-2: Comparative overview of the metaheuristic, hybrid and most recent MPPT tiers against the performance criteria of Chapter 3. For detailed per-method evidence and references, see Table 3-4 (Metaheuristic), Table 3-6 (Hybrid, ML/DL/RL, MPC/SMC), and Table 3-5 (MPC vs. SMC in detail) ..... 117
Table 4-3: Qualitative link between converter family and MPPT implementation (see Table 2-5 [47, 63]). ..... 119
Table 4-4: Joint converter–algorithm design procedure assembled from the criteria of Chapters 2 and 3. ..... 120
Table 4-5: Quantitative results of the two studies in which converter and conventional MPPT algorithm are varied jointly [100, 101]. ..... 121
Table 4-6: Emerging trends assessed against the challenges of Section 4.3.5. ..... 127

# Nomenclature and Acronyms

### Acronyms

| Acronym | Meaning |
|---|---|
| ACO | Ant Colony Optimisation |
| ADC | Analogue-to-Digital Converter |
| AI | Artificial Intelligence |
| AM | Air Mass (as in the AM 1.5 reference spectrum) |
| ANFIS | Adaptive Neuro-Fuzzy Inference System |
| ANN | Artificial Neural Network |
| CC | Constant Current (MPPT method) |
| CCM | Continuous Conduction Mode |
| CIGS | Copper Indium Gallium Selenide (thin-film technology) |
| CS | Cuckoo Search; current sensor (in circuit schematics) |
| CV | Constant Voltage (MPPT method) |
| DC | Direct Current |
| AC | Alternating Current |
| DCM | Discontinuous Conduction Mode |
| DL | Deep Learning |
| DPP | Differential Power Processing |
| DSO | Digital Storage Oscilloscope |
| DSP | Digital Signal Processor |
| EMI | Electromagnetic Interference |
| FF | Fill Factor |
| FLC | Fuzzy Logic Control |
| FOCV | Fractional Open-Circuit Voltage |
| FPGA | Field-Programmable Gate Array |
| FSCC | Fractional Short-Circuit Current |
| GA | Genetic Algorithm |
| GMPP | Global Maximum Power Point |
| GWO | Grey Wolf Optimisation |
| IC | Incremental Conductance (notation of [100] and [101]) |
| IEA | International Energy Agency |
| INC | Incremental Conductance |
| IRENA | International Renewable Energy Agency |
| LLC | Inductor–Inductor–Capacitor (resonant tank) |
| LMPP | Local Maximum Power Point |
| LSTM | Long Short-Term Memory (network) |
| MPC | Model Predictive Control |
| ML | Machine Learning |
| MPP | Maximum Power Point |
| MPPT | Maximum Power Point Tracking |
| NB, PB | Negative Big, Positive Big (fuzzy linguistic labels) |
| NREL | National Renewable Energy Laboratory |
| P&O | Perturb and Observe |

| Acronym | Meaning |
|---|---|
| PI | Proportional–Integral (controller) |
| PID | Potential-Induced Degradation |
| POA | Pelican Optimisation Algorithm |
| PSC | Partial Shading Condition |
| PSO | Particle Swarm Optimisation |
| PV | Photovoltaic |
| PWM | Pulse-Width Modulation |
| RCD | Resistor–Capacitor–Diode (clamp) |
| RL | Reinforcement Learning |
| SEPIC | Single-Ended Primary-Inductance Converter |
| SMC | Sliding-Mode Control |
| STC | Standard Test Conditions |
| VL | Voltage Lift |
| VMC | Voltage Multiplier Cell |
| WBG | Wide-Bandgap (semiconductor) |
| ZCS | Zero-Current Switching |
| ZVS | Zero-Voltage Switching |

## Principal symbols

| Symbol | Meaning |
|---|---|
| $a$ | Diode ideality factor |
| $c_1$, $c_2$ | Acceleration coefficients of particle swarm optimisation |
| $D$ | Converter duty cycle |
| $E_g$ | Semiconductor band-gap energy |
| $f_s$ | Switching frequency |
| $f_r$ | Resonant frequency of a soft-switching network |
| $FF$ | Fill factor |
| $G$ | Solar irradiance |
| $G_n$ | Rated (STC) irradiance |
| $I$ | Terminal current of a PV cell/module |
| $I_0$ | Diode reverse-saturation current |
| $I_{mpp}$ | Current at the maximum power point |
| $I_{pv}$, $I_{ph}$ | Photogenerated current |
| $I_{sc}$ | Short-circuit current |
| $J$ | Cost function of model predictive control |
| $k$ | Boltzmann constant |
| $k_1$, $k_2$ | Proportionality constants of the fractional open-circuit-voltage and short-circuit-current methods |
| $K_I$ | Short-circuit current temperature coefficient |
| $L$ | Inductance |
| $L_r$ | Resonant inductance (with $C_r$, resonant capacitance) |
| $M(D)$ | Converter voltage gain as a function of duty cycle |
| $n$ | Transformer turns ratio, $N_s/N_p$ |
| $N_p$ | Number of primary winding turns of a transformer |
| $N_s$ | Number of series-connected cells (Chapter 1); number of secondary winding turns (Chapter 2) |

| Symbol | Meaning |
|---|---|
| $P$ | Instantaneous power |
| $P_{av}$ | Instantaneously available (maximum) power |
| $P_{mpp}$ | Power at the maximum power point |
| $q$ | Elementary charge |
| $Q$ | Quality factor of a resonant network |
| $R_L$ | Load resistance |
| $R_p$ | Shunt (parallel) resistance |
| $R_{pv}$, $R_{in}$ | Resistance reflected to the converter input |
| $R_s$ | Series resistance |
| $T_c$ | Cell temperature |
| $T_p$ | MPPT sampling (perturbation) interval |
| $V$ | Terminal voltage of a PV cell/module |
| $V_{in}$ | Converter input voltage |
| $V_{mpp}$ | Voltage at the maximum power point |
| $V_o$ | Converter output voltage |
| $V_{oc}$ | Open-circuit voltage |
| $V_T$ | Thermal voltage, $kT/q$ |
| $w$ | Inertia weight of particle swarm optimisation |
| $Z_0$ | Characteristic impedance of a resonant network |
| $\gamma$ | Module power-temperature coefficient |
| $\Delta D$ | Duty-cycle perturbation step |
| $\varepsilon$ | Tolerance band of the Incremental Conductance test |
| $\eta$ | Conversion efficiency |
| $\eta_{MPPT}$ | Tracking efficiency |
| $\sigma$ | Sliding surface of sliding-mode control |

# 1 CHAPTER 1 - INTRODUCTION AND PHOTOVOLTAIC SYSTEMS

## 1.1 Motivation and Background

Photovoltaic (PV) generation has moved, in little more than a decade, from a specialised branch of renewable-energy engineering to the dominant source of new electricity-generating capacity worldwide. According to the International Renewable Energy Agency (IRENA), global renewable power capacity reached 5,149 GW at the end of 2025, of which solar accounted for 2,392 GW - a larger installed base than any other renewable technology and almost twice the 1,291 GW of installed wind capacity [1]. Of the record 692 GW of renewable capacity commissioned during 2025, 511 GW was solar and 510 GW of that figure was solar PV alone; renewable sources therefore represented 85.6% of all new generating capacity added worldwide that year [1]. Capacity statistics differ appreciably between sources for methodological rather than physical reasons - IRENA compiles net generating capacity as reported by national authorities, whereas the International Energy Agency (IEA) publishes independent market estimates and reports approximately 605 GW of solar PV additions for the same year [1, 2] - so any capacity figure cited in this thesis is accompanied by its source. The medium-term outlook reinforces the trend: the IEA expects approximately 4,600 GW of renewable capacity to be added globally between 2025 and 2030, with solar PV accounting for nearly 80% of that growth and distributed PV representing about 42% of the PV expansion [103].

The distinction between distributed and utility-scale deployment is significant for the subject of this thesis, because a residential rooftop array, a commercial installation and a utility-scale plant rarely share the same power-electronic architecture: they differ in array voltage, in cost tolerance, in whether storage is present, and in whether the interconnection is made to a DC bus, an AC grid, or an isolated load.Figure 1-1 places the three side by side. Each context demands a different balance between converter complexity and control sophistication, yet the same underlying engineering question recurs in all of them: given a PV array whose electrical characteristic varies continuously with the weather, how should the power-electronic interface placed between that array and its load be designed and controlled so that the available energy is not wasted?




Figure 1-1: The three deployment contexts contrasted in this section, which rarely share the same power-electronic architecture, and two of the components that distinguish them: (a) a residential rooftop array on a private house in Los Angeles [104]; (b) a commercial rooftop installation on a storage facility in Gilroy, California [105]; (c) part of the 15 MW utility-scale plant at Nellis Air Force Base, Nevada, comprising approximately 70,000 modules [106]; (d) a 1 MW / 4 MWh containerized battery energy storage system in Pullman, Washington [107]; (e) a commercial all-in-one off-grid hybrid inverter (MPP Solar LV2424-MSD), which combines a built-in MPPT solar charger, a battery charger and an inverter in one enclosure [108, 109].

This question is the organising thread of the present work. The thesis is a bibliographic review of the literature that answers it in two complementary ways - through the design of the DC–DC converter that interfaces the array to the rest of the system, and through the Maximum Power Point Tracking (MPPT) algorithm that commands that converter - with particular emphasis on the most recent MPPT techniques reported in the literature and on the relationship between the converter and the tracking algorithm that acts through it.

## 1.2 The Photovoltaic Effect and the Solar Cell

### 1.2.1 Physical mechanism

The photovoltaic effect is the direct conversion of electromagnetic radiation into electricity within a semiconductor junction, first observed by Becquerel in 1839, treated quantitatively for the p–n junction in the early 1950s [3], and realised as a practical silicon device by Chapin, Fuller and Pearson in 1954 at an efficiency of approximately 6% [4, 5]. In a semiconductor, electron states are grouped into a valence band and a conduction band separated by an energy gap $E_g$. A photon of wavelength $\lambda$ carries energy

$$E_{ph} = h \cdot \frac{c}{\lambda} \quad (1.1)$$

where $h$ is Planck's constant and $c$ the speed of light; absorption promotes an electron across the gap only if $E_{ph} \geq E_g$, defining a cut-off wavelength $\lambda_g = h \cdot c/E_g$ beyond which the material is effectively transparent [6]. For crystalline silicon, with $E_g \approx 1.12eV$, the cut-off falls at approximately 1100 nm.

Because each usable photon yields at most one electron–hole pair, the generated current tracks the incident photon flux almost linearly, while photons of energy above the gap surrender their excess energy as heat (thermalisation). A single band gap therefore cannot suit the whole solar spectrum: lowering it captures more photons at the cost of greater thermalisation loss, and raising it does the reverse. Shockley and Queisser formalised this trade-off, placing the theoretical limit for a single-junction cell under one-sun illumination at approximately 33%, at an optimal gap near 1.3 eV [6]; silicon, at 1.12 eV, sits close enough to that optimum that the penalty is small, which is one of the properties behind its continued dominance of the cell market [7, 8].

Generation alone does not produce usable current: an electron–hole pair left to itself recombines and returns its energy to the lattice as heat. The p–n junction supplies the built-in electric field - present in the dark, not created by illumination - that separates a photogenerated pair before it can recombine, driving the electron and hole to opposite terminals and producing a voltage capable of driving current through an external load for as long as illumination persists [9]. The same junction is unavoidably also a diode, so that the terminal current of an illuminated cell is, to a first approximation, the difference between a photogenerated current and an internal diode current: $I = I_{ph} - I_D(V)$. This balance between a constant term and an exponential term produces the

characteristic knee of the current–voltage curve and, consequently, the single well-defined maximum-power point that exists under uniform illumination.

### 1.2.2 From cell to module to array

Junction physics fixes what a single cell can deliver irrespective of application requirements: a crystalline-silicon cell develops an open-circuit voltage of roughly 0.6–0.7 V, operates near 0.55 V at its maximum power point, and supplies a current on the order of 10 A for contemporary cell formats at Standard Test Conditions (STC - 1000 W/m² irradiance, 25 °C cell temperature, AM 1.5 reference spectrum) [7, 10]. Reaching practical voltage and power levels is therefore a matter of aggregation: cells are connected in series to build voltage within a module, modules are connected in series to form strings, and strings in parallel to form arrays, in whatever combination the application requires [7]. Figure 1-2 shows the same hierarchy as physically realised, from the series interconnection of cells inside a module to a complete ground-mounted array.Table 1-1 gives indicative electrical quantities at each level for a conventional crystalline-silicon product.

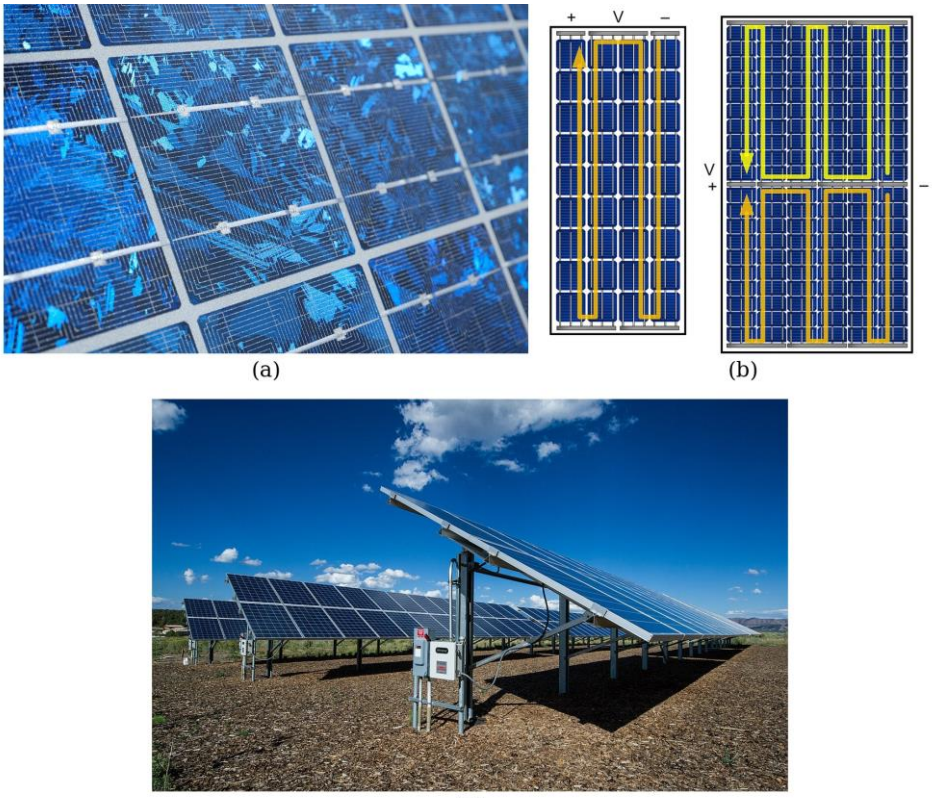



Figure 1-2: Physical realization of the cell–module–string–array hierarchy: (a) close-up of the series-interconnected cells of a polycrystalline module (photograph by G. Vellut, CC BY 2.0) [110]; (b) schematic of the internal interconnection of standard modules: left, a single string of 36 cells in series; right, two sub-matrices in parallel, each of 60 half-cut cells in series (C. Domínguez, CC BY-SA 4.0) [111]; (c) a 67 kW array at the Mesa Verde Visitor and Research Center, Colorado, formed by 286 modules of 235 W wired as 22 parallel strings of 13 series-connected modules (photograph by D. Schroeder/NREL, Public Domain Mark 1.0) [112].

Because an illuminated cell behaves as a current source, a series-connected chain can carry no more current than its weakest member permits; differences in output between cells or modules - arising from shading, soiling, or manufacturing spread - translate into a disproportionately large reduction in the power of the whole assembly [11]. This sensitivity, a direct inheritance of the current-source physics of the photovoltaic effect, is the origin of the partial-shading problem discussed in Section 1.5.3 and is addressed architecturally, at the conversion-topology level, in Chapter 2.

Table 1-1: Indicative electrical quantities for a conventional crystalline-silicon cell, module and string at Standard Test Conditions. Values are order-of-magnitude illustrations rather than product specifications (compiled from [7]).

| Quantity at STC | Single cell | Module (60 cells in series) | String (20 modules in series) |
|---|---|---|---|
| Open-circuit voltage | ≈ 0.65 V | ≈ 39 V | ≈ 780 V |
| Voltage at maximum power | ≈ 0.55 V | ≈ 33 V | ≈ 660 V |
| Current at maximum power | ≈ 11 A | ≈ 11 A | ≈ 11 A |
| Power at maximum power point | ≈ 6 W | ≈ 360 W | ≈ 7.2 kW |

Silicon accounts for roughly 90% of the photovoltaic cell market, a dominance attributed to a favourable combination of properties: a band gap reasonably well matched to the terrestrial spectrum, chemical stability, abundance of the raw material, and a manufacturing base shared with the microelectronics industry [7]. Device technologies are conventionally grouped into three generations - wafer-based crystalline silicon; thin-film technologies (amorphous silicon, CdTe, CIGS), which use less absorber material at the cost of lower efficiency; and emerging approaches (multi-junction III–V, perovskite, organic and dye-sensitised cells), largely pre-commercial for terrestrial power generation [7, 8, 12]. Because the review that follows assumes conventional silicon-based arrays throughout, tracking strategies specific to emerging cell technologies are outside its scope and are noted only where the surveyed literature raises them.

## 1.3 Equivalent-Circuit Model of the PV Generator

Translating the physical description above into a circuit that can be simulated and analysed is a prerequisite for everything that follows: in the vast majority of converter and MPPT studies, the array against which an algorithm is evaluated is not a physical array but one of the equivalent-circuit models developed in this section.

### 1.3.1 The single-diode model

The single-diode (or five-parameter) model represents the light-driven generation of carriers as a current source $I_{pv}$ proportional to irradiance, in parallel with a diode representing the junction, and two parasitic elements: a series resistance $R_s$ (semiconductor bulk, metal contacts, front grid) and a shunt resistance $R_p$ (leakage paths). Figure 1-3 shows the resulting equivalent circuit. For a module of $N_s$ series-connected cells, the terminal characteristic is [13]

$$I = I_p v - I_0 \left[ exp\left( \frac{(V + IR_s)}{(aN_s V_T)} \right) - 1 \right] - \frac{(V + IR_s)}{R_p} \quad (1.2)$$

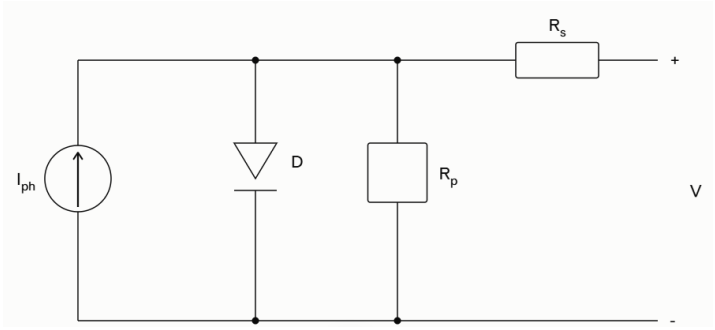



Figure 1-3: Single-diode equivalent-circuit model of a photovoltaic cell/module: a light-generated current source in parallel with a diode, a shunt resistance $R_p$, and a series resistance $R_s$ [13], [15].

where $I_0$ is the diode reverse-saturation current, $a$ the diode ideality factor (customarily $a = 1$ for crystalline silicon), and $V_T = k \cdot T/q$ the thermal voltage ($k$ the Boltzmann constant, $T$ the junction temperature in kelvin, $q$ the elementary charge). Because equation (1.2) is implicit in $I$, it is normally solved by a fixed-point or Newton iteration; in a well-made crystalline-silicon device $R_p$ is large and $R_s$ small [9, 13]. The five quantities $I_{pv}$, $I_0$, $a$, $R_s$ and $R_p$ fully determine the characteristic and are ordinarily extracted from the short-circuit current, open-circuit voltage and maximum-power coordinates given on the manufacturer's datasheet, typically by iterating $R_s$ and $R_p$ jointly until the modelled maximum power matches the datasheet value [13]. The approach owes much of its standing to De Soto et al., who formalised the translation of the extracted parameters to arbitrary operating conditions and validated the result against measured data for several cell technologies [14].

The parameters are not constants of the device: the photocurrent scales almost linearly with irradiance and drifts weakly with temperature,

$$I_{pv} = (I_{pv,n} + K_I \cdot \Delta T) \frac{G}{G_n} \quad (1.3)$$

while the saturation current depends strongly on temperature through the semiconductor band gap $E_g$ [13]. Here $G$ is the incident irradiance, $G_n$ the rated (STC) irradiance, $K_I$ the manufacturer's short-circuit current temperature coefficient, and $\Delta T$ the departure of the cell temperature from its rated value. These translation equations are what allow a model identified once from datasheet data at STC to be used at any other operating condition - a step made necessary by the fact, developed in Section 1.5, that a field-installed array spends almost all of its working life away from STC.

### 1.3.2 The double-diode model and model choice as an experimental variable

The single-diode model's principal weakness lies in the depletion region: at low voltage and low irradiance, recombination inside the depletion region contributes a current component that one ideal diode cannot reproduce. The double-diode model adds a second diode specifically to represent this recombination loss, at the cost of two additional parameters (seven in total, reducible to five by simplified formulations) [15]. Figure 1-4 gives the corresponding circuit. Cavalcanti et al. fitted both models to measured module characteristics and reported curve-fitting errors for the double-diode model several times lower than for the single-diode model, with the largest margin appearing away from the rated condition - precisely the low-irradiance regime in which partial shading and dawn/dusk tracking are decided [16]. Table 1-2 summarises the comparison. Because the great majority of MPPT studies evaluate algorithms on a simulated array built from the single-diode model, while a minority use the double-diode model, and the two disagree most exactly where tracking is hardest, the choice of PV model is itself a component of the test conditions under which a reported tracking result was obtained - a point to which the comparative discussion of Chapter 4 returns.

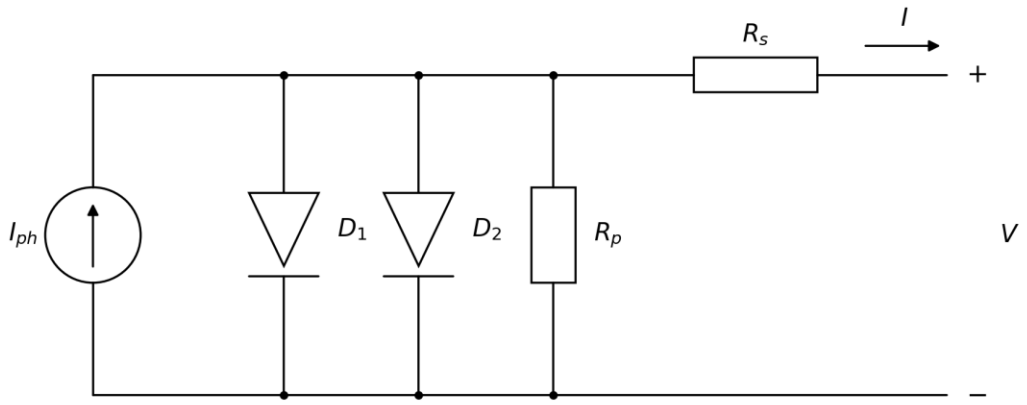



Figure 1-4: Double-diode equivalent-circuit model of a photovoltaic cell. The second diode $D_2$, in parallel with $D_1$, represents recombination in the depletion region, which a single diode cannot reproduce at low voltage and low irradiance. $I_{ph}$ is the light-generated current, $R_s$ the series resistance and $R_p$ the shunt resistance [15], [16].

Table 1-2: Comparison of the single-diode and double-diode equivalent-circuit models.

| Attribute | Single-diode model | Double-diode model | Reference(s) |
|---|---|---|---|
| Circuit elements | Current source, one diode, $R_s$, $R_p$ | Current source, two diodes, $R_s$, $R_p$ | [13, 15] |
| Parameters to identify | Five | Seven (reducible to five) | [13, 15] |
| Accuracy near rated conditions | Good | Good | [16] |
| Accuracy at low irradiance / near $V_{oc}$ | Degrades | Markedly better | [16] |
| Typical use | Real-time control, large-array simulation | Offline simulation, model-based tracking | [13, 15] |

## 1.4 Electrical Characteristics of the PV Generator

Sweeping the terminal voltage of equation (1.2) from short circuit to open circuit traces the current–voltage (I–V) characteristic; multiplying the two coordinates pointwise gives the power–voltage (P–V) characteristic. Figure 1-5 shows both, computed from equation (1.2) using the parameters of Table 1-3, representative of a 60-cell crystalline-silicon module at STC.

Table 1-3: Single-diode model parameters used to compute Figure 1-5, and the resulting characteristic quantities at STC [13], [15].

| Quantity | Symbol | Value |
|---|---|---|
| Cells in series | $N_s$ | 60 |
| Diode ideality factor | $a$ | 1.0 |
| Series resistance | $R_s$ | 0.22 Ω |
| Shunt resistance | $R_p$ | 500 Ω |
| Short-circuit current | $I_{sc}$ | 11.60 A |
| Open-circuit voltage | $V_{oc}$ | 39.0 V |
| Voltage at maximum power | $V_{mpp}$ | 32.0 V |
| Current at maximum power | $I_{mpp}$ | 10.96 A |
| Power at maximum power point | $P_{mpp}$ | 350 W |
| Fill factor | $FF$ | 0.775 |

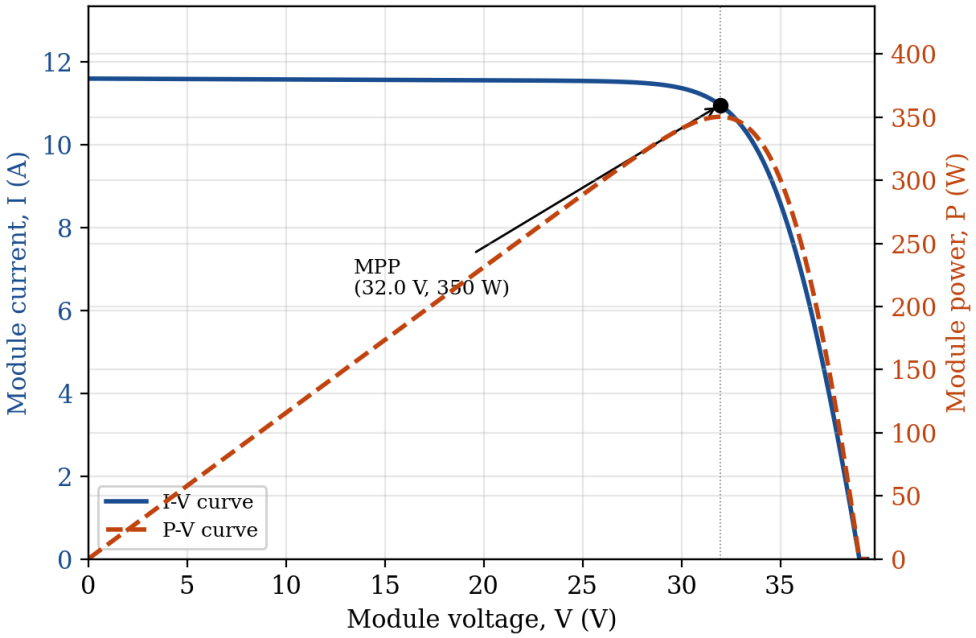



Figure 1-5: Current–voltage (I–V) and power–voltage (P–V) characteristics of the photovoltaic module of Table 1-3 at Standard Test Conditions, computed from the single-diode model of equation (1.2) [13], [15].

The I–V curve is anchored by two measurable extremes. At short circuit the diode and shunt terms are negligible, so the short-circuit current $I_{sc}$ essentially equals the photocurrent, inheriting its linear dependence on irradiance. At open circuit the photocurrent flows entirely through the diode, so $V_{oc}$ depends logarithmically on the ratio of photocurrent to saturation current [9, 13]. Between the anchors, the curve shows a nearly horizontal current-source plateau, a knee, and a steep voltage-source descent toward $V_{oc}$; the maximum power point sits at the knee, where the magnitude of the differential resistance $dV/dI$ equals the static resistance $V/I$ [17].

The most consequential property of the curve is what it does not contain: any preferred operating point. Because the array simply operates wherever the characteristic of the connected load intersects its own, a directly connected resistive load generally intersects the curve away from the knee. For the module of Table 1-3, a directly connected 6 Ω load lands the operating point at approximately 36.5 V and 6.1 A - about 222 W against an available 350 W, a loss of roughly 37% with nothing wrong with the module, the load, or the weather [18]. Removing this accident - adjusting the effective load seen by the array so that it always intersects the characteristic at the knee, whatever the prevailing irradiance and temperature - is precisely the function of the power-electronic interface studied in Chapter 2 and of the tracking algorithm studied in Chapter 3.

A single scalar summarises how closely the characteristic approaches the rectangle defined by its anchors, the fill factor

$$FF = \frac{P_{mpp}}{(V_{oc} \cdot I_{sc})} = \frac{(V_{mpp} \cdot I_{mpp})}{(V_{oc} \cdot I_{sc})} \quad (1.4)$$

Good crystalline-silicon modules exceed $FF = 0.75$; the slope near open circuit is governed by $R_s$, and the slope near short circuit by $R_p$ [19]. The efficiency of the device itself is a related but distinct quantity, the ratio of the maximum electrical power to the incident solar power, $\eta = P_{mpp}/(G \cdot A)$, which must be kept conceptually separate from the *tracking* efficiency introduced in Chapter 3 - the fraction of the theoretically available power that a given converter–controller combination actually extracts.

## 1.5 Environmental Dependence and the Need for Tracking

### 1.5.1 Irradiance and temperature

The operating conditions affect the module output in two distinct ways. Irradiance acts principally on the current: the photogenerated current scales in near-proportion to irradiance $G$ through equation (1.3), so that halving the irradiance approximately halves the available power, while $V_{oc}$ depending on $G$ only logarithmically - changes comparatively little. Figure 1-6 shows the resulting family of P–V curves for the module of Table 1-3: the maximum power falls in close proportion to irradiance while the voltage at which it occurs drifts by only a few per cent across a five-fold change in irradiance, a regularity exploited directly by the voltage-anchored tracking methods of Chapter 3.

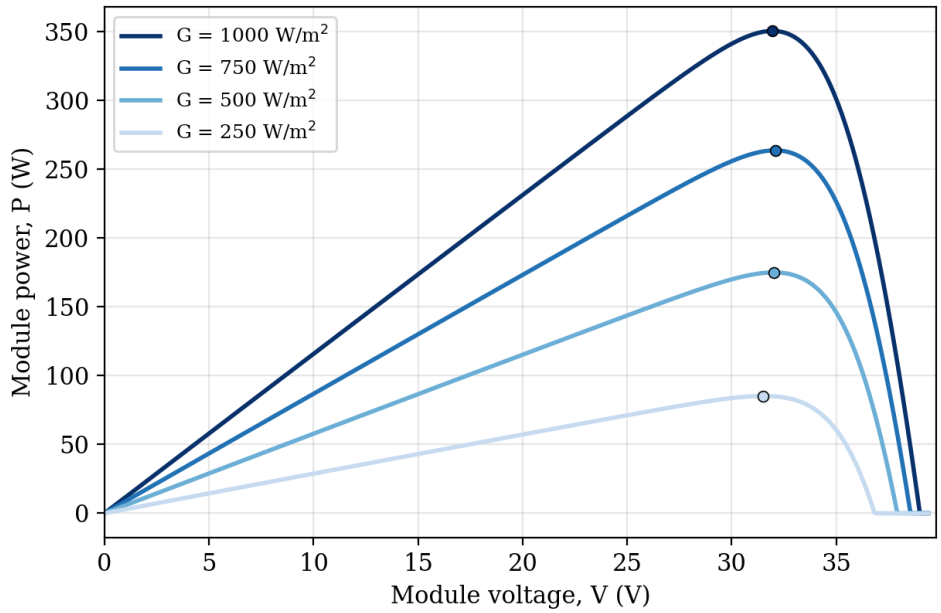



Figure 1-6: Effect of irradiance on the power–voltage characteristic of the module of Table 1-3 at a fixed cell temperature of 25 °C; markers indicate the maximum power point of each curve [13], [15].

Temperature acts principally on the voltage, and in the opposite direction: as the cell heats, the saturation current $I_0$ grows steeply while the band gap narrows, so $V_{oc}$ falls approximately linearly with temperature (Figure 1-7). The net effect on power is conventionally expressed through the module power-temperature coefficient $\gamma$,

$$P_{mpp}(T_c) = P_{mpp,STC} \cdot [1 + \gamma \cdot (T_c - 25\,°\mathrm{C})] \quad (1.5)$$

with $\gamma$ typically between −0.3%/K and −0.5%/K for crystalline-silicon modules [7, 8]. Since an illuminated module in still air commonly runs several tens of degrees above ambient temperature, this coefficient represents a substantial and unavoidable departure from nameplate output on precisely the days when irradiance is highest.

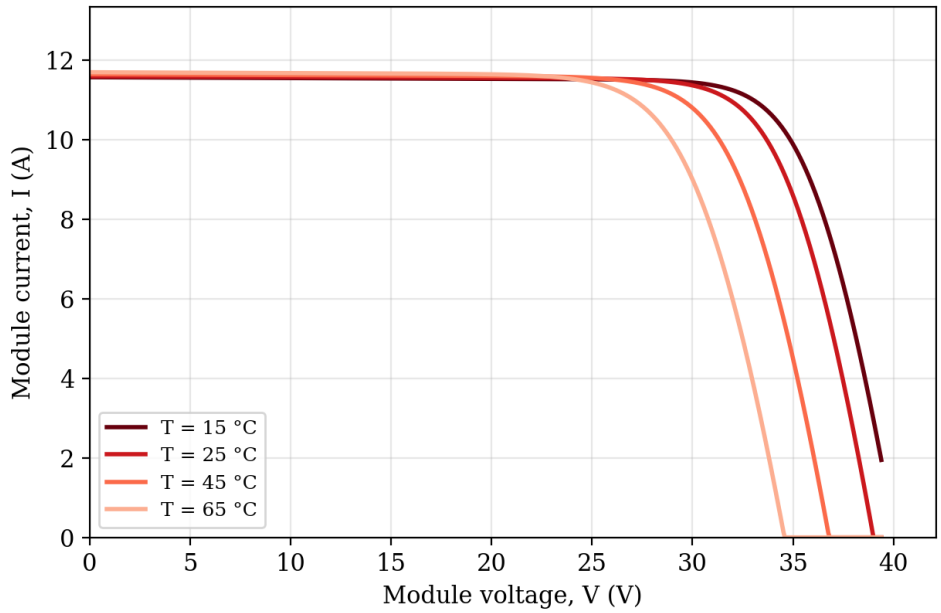



Figure 1-7: Effect of cell temperature on the current–voltage characteristic of the module of Table 1-3 at a fixed irradiance of 1000 W/m² [13], [15], [11]

Two further observations organise the disturbance environment that any tracking controller must confront. First, the variability of the resource operates on several timescales at once: a deterministic layer (the diurnal and seasonal cycles) can be predicted years in advance, while a stochastic layer (cloud passage, aerosol loading) cannot, and it is this fast layer - capable of reducing irradiance on a module by a large fraction within seconds - that dominates the design of a tracking algorithm's dynamic response. Second, the reference conditions at which devices are rated (STC) are a laboratory construction that field operation systematically fails to reproduce: over most operating hours the irradiance is well below 1 kW/m² and the cell runs above 25 °C, so the array spends almost all its working life away from the point at which it was rated. Maximum power point tracking exists precisely to extract the power actually available under whatever conditions prevail, rather than under the nameplate ones.

### 1.5.2 The maximum power point as a moving target

Because the operating point that maximises power - defined by the stationarity condition

$$\frac{\mathrm{d}P}{\mathrm{d}V} = I + V \cdot \left(\frac{\mathrm{d}I}{\mathrm{d}V}\right) = 0 \qquad (1.6)$$

- depends on irradiance and temperature that a simple controller does not measure directly, the maximum power point (MPP) is not a fixed setpoint but a trajectory. Under uniform illumination this trajectory is well-behaved: it retains a single peak, moves almost vertically in the

power–voltage plane as irradiance changes on the timescale of seconds, and drifts slowly and almost horizontally as temperature changes on the timescale of minutes to hours. A fast, largely vertical disturbance and a slow, largely horizontal one place different demands on a tracking algorithm, and the benchmark irradiance-step and temperature-ramp profiles used throughout the MPPT literature are stylised reproductions of exactly these two channels.

### 1.5.3 Partial shading and the multi-peak characteristic

A third environmental condition is qualitatively different because it changes the *shape* of the characteristic rather than merely its scale. When part of an array is unequally illuminated - by patchy cloud, the shadow of a nearby structure, vegetation, or soiling - the mismatched cells are forced to carry a current their own illumination cannot support. Left unprotected, this would drive the affected cells into reverse bias, creating a hot-spot risk; the standard protection is a bypass diode connected in anti-parallel across each module or sub-string (commercial 60-cell modules typically carry three, one per group of twenty cells), which conducts around the shaded section once its voltage collapses, sacrificing that section's contribution but protecting it from damage [20, 21]. Figure 1-8 shows the temperature field that results when a single cell is half shaded. The string voltage becomes a piecewise sum of individual module voltages, clamped at the bypass-diode drop wherever a module cannot sustain the string current, and it is this piecewise structure - not any new physics - that produces a power–voltage characteristic with **several local maxima and only one global maximum** (GMPP).

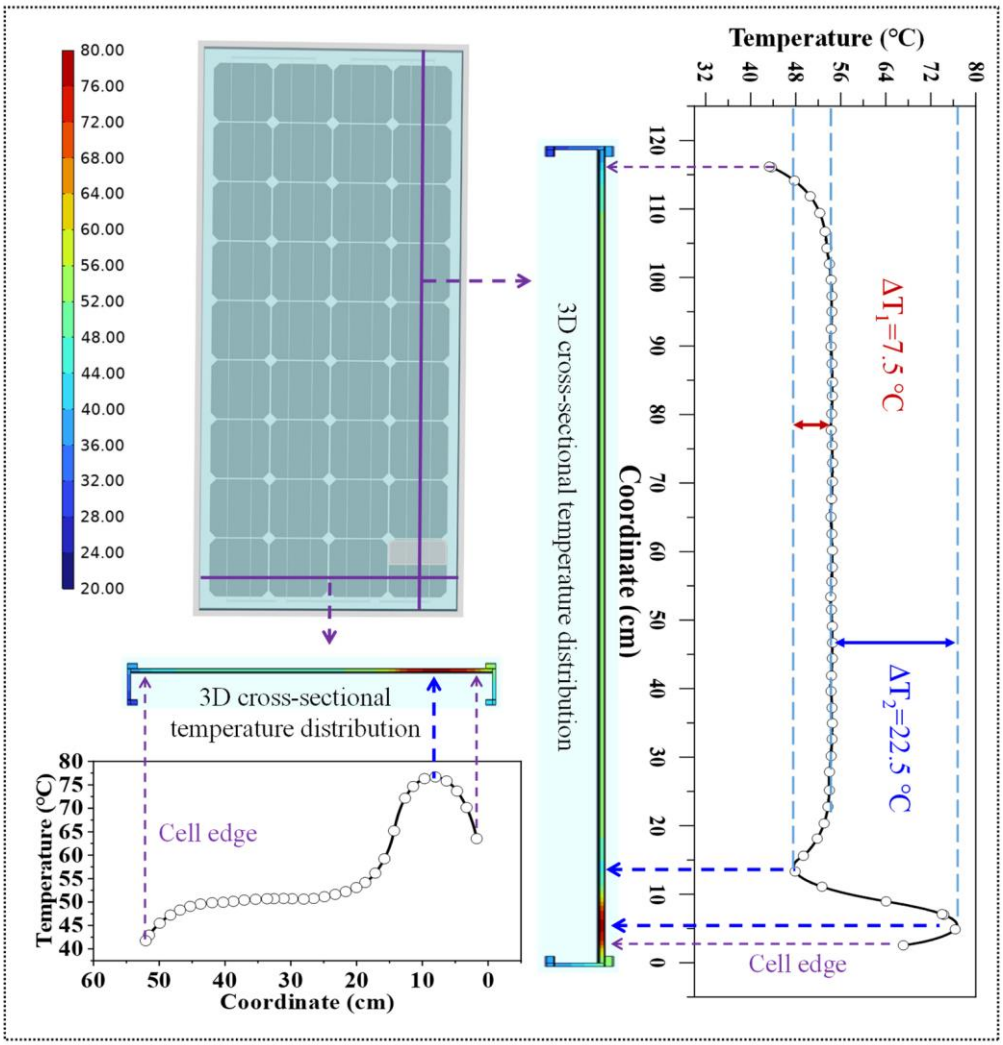
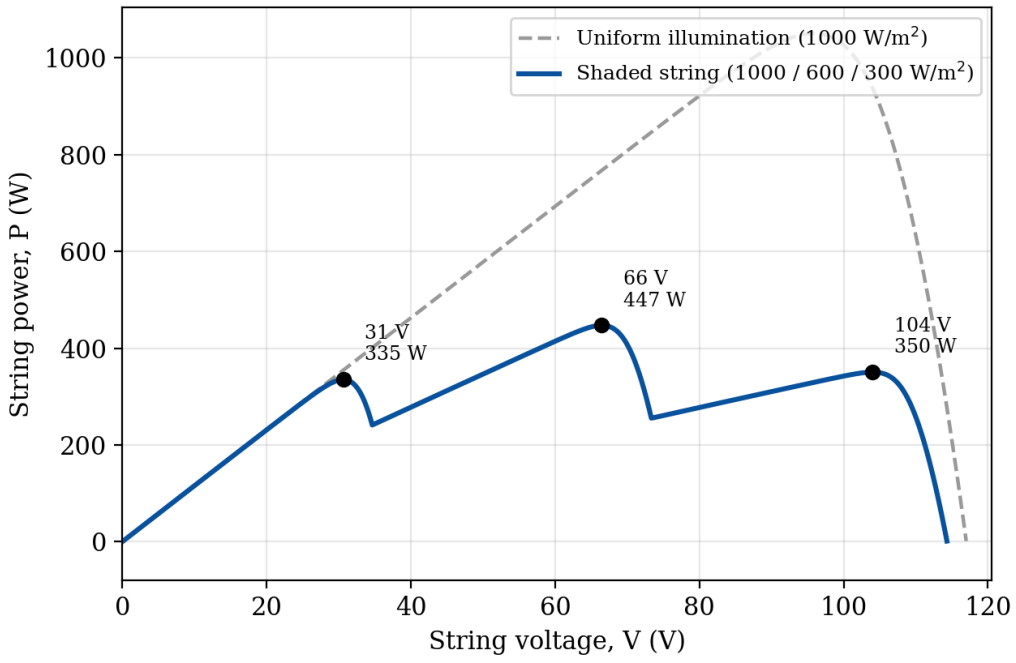
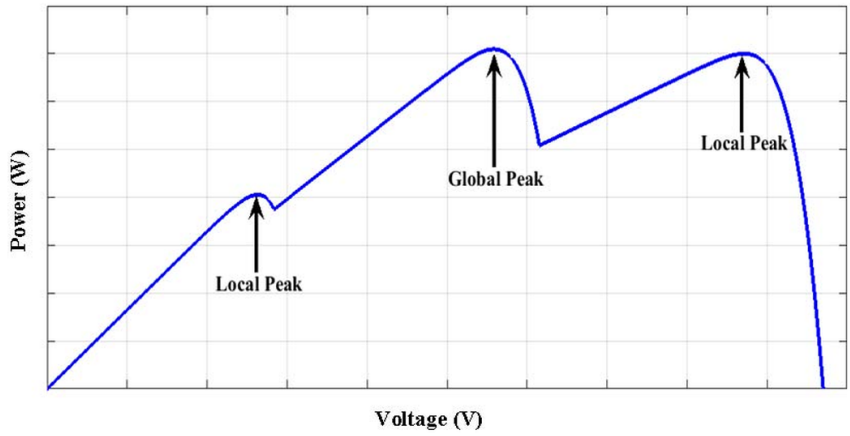



Figure 1-8: Temperature distribution in a locally shaded crystalline-silicon module at an irradiance of 750 W/m² with half of one cell shaded (shading ratio R = 1/2), obtained by thermal simulation and validated against infrared measurements. The module map (top left) marks two line scans, whose temperature profiles are plotted along the module length (right) and across the row containing the shaded cell (bottom left), each with its three-dimensional cross-section. The unshaded part of the shaded cell forms a hot spot of 77.66 °C, about 22.5 °C ($\Delta T_2$) above the surrounding cells, while the shaded part forms a cold spot about 7.5 °C ($\Delta T_1$) below them. Reproduced from [113], Fig. 5.

Figure 1-9 illustrates the effect for a string of three series-connected modules of the type in Table 1-3, each protected by its own bypass diode, under irradiances of 1000, 600 and 300 W/m². Three local maxima appear, at approximately 31 V/335 W, 66 V/447 W and 104 V/350 W; the global maximum is the *central* peak, not the first one a controller sweeping upward from low voltage would encounter, and it delivers only 447 W against the 1051 W available from the same string under uniform illumination [20-23].




(a)




(b)

Figure 1-9: (a) Power–voltage characteristic of a string of three series-connected modules of the type in Table 1-3, each protected by a bypass diode, under irradiances of 1000, 600 and 300 W/m², compared with the uniformly illuminated case. Three local maxima appear; the global maximum lies at the central peak [13], [15]; bypass-diode behaviour as described in [20-23]. (b) The same multi-peak characteristic as reported for a partially shaded array, with two local peaks and the global peak; reproduced from [122], Fig. 2.

The consequence for tracking is structural rather than incremental. The peak condition of equation (1.6) is local - it is satisfied at every one of the maxima in Figure 1-9 - so a controller that simply climbs the local gradient has, by its own stopping criterion, no way to distinguish the global peak from an impostor, and may settle indefinitely on a local maximum, forfeiting a substantial fraction of the power actually available [23, 24]. This single limitation - the inability of local, gradient-following methods to guarantee global convergence under partial shading - is the central technical motivation for the global-search and intelligent MPPT families surveyed in Chapter 3.

**Example 1.1 - Power at stake under partial shading (2S-2P array of [102])**

**Given data**

- Four 5 W modules connected in a 2S-2P arrangement, simulated in MATLAB/Simulink [102].
- Case I, uniform 1000 W/m²: MPP at 19.09 V, 20 W.
- Case II, modules M3 and M4 at 600 W/m²: MPP at 18.67 V, 15.76 W.
- Case III, non-uniform irradiance (1000, 800 and 600 W/m² on different modules): LMPP at 8.87 V, 9.17 W; GMPP at 19.44 V, 14.65 W.

**Formulas**

Power forfeited by a tracker locked on the LMPP: $(P_{GMPP} - P_{LMPP})/P_{GMPP}$
Power reduction caused by shading: $(P_{uniform} - P_{MPP})/P_{uniform}$

**Calculation**

Tracker locked on the LMPP (Case III): $(14.65 - 9.17)/14.65 = 0.374$
Shading, Case II: $(20 - 15.76)/20 = 0.212$
Shading, Case III: $(20 - 14.65)/20 = 0.268$

**Result**

- A local tracker that settles on the LMPP of Case III loses 37.4 % of the power still available.
- The shading itself has reduced the available power by 21.2 % (Case II) and 26.8 % (Case III).

**Interpretation:** in Case III the loss caused by the tracker is larger than the loss caused by the shading. The same order of magnitude follows from the three-module string of Figure 1-9, where settling on the first peak instead of the global one forfeits (447 − 335)/447 = 25% of the available power. These figures quantify why global search capability is the criterion that separates the MPPT families under partial shading (Chapter 3).

**Source:** [102]

## 1.6 Photovoltaic System Configurations

A photovoltaic generator is always embedded in a larger electrical system, and the architecture of that system constrains what may be asked of the conversion and tracking stage.

**Stand-alone systems** supply an isolated load without a grid connection and therefore require energy storage (typically a battery) to carry the load through periods of insufficient sunlight [25, 26]. Because the battery voltage rarely coincides with the array's maximum-power voltage, a charger stage is interposed to track the peak; moreover, the tracking objective is here conditional rather than absolute, since the controller must relinquish the maximum power point whenever the available PV power exceeds what the load and the battery's charging regime can absorb [25]. A laboratory-scale stand-alone configuration of this kind - a small PV array, a DC–DC converter with a microcontroller-based MPPT controller and a resistive load - is shown in the photograph of Figure 3-22 [102].

**Grid-connected systems** absorb whatever power the array produces, so maximum-power extraction can, in principle, be pursued unconditionally; the price is paid on the output side, where a grid-synchronised, harmonic-compliant AC current must be synthesised. Two architectures divide the field: in the single-stage arrangement one inverter performs both tracking and grid-

current control, while in the two-stage arrangement - the reference architecture adopted throughout this thesis - a dedicated DC–DC converter tracks the array while feeding a regulated DC link from which a separate inverter stage works, the link capacitor decoupling the two control problems [27]. Figure 1-10 contrasts the two circuits. Within the grid-connected family, the granularity of conversion - how many modules share one converter - spans a spectrum from central (one tracker for the whole array, cheapest but fully exposed to the mismatch penalty of Section 1.5.3), through string and *multi-string* (independent tracking per string, the dominant arrangement in European installations), to module-integrated conversion (one converter per module, recovering mismatch loss at its source at the cost of the highest converter count and the largest required voltage gain) [11, 28, 29].

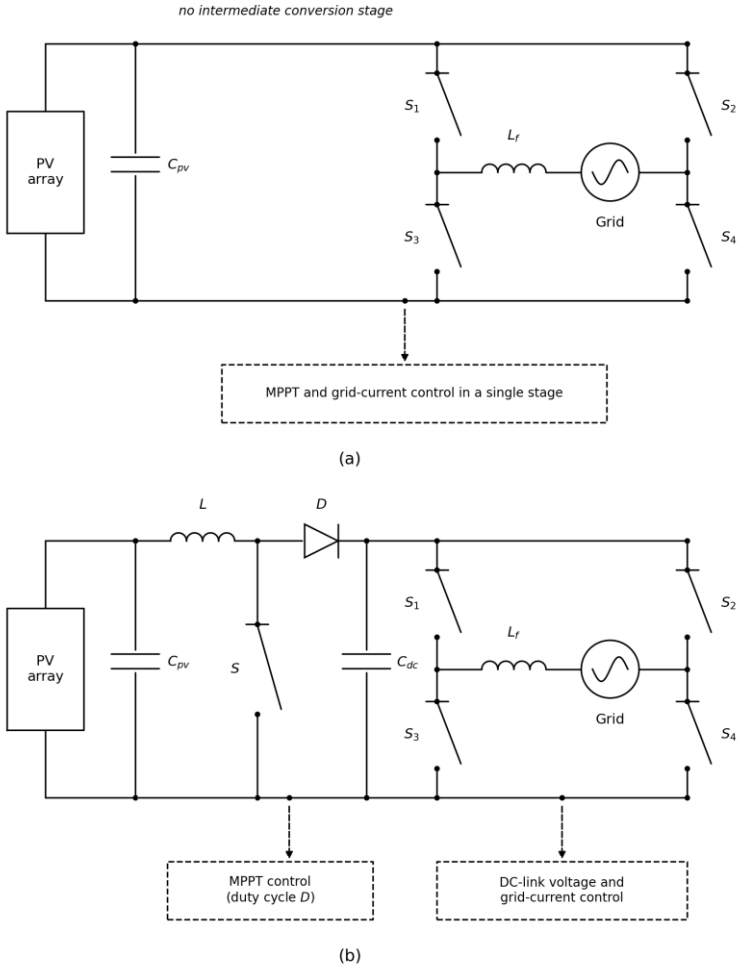



Figure 1-10: Circuit schemes of the two grid-connected architectures. (a) Single-stage: the array feeds the inverter bridge $S_1$–$S_4$ directly, the input capacitor $C_{pv}$ also acting as the DC link, so one controller must perform maximum power point tracking and grid-current regulation simultaneously [11]. (b) Two-stage: a boost converter (L, S, D) tracks the array and charges the DC-link capacitor $C_{dc}$, from which the inverter operates; the link capacitor decouples the tracking problem from grid-current control, and each stage carries its own controller [28, 29]. $L_f$ is the grid-side filter inductance.

**Hybrid systems** combine the photovoltaic source with at least one other generator (fuel cell, wind, diesel) and usually with storage, typically through a multi-input converter; here maximum power point tracking is one control objective among several, engaged or subordinated according to the overall power balance [30].

Table 1-4 summarises the grid-connected granularity spectrum, which recurs throughout Chapter 2 because it fixes the voltage gain that the DC–DC stage must provide: a single module operates at roughly 30–45 V at its maximum power point, a full string may reach several hundred volts, and a single-phase grid-tied inverter typically requires a DC link on the order of 350–400 V. Conversion from a short string or a single module therefore demands a high step-up ratio, while conversion from a full-length string may require little or no boost - the distinction that organises the converter survey of the next chapter.

Table 1-4: Conversion granularity in grid-connected photovoltaic systems (compiled from [28, 29]).

| Architecture | Tracking granularity | Shading resilience | Typical voltage gain required |
|---|---|---|---|
| Central | One tracker for the whole array | Lowest | Low to moderate |
| String | One tracker per string | Moderate | Low to moderate |
| Multi-string | One tracker per string, shared inverter | Moderate–high | Low to moderate |
| Module-integrated | One tracker per module | Highest | High (module-to-link gain) |

## 1.7 The Role of Power Electronics: the Converter as Actuator

The preceding sections established that a photovoltaic generator has no intrinsic mechanism for holding itself at its maximum power point, and that the point itself moves continuously with irradiance, temperature and shading pattern. Closing this gap is the joint task of a DC–DC converter and a control algorithm, and the relationship between the two is the organising idea of this thesis.

A switching DC–DC converter, by varying its duty cycle $D$, changes the apparent resistance that the downstream circuit presents at the array terminals. For an ideal boost converter operating in continuous conduction mode, for instance, the static voltage gain is a function of duty cycle alone,

$$M(D) = \frac{V_o}{V_{pv}} = \frac{1}{(1 - D)} \tag{1.7}$$

and, neglecting losses, the resistance seen at the converter input is

$$R_{pv} = \frac{V_{pv}}{I_{pv}} = (1 - D)^2 \cdot R_L \quad (1.8)$$

so that varying $D$ sweeps the emulated input resistance, and with it the array operating point, across the entire I–V curve [31]. This is the physical basis on which every MPPT algorithm surveyed in Chapter 3 ultimately acts: whatever its internal logic, an MPPT algorithm's final product is a duty-cycle command (or a voltage/current reference that becomes one), and the physical consequence of that command is produced entirely by the converter. The DC–DC converter is, in this precise sense, the actuator of the tracking loop, illustrated in Figure 1-11: it performs voltage adaptation between the array and the downstream DC bus, source–load decoupling, and part of the power-conditioning and protection function of the system, while simultaneously being the plant through which the tracking algorithm moves the operating point [32, 33].

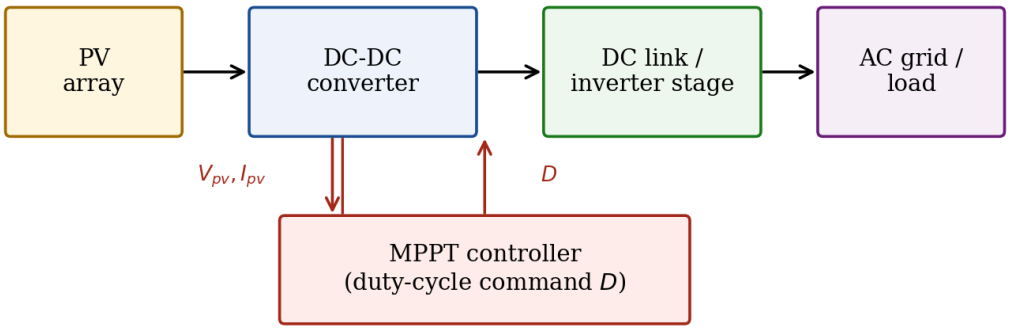



Figure 1-11: Two-stage photovoltaic conversion chain, showing the DC–DC converter as the actuator through which the MPPT controller imposes the operating point of the array.[32, 33].

Equation (1.7) also exposes the principal practical limitation of the conventional boost stage that motivates much of Chapter 2: the ideal gain diverges as $D$ approaches unity, but in a real converter the parasitic resistances of the inductor, switch and diode cause the gain to reach a finite maximum and then collapse, with extreme duty cycles additionally associated with severe diode reverse-recovery losses and high device voltage stress [34, 35]. Because a PV array's terminal voltage is typically well below what a grid-tied inverter or a high-voltage DC bus requires, this limitation is encountered routinely rather than exceptionally, and it has driven an extensive body of literature on high-gain converter topologies, surveyed in Chapter 2.

The literatures on converter design and on tracking algorithms have, however, historically developed largely in parallel: converter papers routinely treat MPPT as an external black box supplying a duty-cycle signal, while MPPT papers routinely treat the converter as a black box in turn - most often a plain boost stage included only because the simulation requires something for

the algorithm to control [32, 33]. Because the quantities by which tracking performance is judged (convergence time, steady-state ripple, energy lost during a transient) are joint properties of the algorithm and the converter, not properties of the algorithm alone, a tracking improvement demonstrated on one power stage cannot automatically be assumed to transfer to another. This observation, developed with supporting evidence in Chapters 2 to 4, is the central critical thread of the present review.

## 1.8 Scope and Objectives of the Thesis

The objective of this thesis is to provide a structured, critical bibliographic review of the DC–DC converter topologies and the Maximum Power Point Tracking algorithms used in photovoltaic systems, with three more specific aims:

1. to survey the converter topologies most relevant to photovoltaic power conditioning, from the classical non-isolated stages through the high-gain families developed to overcome the classical boost converter's gain ceiling (Chapter 2);
2. to survey and critically compare the MPPT algorithms reported in the literature, from the classical perturb-and-observe and incremental-conductance methods through intelligent, metaheuristic, hybrid and learning-based techniques, with particular emphasis on the algorithms most active in the recent literature (Chapter 3, the central chapter of this thesis);
3. to bring the two literatures into a single frame, so that the trade-offs between converter-level properties (gain, ripple, dynamics) and controller-level properties (tracking speed, accuracy, robustness, computational cost) can be compared explicitly, and to draw conclusions on which combinations the current state of the art supports and which questions remain open (Chapter 4).

The review is restricted to conventional crystalline-silicon arrays and to DC–DC conversion stages and the MPPT strategies that act through them; it excludes inverter-side grid-code compliance and power-quality analysis except where these constrain the DC stage, and it does not extend to tracking strategies developed specifically for emerging cell technologies. Within the MPPT literature, particular attention is given to work published over the last decade, with earlier sources retained where they establish a method or a result that later work depends upon. The thesis is a literature review rather than an experimental study: no new converter is fabricated and no new algorithm is proposed; its contribution lies in the organisation, synthesis and critical comparison of the existing published record.

## 1.9 Organisation of the Thesis

The remainder of the thesis is organised as follows. Chapter 2 surveys DC–DC converter topologies for photovoltaic applications: the classical non-isolated converters, the high-gain topologies developed to overcome their voltage-gain limitations, a brief treatment of isolated topologies, and the converter-selection criteria - including those that become visible only once the converter is read as the actuator of an MPPT loop. Chapter 3, the central chapter of the thesis, surveys the state of the art in MPPT: the maximum-power-point concept and the performance criteria used to judge tracking methods; the classical algorithms (perturb and observe, incremental conductance, constant-voltage/current and fractional methods); the advanced and intelligent methods (fuzzy logic, artificial neural networks, metaheuristic optimisation); and the most recent techniques reported in the literature (hybrid two-stage schemes, machine-learning and reinforcement-learning approaches, model predictive control and sliding-mode control). Chapter 4 draws the two surveys together: it compares MPPT algorithms and converter topologies critically against the performance criteria established in the preceding chapters, discusses what the literature does and does not yet establish about the converter–algorithm interface, and concludes with the directions the recent literature suggests for future work.

# 2 CHAPTER 2 - DC-DC CONVERTERS FOR PHOTOVOLTAIC APPLICATIONS

Chapter 1 established that the DC–DC converter is the actuator through which every Maximum Power Point Tracking (MPPT) algorithm imposes an operating point on the photovoltaic (PV) array, and that its practical voltage-gain ceiling is what has driven an extensive body of literature on high-gain topologies. This chapter surveys that literature: Section 2.1 fixes the classification and the analytical toolkit used throughout; Sections 2.2 and 2.3 survey the non-isolated and isolated converter families; Section 2.4 surveys the high step-up techniques developed to overcome the classical boost converter's gain limitation; and Section 2.5 develops the selection criteria against which a converter is judged, including the criteria that only become visible once the converter is read as the actuator of a control loop rather than merely as a power-processing circuit.

## 2.1 Classification and Analytical Toolkit

### 2.1.1 The isolation and switching-regime axes

The converter literature organises itself along two largely orthogonal axes. The first is galvanic isolation. A non-isolated converter connects input and output through a common conductive path and is built from inductors, capacitors, switches and diodes alone; its simplicity, low component count and cost explain both its industrial ubiquity and the volume of research devoted to it [33, 34]. An isolated converter interposes a high-frequency transformer, which supplies two distinct benefits that are worth keeping separate: galvanic separation itself (independent grounds, structurally answering safety and leakage-current requirements), and a turns ratio that acts as an additional, duty-cycle-independent gain lever [34, 36]. The price is the transformer's leakage inductance (voltage spikes at turn-off, requiring snubber or clamp circuitry) and a size/cost penalty relative to non-isolated counterparts [33, 34]. Figure 2-1 contrasts the two classes on the same buck–boost conversion function.

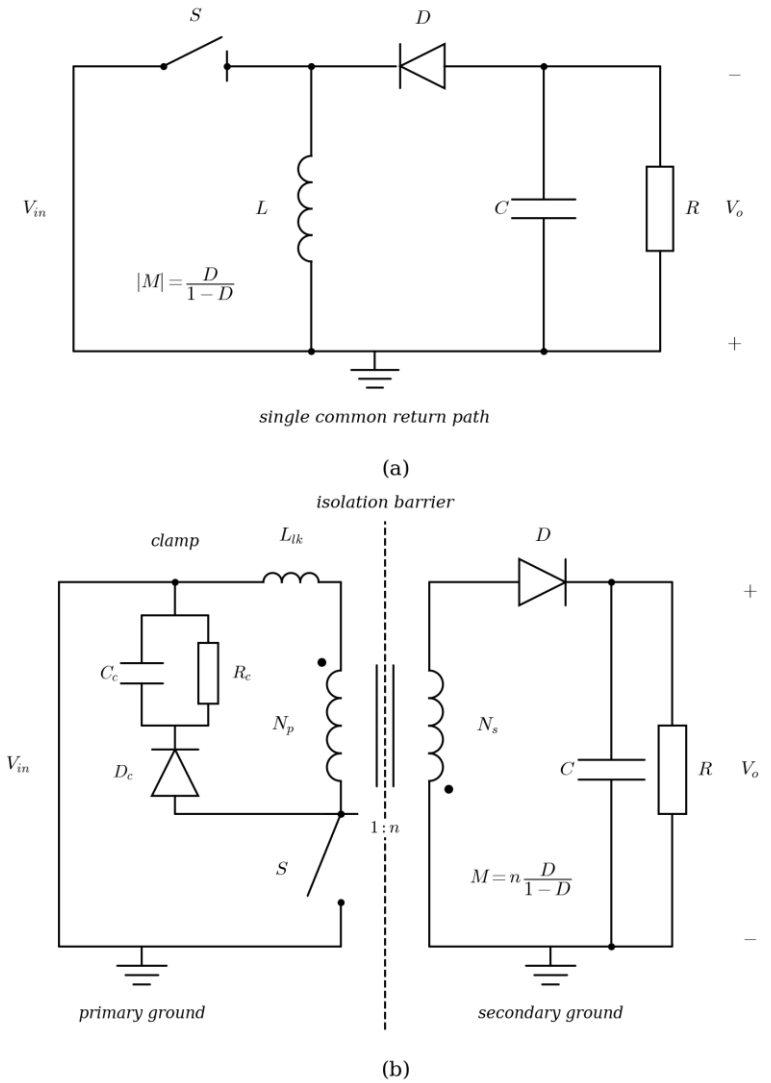



Figure 2-1: The isolation axis illustrated on the same conversion function. (a) Inverting buck–boost converter without isolation: input and output share a single return path, and the gain |M| = D/(1 − D) is set by the duty cycle alone [31], [33], [119]. (b) Its isolated counterpart, the flyback converter, in which the inductor becomes a coupled inductor with turns ratio 1 : n: the isolation barrier separates the primary and secondary grounds, the gain M = nD/(1 − D) acquires the duty-cycle-independent factor n, and the leakage inductance $L_{lk}$ requires a clamp ($D_c$, $C_c$, $R_c$) to absorb the voltage spike at switch turn-off [31], [34], [115].

The second axis is the switching regime. In a hard-switched converter the semiconductor commutates while carrying both voltage and current, so every transition dissipates energy; because this loss grows with switching frequency, it places a practical ceiling on frequency and hence a floor under the size of the passive components. Soft-switching techniques (zero-voltage or zero-current switching) remove this transition loss by arranging for the device to commutate with near-zero voltage or current, permitting higher switching frequencies and smaller magnetics at the cost of additional components and more elaborate, often variable-frequency control [34, 37]. Figure 2-2 illustrates the difference at the level of a single commutation. A property worth noting for the photovoltaic application specifically: the proper operation of resonant, load-dependent soft-switching converters is tied to the operating point relative to a resonant frequency, which sits

uneasily with a PV input whose voltage and power sweep continuously with irradiance and temperature - an efficiency figure quoted for a soft-switched converter at its resonant sweet spot says little about photovoltaic service unless the surrounding operating range is reported with it [34].

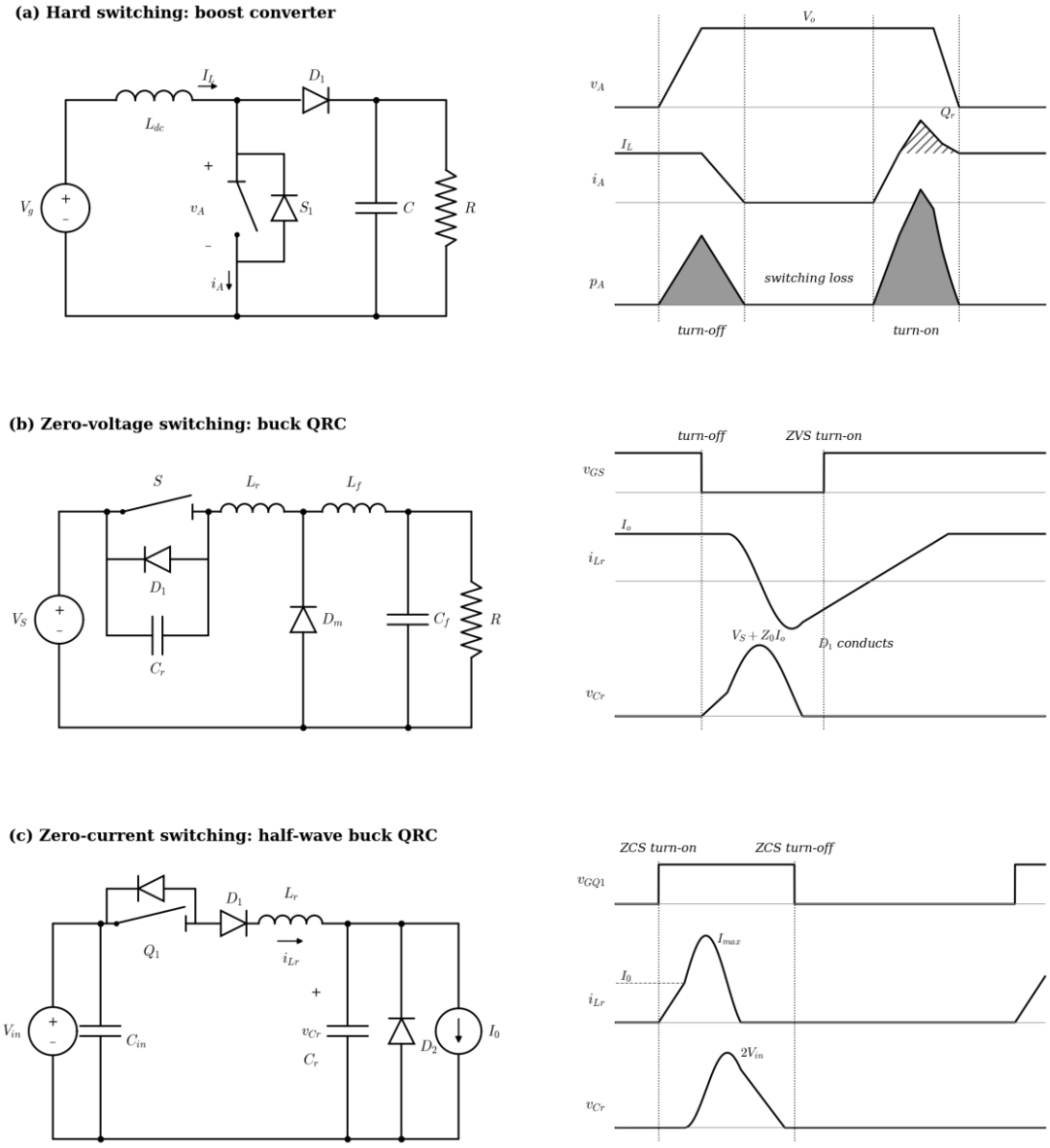



Figure 2-2: The switching-regime axis illustrated on three complete converters, each with the commutation waveforms reported for it [34, 37]. (a) Hard switching in a boost converter [116]: at turn-off the switch voltage $v_A$ rises to $V_o$ while the current $i_A$ is still flowing, and at turn-on the current, including the reverse-recovery charge $Q_r$ of $D_1$, rises while the voltage is still high; the shaded overlap $p_A = v_A i_A$ is the energy lost per commutation. (b) Zero-voltage switching in a buck quasi-resonant converter [117]: $C_r$ in parallel with S slows the voltage rise at turn-off, the $L_r$–$C_r$ resonance returns $v_{Cr}$ to zero, and S is turned on while its antiparallel diode $D_1$ conducts, that is, at zero voltage; the peak switch voltage is $V_S + Z_0 I_o$. (c) Zero-current switching in a half-wave L-type buck quasi-resonant converter (QRC) [118]: $L_r$ in series with $Q_1$ limits the current slope at turn-on, the resonance with $C_r$ returns $i_{Lr}$ to zero, and the series diode $D_1$ blocks reverse current, so that $Q_1$ is turned off at zero current. Waveforms are qualitative and not to scale.

A photovoltaic example of resonant soft switching is the ZVS Zeta converter of Raj et al. [100], shown with its MPPT loop in Figure 2-. A resonant inductor $L_r$ and capacitor $C_r$, together with a diode across the switch, make the switch turn on at zero voltage; the network is designed from the resonant frequency $f_r = 1/(2\pi\sqrt{(L_rC_r)})$, the characteristic impedance $Z_0 = \sqrt{(L_r/C_r)}$ and the quality factor $Q = R/Z_0$, and ZVS operation requires the switching frequency to remain below $f_r$ [100]. Example 2.1 checks this condition for the published design. The same study applies this resonant network to a SEPIC converter, shown in Figure 2-, where a capacitor and a diode are again connected in parallel with the switch and an inductor in series with it [100].

**Example 2.1 - Resonant network of the ZVS Zeta converter of [100]**

**Given data**

$L_r$ = 848.82 µH; $C_r$ = 190.985 nF; load resistance $R$ = 60 Ω; switching frequency $f_s$ = 5 kHz (Appendix A of [100])

**Formulas**

$f_r = 1/(2\pi\sqrt{(L_rC_r)})$ $f_{ns} = f_s/f_r$ $Z_0 = \sqrt{(L_r/C_r)}$ $Q = R/Z_0$

**Calculation**

$L_rC_r = 848.82\times10^{-6}$ H × $190.985\times10^{-9}$ F = $1.621\times10^{-10}$ s²

$f_r = 1/(2\pi \times 1.273\times10^{-5}$ s) = 12.5 kHz; $f_{ns} = 5/12.5 = 0.40$

$Z_0 = \sqrt{(4444\ \Omega^2)} = 66.7\ \Omega$; $Q = 60/66.7 = 0.90$

**Result**

$f_r$ = 12.5 kHz = 2.5 $f_s$: the normalised switching frequency is 0.40, and the ZVS condition $f_s < f_r$ is satisfied at the design point.

**Interpretation:** the margin is fixed at a single operating point (17 V, 0.58 A, 60 Ω). [100] reports the performance at 1000 W/m² and for one irradiance step to 1200 W/m², so - as noted above for resonant converters in general - the behaviour over the full photovoltaic operating range is not documented.

**Source:** [100]

Two further axes, secondary to the two above but relevant at particular points in this chapter, complete the classification. Power-flow direction separates unidirectional converters, sufficient for a pure generation path, from the bidirectional family required wherever storage is coupled to the array (Section 2.3). Port count separates the single-input, single-output converters that are the subject of most of this chapter from multi-input structures that interface several sources - the photovoltaic array, a fuel cell, a battery - through one shared conversion stage, relevant to the hybrid system configurations introduced in Section 1.6 but outside the principal scope of the present review.

### 2.1.2 Steady-state balance, gain laws and the conduction-mode boundary

A switched-mode converter alternates, at switching frequency $f_s = 1/T_s$, between charging and discharging states, the semiconductor switch conducting for a fraction $D = t_{on}/T_s$ of each period - the duty cycle, which is the control input that pulse-width modulation adjusts. In steady state, the average voltage across every inductor and the average current through every capacitor must both

vanish over one switching period (the volt-second and charge balances); applying this to the classical converters gives the ideal continuous-conduction-mode (CCM) gain laws

| | |
|---|---|
| $\text{buck: } M(D) = \frac{V_o}{V_{in}} = D$ | (2.1) |
| $\text{boost: } M(D) = \frac{V_o}{V_{in}} = \frac{1}{(1 - D)}$ | (2.2) |
| $\text{buck} - \text{boost, Ćuk, SEPIC, Zeta: } \lvert M(D) \rvert = \frac{D}{(1 - D)}$ | (2.3) |

with the buck–boost and Ćuk delivering equation (2.3) with inverted output polarity, and the SEPIC and Zeta delivering it non-inverted [31]. Read as control characteristics, these equations are the plant through which every MPPT algorithm in Chapter 3 acts: they are nonlinear, so a fixed duty-cycle perturbation moves the operating point by very different amounts at different $D$.

The ideal boost gain of equation (2.2) diverges as $D \to 1$, but a real converter does not deliver unbounded gain: carrying the inductor's series resistance $r_L$ through the analysis gives

| | |
|---|---|
| $M(D) = \left[\frac{1}{(1 - D)}\right] \cdot \frac{1}{\left[1 + \frac{r_L}{((1 - D)^2 \cdot R)}\right]}$ | (2.4) |

which reproduces the gain characteristic the literature reports: the real curve follows the ideal law at moderate duty cycles, then peels away, passes through a maximum, and collapses. The maximum occurs at $D = 1 - \sqrt{(r_L/R)}$, where the gain reaches only $1/\left(2\sqrt{(r_L/R)}\right)$ - for a parasitic ratio $rL/R$ of just 1%, the ceiling is a gain of five, reached at $D = 0.90$ [38, 39]. This parasitic-limited ceiling is the quantitative origin of the entire high step-up literature surveyed in Section 2.4.

The scale of the problem is worth making concrete. Section 1.6 established that a single crystalline-silicon module operates at roughly 33 V at its maximum power point (Table 1-1), while a single-phase grid-tied inverter typically requires a DC link on the order of 380 V - a required gain of approximately 11.5. Reaching such a ratio with the ideal boost law of equation (2.2) alone would require $D \approx 0.91$, deep inside the parasitic collapse region that equation (2.4) describes, where conduction losses, device stress and diode reverse-recovery problems converge to erode efficiency

precisely as gain is most needed [40, 41]. Module-level and short-string architectures therefore cannot rely on the conventional boost stage alone, and this arithmetic - not a preference for exotic circuits - is what motivates the high step-up literature of Section 2.4.

A second, equally important limitation is the boundary between continuous conduction mode (CCM), in which the inductor current never falls to zero, and discontinuous conduction mode (DCM), in which it does. Defining the dimensionless conduction parameter $K = 2 \cdot L \cdot f_s / R_L$, a boost converter remains in CCM if and only if

$$K > K_{\text{crit}}(D) = D \cdot (1 - D)^2 \quad (2.5)$$

whose maximum value, 4/27, occurs at $D = 1/3$ [32]. When this inequality is violated, the converter enters DCM and the conversion ratio becomes a function of $L$, $f_s$ and $R_L$ as well as of $D$ - a materially different relation from equation (2.2). This distinction matters directly for MPPT: a tracking algorithm that infers the array voltage from the duty cycle and the DC-link voltage through the CCM relation is operating on a model that no longer describes the hardware once the converter crosses into DCM, and the crossing is more likely for a PV-fed converter than the conventional load-dependent argument suggests, because at low irradiance the array current itself is small, so the inductor ripple is large relative to the mean. Noman et al. showed that a boost stage sized for CCM at the maximum power point can nevertheless operate in DCM near open circuit at any irradiance, and even within the maximum-power region at irradiance below roughly 250 W/m² [42]. Because a perturb-and-observe search conventionally begins near open circuit, the algorithm may start each acquisition inside a region where its own voltage relation is already invalid - a coupling mechanism developed further in Chapters 3 and 4.

Ripple and component stress complete the analytical toolkit. For the boost inductor, the current ripple follows directly from the charging interval, and the output-capacitor voltage ripple from the charge surrendered while the diode blocks conduction:

$$\Delta i_L = V_{in} \cdot \frac{D}{(L \cdot f_s)} \quad (2.6)$$

$$\Delta v_o = V_o \cdot \frac{D}{(R \cdot C \cdot f_s)} \quad (2.7)$$

Both shrink with inductance/capacitance and with switching frequency, but design headroom is not free: raising the frequency to shrink the passives raises the switching loss, and undersizing the inductor pushes the converter toward the DCM boundary of equation (2.5). Design practice commonly sizes the inductor so that $\Delta i_L$ falls between roughly twenty and forty per cent of the average inductor current at the rated operating point, which simultaneously bounds the ripple and keeps the converter clear of the conduction-mode boundary [43]. At the array terminals, ripple is not a cosmetic quantity - because the power–voltage characteristic is curved near its peak (Section 1.4), a ripple of finite amplitude extracts strictly less power than the corresponding mean operating point, and it blurs the very voltage/current measurements on which the tracking computation runs [44, 45]. The photovoltaic distinction is which side of the converter the ripple reaches: topologies whose input port is an inductor (boost, Ćuk, SEPIC) draw a continuous, smoothed input current, while the buck, buck–boost and Zeta place a switch at the input and draw pulsating current [6, 46].

Device stress - the peak voltage a switch or diode must block and the peak current it must carry - fixes the required semiconductor voltage class and hence conduction loss and cost; in the boost converter the switch and diode block the full output voltage, while in the buck–boost family they block the sum of input and output voltages. A higher blocking-voltage requirement forces a higher-voltage-class switch, whose larger on-resistance raises conduction loss - the chain that connects device stress to converter cost and efficiency, and that organises the selection criteria of Section 2.5 [41].

## 2.2 Non-Isolated Converter Topologies

The six basic non-isolated converters - buck, boost, buck–boost, Ćuk, SEPIC and Zeta - are, structurally, variations of a single three-terminal switching cell, and they remain the platform on which the great majority of MPPT studies are conducted [47]. Figure 2- shows three representative circuits; Table 2-1 collects the comparison that organises the remainder of this section.

The buck converter (equation (2.1)) places the switch at the input, so its input current is pulsating (chopped) while its output current is smooth. This is the wrong orientation for a photovoltaic front end, since a chopped input current must be filtered before the array sees it or the tracking measurement is blurred; a buck-based interface also cannot reach the maximum power point once the equivalent load resistance exceeds an irradiance-dependent bound, and it carries the heaviest small-signal control burden of the classical set (four time-varying parameters, lightly damped) [18, 28].

The boost converter (equation (2.2)) inverts this arrangement: continuous input current, pulsating output current - the right orientation for a PV source, and the reason it is the default front end of the two-stage grid-connected architecture [27]. In a direct comparison of converter dynamics as MPPT interfaces, the boost's small-signal model carries only a single time-varying parameter (the array's own dynamic resistance), is well damped, and achieves the widest control bandwidth at the lowest implementation cost of the converters compared [18]. Its liabilities are exactly those developed in Section 2.1.2: a parasitic-limited gain ceiling, switch/diode stress at the full output voltage, and the CCM/DCM crossing.

The buck–boost family (equation (2.3)) trades a more elaborate circuit for range: reflecting the output load $R_o$ through the ideal gain law gives the resistance the converter presents to the array,

$$R_{in} = R_o \cdot \left[\frac{(1 - D)}{D}\right]^2 \quad (2.8)$$

which sweeps the *entire* positive axis as $D$ moves from 0 to 1 - unlike the boost relation of equation (1.8), which is bounded above by $R_L$. A buck–boost-class stage can therefore place the array operating point anywhere on its I–V curve regardless of irradiance, and the comparative literature accordingly names the buck–boost, Ćuk, SEPIC and Zeta converters collectively as the preferred class for MPPT service on precisely this ground [28, 33]. Figure 2- collects the six basic circuits in a common notation, with source and load: the three of Figure 2- redrawn, and the Ćuk, SEPIC and Zeta converters that complement them:

- The Ćuk converter is the most thoroughly repaired member of the family: two inductors, one at each port, give continuous current on both the array side and the load side, and comparative evaluations report it achieving the highest tracking efficiency among the conventional converters [33, 47].
- The SEPIC converter keeps the continuous input inductor of the Ćuk while restoring non-inverted output polarity and a ground-referenced switch, which is why it recurs wherever the array voltage may lie on either side of the bus voltage - the stand-alone battery charger of Chiang et al. selected a SEPIC stage for exactly this combination of step-up/step-down capability, positive output, and low input-current ripple for precise tracking [25].
- The Zeta converter is the SEPIC's dual (pulsating input, continuous output) and is nearly equivalent to it in efficiency, so the choice between the two is a placement question -

smoothness where the source needs it (SEPIC) or where the load needs it (Zeta) - rather than a performance ranking [33, 47].

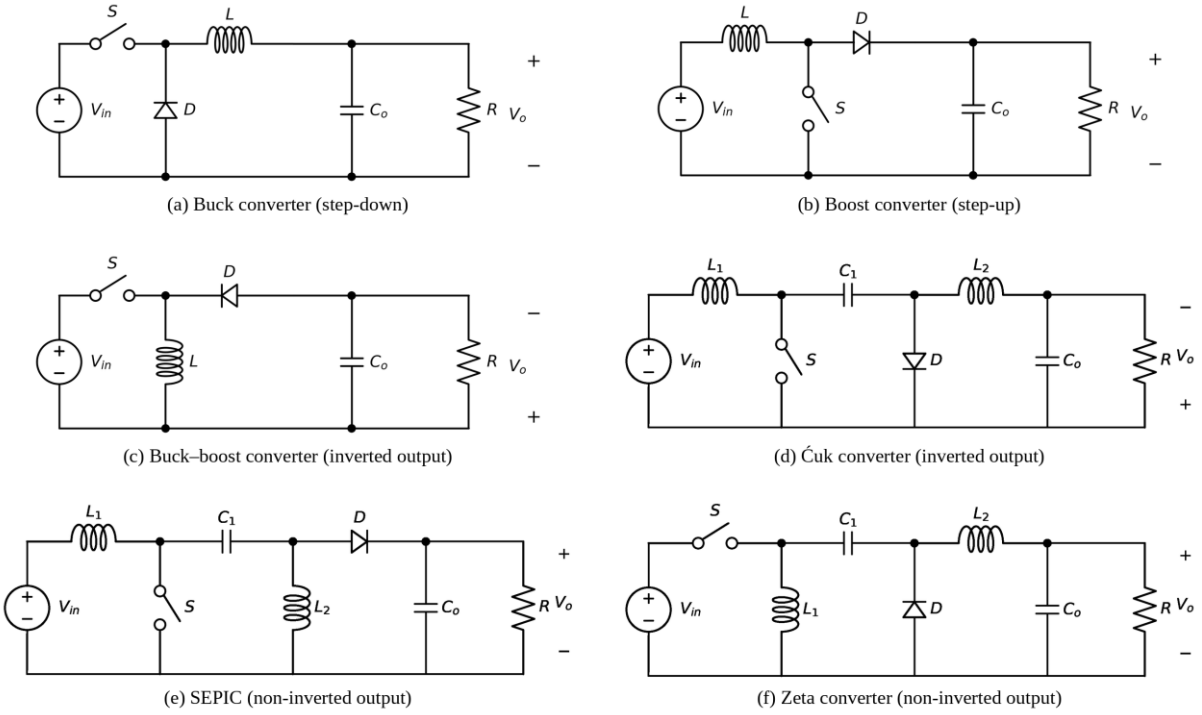



Figure 2-3: Circuit diagrams of the basic non-isolated converters in a common notation, with source and load: (a) buck, (b) boost, (c) inverting buck–boost, (d) Ćuk, (e) SEPIC and (f) Zeta. S: switch; D: diode; L, $L_1$, $L_2$: inductors; $C_1$: energy-transfer capacitor; $C_o$: output capacitor; R: load. Drawn by the author; SEPIC and Zeta topologies as in [100], Ćuk topology as in [17]. Buck, boost and buck–boost topologies as in [28, 33].

Table 2-1: Photovoltaic assessment of the six basic non-isolated converters.

| Converter | Ideal CCM gain | Input current | Tracking range | PV interface verdict | Reference(s) |
|---|---|---|---|---|---|
| Buck | $D$ | Pulsating | Bounded by an irradiance-dependent load limit | Requires input filtering; used where bus voltage is reliably below array voltage | [18, 28] |
| Boost | $\frac{1}{(1-D)}$ | Continuous | Mirror bound at low irradiance | Best control dynamics of the set; default two-stage front end; gain-limited | [18, 27] |
| Buck–boost | $\frac{D}{(1-D)}$ | Pulsating | Unbounded (eq. 2.8) | Full-range tracking; weakest of the buck–boost class on ripple | [28, 33] |
| Ćuk | $\frac{D}{(1-D)}$ | Continuous | Unbounded | Smoothest of the set; best reported conventional efficiency | [33, 47] |
| SEPIC | $\frac{D}{(1-D)}$ | Continuous | Unbounded | Standard choice where array voltage may lie on either side of the bus | [25] |
| Zeta | $\frac{D}{(1-D)}$ | Pulsating | Unbounded | SEPIC's mirror image; suited to a demanding load rather than source | [33, 47] |

The Zeta and SEPIC stages are also the subject of a study in which the switching regime and the tracking algorithm are varied together. Raj et al. [100] compared conventional (hard-switched) and ZVS versions of both converters, fed by a single PV panel and controlled by P&O or INC (denoted IC in [100]), in MATLAB simulation at 1000 W/m² and 25 °C, and verified the Zeta–INC combination experimentally with a real-time simulator (OP-5142) and oscilloscope measurements. Figure 2- shows the PV-fed ZVS Zeta converter with its control loop. In the simulated waveforms the input current of the Zeta converter is discontinuous whereas that of the SEPIC is continuous, and the output-voltage ripple of the Zeta is lower than that of the SEPIC because of the series output inductor $L_2$ [100] - the port-continuity pattern summarised in Table 2-1. Example 2.2 quantifies the efficiency effect of soft switching reported in the same study, and Example 2.3 shows the sizing of two of the basic converters for a common conversion ratio.

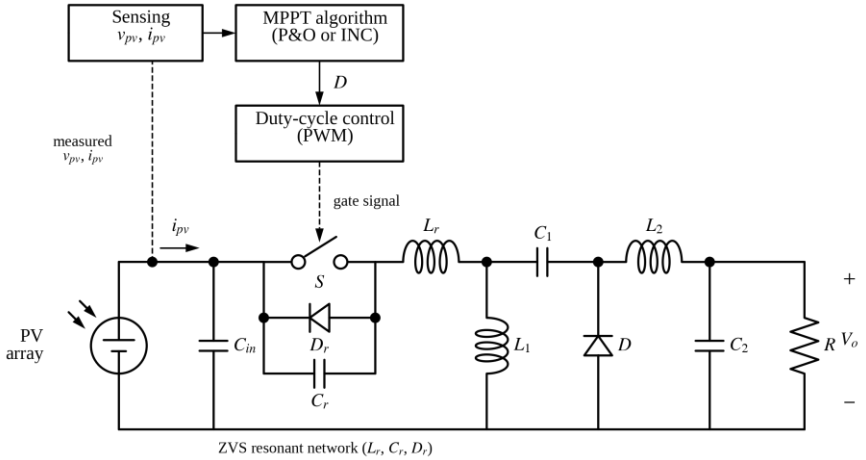



Figure 2-4: Photovoltaic-fed zero-voltage-switching (ZVS) Zeta converter with its MPPT control loop: the MPPT algorithm (P&O or INC) processes the measured array voltage and current and sets the duty cycle $D$ of switch S; $L_r$, $C_r$ and $D_r$ form the resonant network that provides zero-voltage turn-on [100].

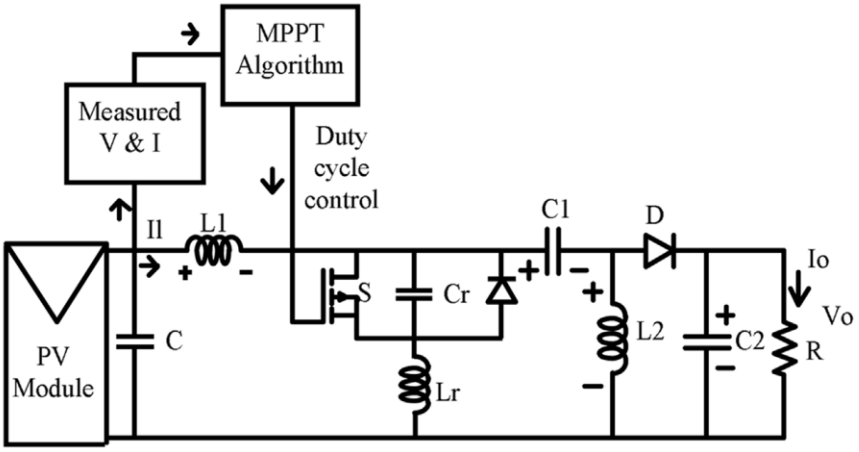



Figure 2-5: Solar-fed zero-voltage-switching (ZVS) SEPIC converter with its MPPT control loop: the measured array voltage and current feed the MPPT algorithm, which sets the duty cycle of switch S; the capacitor $C_r$ and the diode connected in parallel with S, together with the inductor $L_r$ in series with it, provide zero-voltage switching [100], Fig. 2(b).

**Example 2.2 - Efficiency gain of soft switching in a PV-fed Zeta converter [100]**

**Given data**

- Simulation with INC at 1000 W/m² and 25 °C (Table 1 of [100]): conventional Zeta $P_{in}$ = 9.2276 W, $P_{out}$ = 8.672 W; ZVS Zeta $P_{in}$ = 9.2276 W, $P_{out}$ = 9.055 W.
- Experiment with INC: conventional Zeta $P_{in} \approx 9.2$ W, $P_{out}$ = 8.6 W; ZVS Zeta $P_{out}$ = 9.0 W.

**Formulas**

$\eta = P_{out}/P_{in}$ $P_{loss} = P_{in} - P_{out}$

**Calculation**

Conventional: $\eta = 8.672/9.2276 = 93.98$ %; $P_{loss} = 0.556$ W
ZVS: $\eta = 9.055/9.2276 = 98.13$ %; $P_{loss} = 0.173$ W
Loss reduction: $(0.556 - 0.173)/0.556 = 69$ %
Experiment: $8.6/9.2 = 93.5$ % and $9.0/9.2 = 97.8$ %

**Result**

- With INC, soft switching raises the Zeta efficiency by about 4.1 percentage points in simulation and 4.3 points in the experiment.
- Under P&O the reported gains are 1.97 points (Zeta) and 7.23 points (SEPIC); under INC the SEPIC gains only 0.41 points [100].

**Interpretation:** the same resonant network yields gains between 0.41 and 7.23 percentage points depending on the converter and on the tracking algorithm - a further instance of the pair-dependence discussed in Section 2.6. The benefit is bought with additional passive components, which [100] identifies as the main drawback of the ZVS circuit, and it is reported at the low switching frequency of 5 kHz used in that study.

**Source:** [100]

**Example 2.3 - Sizing a boost and a Ćuk stage for the same 14 V → 50 V conversion [101]**

**Given data**

- Both converters: input 14 V, output magnitude 50 V, switching frequency 50 kHz [101].
- Boost: load 50 Ω, output ripple $\Delta V_o/V_o$ = 1 %, inductor 25 % above the CCM minimum.
- Ćuk: output power 90 W, inductor ripple 10 % of each mean inductor current, output ripple 1 %, ripple on $C_1$ 5 %.

**Formulas**

Boost: $D = 1 - V_{in}/V_o$ $L_{min} = D(1-D)^2R/(2f_s)$ $C = D/[R(\Delta V_o/V_o)f_s]$
Ćuk: $D = |V_o|/(|V_o| + V_{in})$ (equation (2.3)) $I_{L1} = P_o/V_{in}$ $I_{L2} = P_o/|V_o|$
$L \geq V_{in}D/(f_s\Delta i_L)$ $R = V_o^2/P_o$ $C_1 \geq |V_o|D/(Rf_s\Delta v_{C1})$ $C_2 \geq (1-D)/[8(\Delta V_o/V_o)f_s^2L_2]$

**Calculation**

Boost: $D = 1 - 14/50 = 0.72$; $L_{min} = 0.72 \times 0.28^2 \times 50/(2 \times 50\,000) = 28.2$ µH, hence $L = 35$ µH; $C = 0.72/(50 \times 0.01 \times 50\,000) = 28.8$ µF
Ćuk: $D = 50/64 = 0.781$; $I_{L1} = 6.43$ A, $I_{L2} = 1.8$ A; $R = 27.8$ Ω; $\Delta v_{C1} = 0.05 \times 64$ V $= 3.2$ V
$L_1 \geq 14 \times 0.781/(50\,000 \times 0.643) = 340$ µH; $L_2 \geq 14 \times 0.781/(50\,000 \times 0.18) = 1.22$ mH
$C_1 \geq 50 \times 0.781/(27.8 \times 50\,000 \times 3.2) = 8.8$ µF; $C_2 \geq 0.219/(8 \times 0.01 \times 50\,000^2 \times 1.22\times10^{-3}) = 0.90$ µF

**Result**

| Converter | Duty cycle | Inductance | Capacitance | Power |
|---|---|---|---|---|
| Boost | 0.72 | $L$ = 35 µH | $C$ = 28.8 µF | 50 W |
| Ćuk | 0.781 | $L_1$ = 340 µH, $L_2$ = 1.22 mH | $C_1$ = 8.8 µF, $C_2$ = 0.90 µF | 90 W |

The Ćuk values coincide with those reported in [101]; for the boost capacitor [101] reports about 24 µF, whereas the stated formula and data give 28.8 µF.

**Interpretation:** for the same voltage ratio (3.57) the Ćuk stage needs a larger duty cycle (0.781 against 0.72), because its gain law is $D/(1-D)$ rather than $1/(1-D)$, and seven components instead of five [101]; in exchange it draws continuous current at both ports (Table 2-1). The inductance values are not directly comparable, because the two designs use different criteria (CCM margin at 50 W for the boost, 10% ripple at 90 W for the Ćuk): the example illustrates the design procedure and the orders of magnitude, not a ranking.

**Source:** [101]

## 2.3 Isolated Converter Topologies

Isolated converters interpose a high-frequency transformer and are used in photovoltaic service where galvanic isolation is a genuine requirement - imposed by grid codes or installation class, by the need to suppress common-mode leakage current through the array's parasitic capacitance to ground, or by the management of potential-induced degradation (PID), a voltage-driven loss of module performance whose countermeasures include controlling the array's potential relative to earth, a freedom that a transformerless grid-tied chain does not have [48, 49]. The flyback converter (the isolated member of the buck–boost family) dominates the low-power, module-level end of this space, its transformer acting as a coupled inductor; it is economical (one switch, one magnetic component) but inherits the buck–boost's chopped input current and requires active-clamp or snubber circuitry to manage leakage-inductance voltage spikes [29, 34]. The basic flyback with a passive clamp appears in Figure 2-1(b); Figure 2-3 shows the active-clamp variant together with its chopped input current.

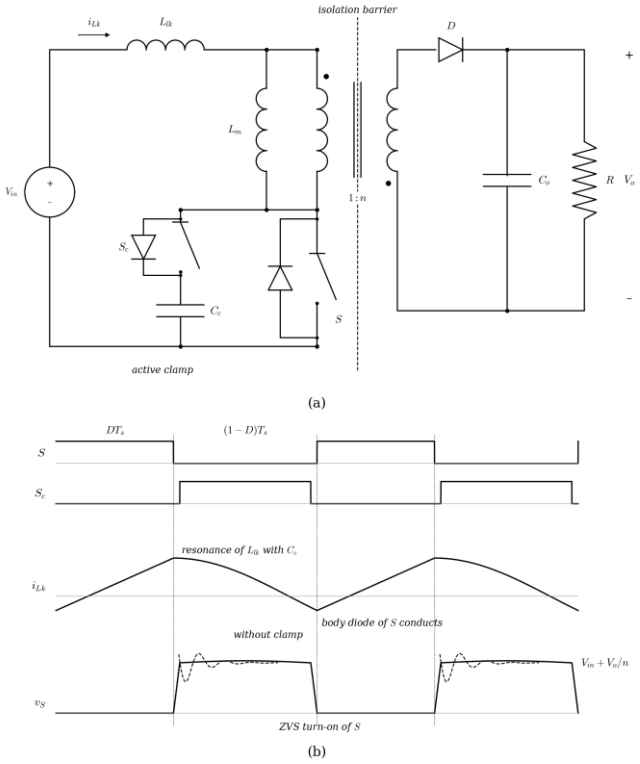



Figure 2-3: Active-clamp flyback converter. (a) [120], Fig. 3: the clamp branch formed by the auxiliary switch $S_c$ and the clamp capacitor $C_c$, operated complementarily to the main switch S, recovers the energy stored in the leakage inductance $L_{lk}$ instead of dissipating it in a resistive snubber; $L_m$ is the magnetizing inductance, and both switches are shown with their body diodes. (b) Qualitative waveforms over two switching periods, [120]: complementary gate signals with dead time; the primary current $i_{Lk}$, which rises linearly while S conducts and, during the off interval, resonates with $C_c$ through zero to a negative value, so that the body diode of S conducts before S is turned on, at zero voltage; and the switch voltage $v_S$, clamped at $V_{in} + V_o/n$, compared with the unclamped turn-off spike and ringing (dashed) [29, 34].

The forward converter is the isolated buck, requiring a core-reset mechanism; push–pull, half-bridge and full-bridge structures progress toward higher power by using the transformer core more fully, at the cost of additional switches and, for the bridge topologies, high-side gate drives [34]. Because the comparative literature places the full-bridge and push–pull structures ahead of the conventional buck and forward converters in tracking capacity (through the leverage of the winding ratio) [28], and because the full-bridge is additionally the natural platform for phase-shift soft switching, it is the isolated topology most often selected for higher-power, string-level grid-connected service [48]. Figure 2- shows the forward converter with a tertiary reset winding.

The microinverter, a grid-tied converter integrated with a single module, is where isolated topologies concentrate most heavily in modern practice, since a single module supplies only tens of volts and a few hundred watts, requiring a large voltage gain at low power that a transformer's turns ratio supplies naturally [10, 40]. The structural difficulty specific to this class is not the DC–DC stage itself but the interface to the grid side: a single-phase inverter demands power that pulsates at twice the line frequency, while the module demands smooth, continuous extraction, so the decoupling between the two - performed by a large capacitor at the module, a regulated intermediate DC link, or, less commonly, by accepting some ripple into the tracking loop - defines much of the microinverter design space [50]. Figure 2- shows a two-stage microinverter with both buffer positions, the power the buffer must absorb, and a commercial unit as installed.

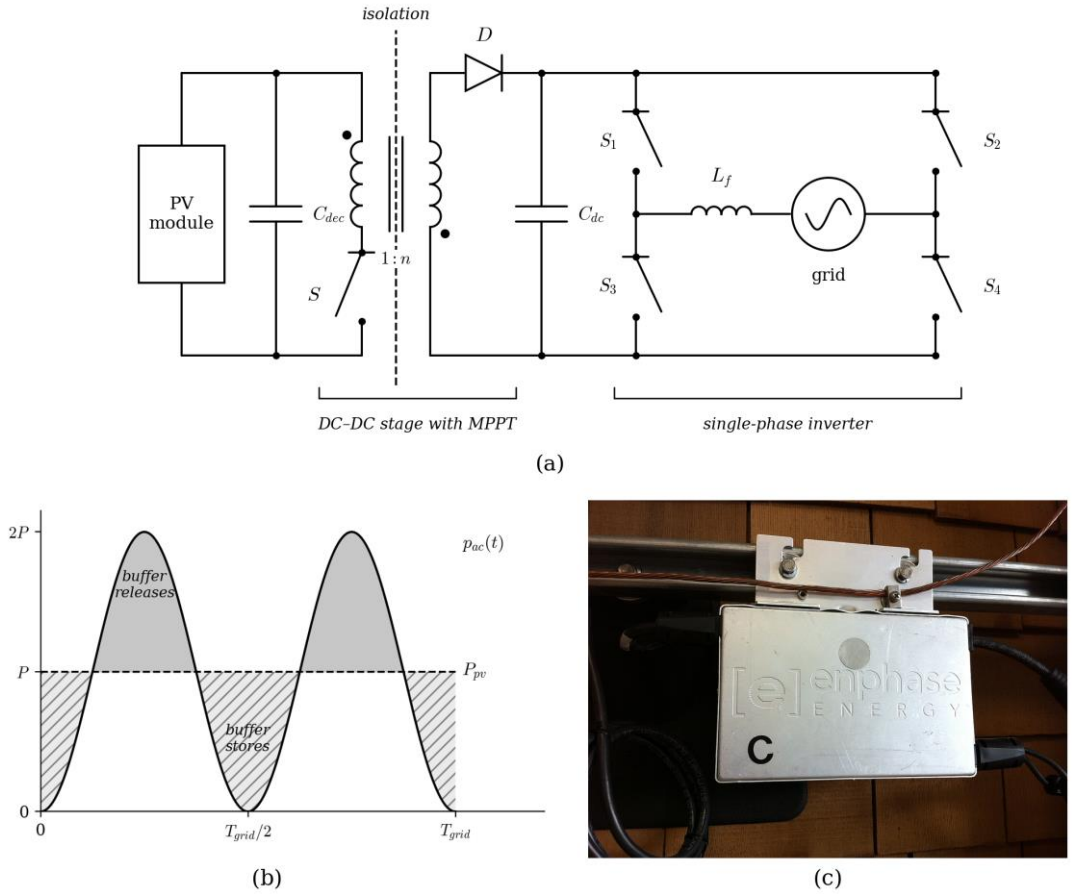



Figure 2-7: (a) A flyback DC–DC stage with MPPT feeds a single-phase full-bridge inverter; the energy buffer can be placed at the module ($C_{dec}$) or at a regulated intermediate DC link ($C_{dc}$). (b) Instantaneous power delivered to a single-phase grid at unity power factor, $p_{ac}(t) = P(1 - \cos 2\omega t)$, which pulsates at twice the line frequency around the constant power $P_{pv}$ extracted from the module; the buffer stores the difference in the hatched intervals and releases it in the shaded ones. (c) A commercial module-level microinverter (Enphase M190) mounted on the racking rail, with the frame grounding conductor attached, before the PV module is placed over it [114]. Panels (a) and (b) [29, 34].

Resonant isolated converters insert a tank circuit between the switch network and the transformer, shaping currents so that the semiconductors commutate near zero voltage or zero current; the resulting efficiency can be high, but because resonant operation depends on the operating point relative to the tank's resonant frequency, these designs are best suited to combination with a pulse-width-modulated front end that absorbs the photovoltaic source's wide input-voltage excursion, leaving the resonant stage to operate closer to its own design point [51]. Figure 2- shows such an arrangement: a PWM boost front end followed by a half-bridge LLC resonant stage.

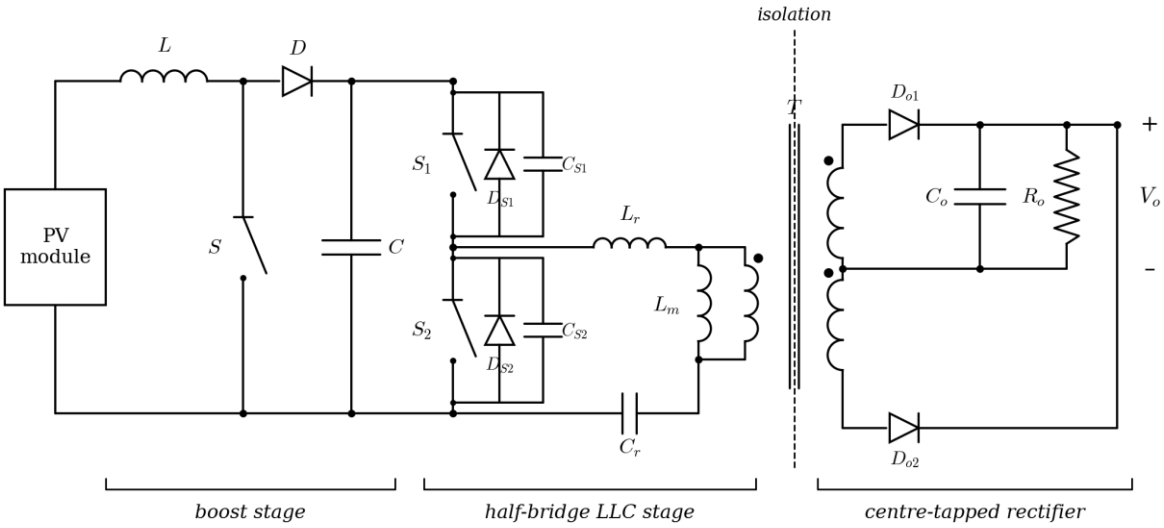



Figure 2-8: Two-stage isolated converter with a resonant output stage, adapted from [121], Fig. 1, with the photovoltaic module in place of the rectified AC input: the boost stage (L, S, D) regulates the intermediate capacitor C, so that the half-bridge ($S_1$, $S_2$) and the LLC tank ($L_r$, $C_r$, $L_m$) can operate close to the resonant frequency $f_r = 1/(2\pi\sqrt{(L_rC_r)})$; during each dead time the resonant current discharges the output capacitance $C_{S1}$ or $C_{S2}$ of the incoming switch, whose body diode $D_{S1}$ or $D_{S2}$ then conducts, so that the switches turn on at zero voltage; the centre-tapped secondary of the transformer T is rectified by $D_{o1}$ and $D_{o2}$.

Whether isolation is needed at all is, however, a requirement decided by codes, grounding scheme and degradation risk rather than by efficiency tables - once the requirement is set, the comparison properly runs within the isolated or the non-isolated class, not across them. Table 2-2 summarises the general trade-off between the two families.

Table 2-2: General comparison of the non-isolated and isolated converter families for photovoltaic service.

| Aspect | Non-isolated family | Isolated family | Reference(s) |
|---|---|---|---|
| Galvanic separation | None | Yes - independent grounds | [48, 49] |
| Gain mechanism | Duty cycle, extended by boosting cells | Duty cycle and transformer turns ratio | [34, 35, 39] |
| Size, cost, component count | Low | Higher - transformer dominates | [34] |
| Characteristic weakness | Limited gain of the basic structures | Leakage inductance; snubber/clamp burden | [29, 34] |
| Typical role | String- and module-level tracking stages | Microinverters; isolation-mandated installations | [10, 40, 48, 49] |

Where storage is integrated into a photovoltaic system, the stand-alone and hybrid configurations of Section 1.6, a further family of bidirectional DC–DC converters allows power to flow into and out of the battery while the array-facing stage continues independently to track its own maximum power point; both isolated and non-isolated bidirectional topologies are classified in a substantial review literature of their own [36, 52]. For the purposes of this thesis, bidirectional converters mark a boundary of scope: the MPPT algorithms surveyed in Chapter 3 act on the unidirectional,

array-facing port, and the additional stress and control burden of the storage-facing port is noted here only so that its exclusion is deliberate rather than accidental.

## 2.4 High Step-Up Non-Isolated Converters

### 2.4.1 Motivation and boosting techniques

Section 2.1.2 established the problem this literature exists to solve: the conventional boost promises unbounded gain and delivers a parasitic-limited ceiling, reached only through extreme duty cycles at which conduction loss, device stress and diode reverse-recovery converge to erode efficiency. Because module-level and short-string architectures require gains from roughly ten upward (Section 1.6), the non-isolated high-gain literature has grown into one of the most prolific branches of power electronics, organised around a small set of voltage-boosting techniques grafted onto the basic converter skeletons of Section 2.2 [34, 35, 39]:

- **Interleaving** places $N$ boost phases in parallel with staggered switching, which cancels input-current ripple partially (completely only at duty cycles that are integer multiples of $1/N$) and divides the power among phases, without changing the ideal gain law; it is, strictly, a current-handling technique rather than a gain-boosting one, valuable to MPPT precisely because it lowers the input ripple that acts as the tracker's noise floor [34, 53].
- **Coupled-inductor** structures wind a second winding on the boost inductor, multiplying the gain by a design-chosen turns ratio without a full transformer, commonly reaching ratios of ten to twenty at moderate duty cycles (0.4–0.6) while holding switch stress well below the output voltage - admitting low-voltage, low-$R_{on}$ devices [38, 39]. The technique's tax is leakage inductance, addressed by active-clamp or regenerative snubber circuits that recycle rather than dissipate the trapped energy [34, 38].
- **Switched-capacitor and switched-inductor cells** boost by topology rather than by duty cycle or magnetics - capacitors charged in parallel and discharged in series (switched-capacitor), or two inductors charged in parallel and discharged in series, giving $M(D) = (1 + D)/(1 - D)$ for the switched-inductor boost [54]. Purely capacitive (charge-pump) realisations pay for their magnetic-free construction with pulsating current and weak regulation, so the photovoltaic literature almost always meets the technique hybridised with an inductor-based front end [34, 54].
- **Voltage-multiplier cells** append diode–capacitor stages to a switching front end; a single stage doubles the base gain law, $M(D) = 2/(1 - D)$, and further stages extend the family

additively, dividing semiconductor stress across the stack at the cost of a growing diode count [56]. To illustrate the structural diversity of this technique, several distinct cell topologies used in Voltage Multiplier Cells (VMCs) are presented below. These modular structures typically incorporate passive components, such as diodes and capacitors, and in some advanced variations, inductors or auxiliary switches [35, 52].

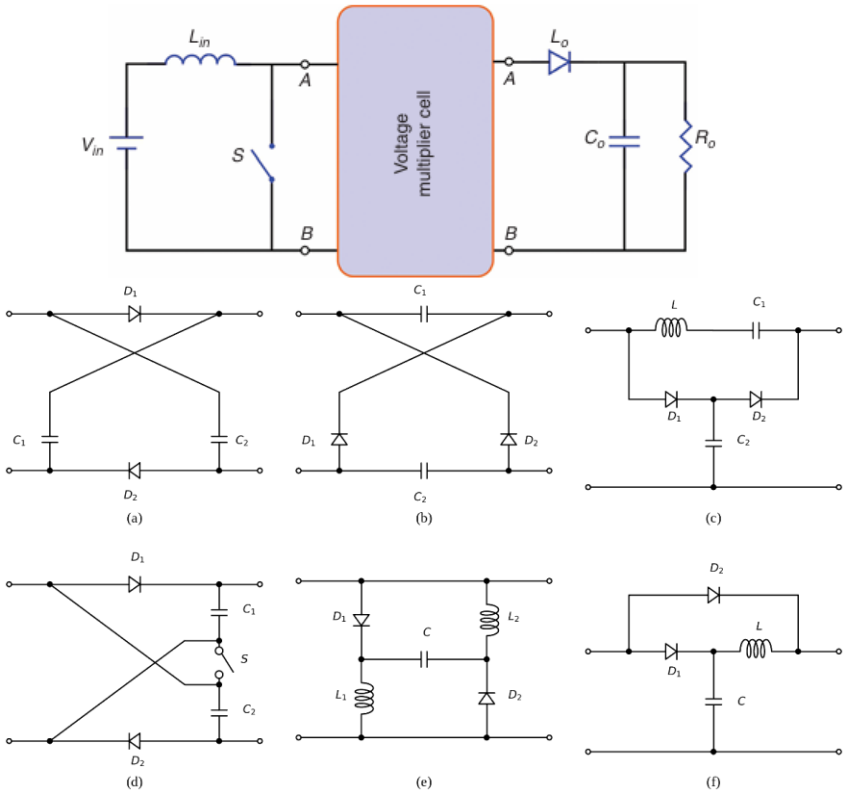



Figure 2-9: Various topology configurations of Voltage Multiplier Cells (VMCs), (a)–(f), built from diodes D and capacitors C, with an inductor L in (c), (e) and (f) and an auxiliary switch S in (d) [35, 52].

Integrating these cells into a switching front end enables the converter to multiply the input voltage efficiently while keeping the voltage stress on individual active semiconductor devices relatively low [35, 52]. Furthermore, these cells are favored for their simple structure and modularity, making them suitable for grid-connected PV systems [35, 52]. However, designers must carefully weigh these benefits against potential practical drawbacks, such as poor voltage regulation, increased overall component count, and a trade-off between the number of multiplier stages and the desired efficiency [35, 52].

- **Cascading** whole converter stages compounds rather than adds: two cascaded boost stages give the quadratic gain law $M(D) = 1/(1-D)^2$, reaching a given ratio at a much lower duty cycle, but efficiencies and losses compound multiplicatively through the chain, and

the second stage must process full power at an already-elevated voltage [34, 55]. Figure 2- shows representative circuits of the interleaving, coupled-inductor, switched-capacitor, switched-inductor and cascading techniques.

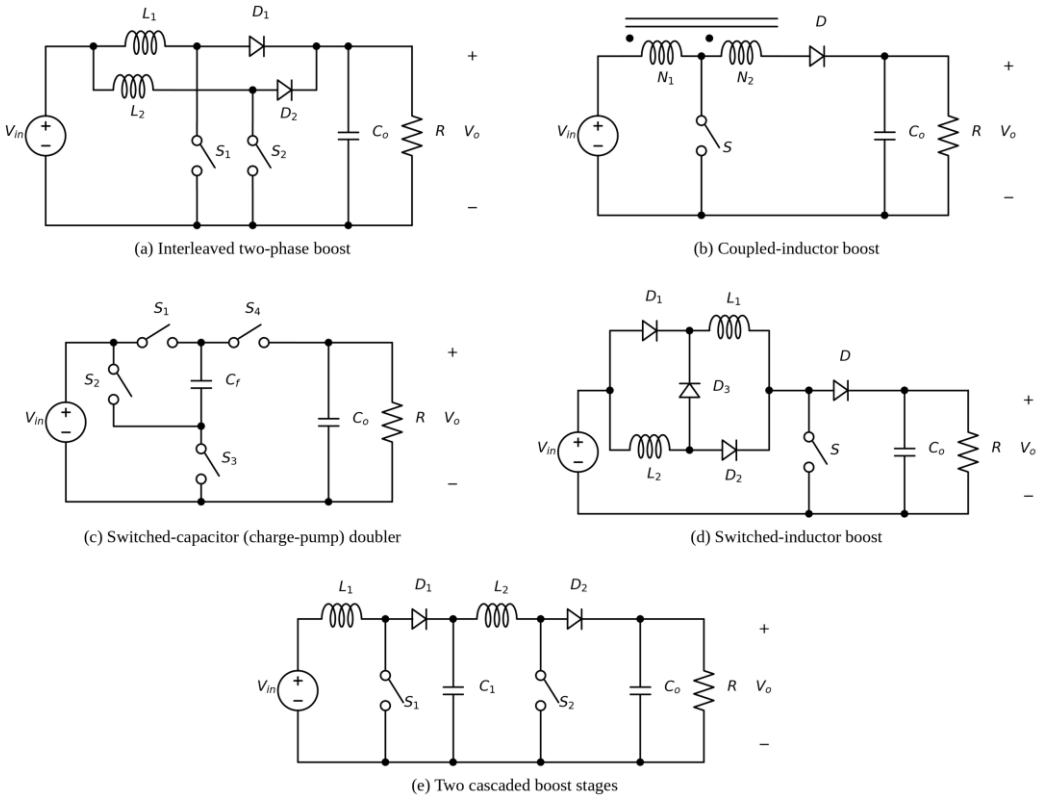



Figure 2-10: Representative circuits of five high step-up techniques, drawn by the author: (a) interleaved two-phase boost, whose ideal gain remains $M = 1/(1 - D)$; (b) coupled-inductor boost, in which the second winding $N_2$ raises the gain according to the turns ratio $N_2/N_1$; (c) switched-capacitor (charge-pump) doubler, in which the flying capacitor $C_f$ is charged in parallel with the source through $S_1$ and $S_3$ and discharged in series with it through $S_2$ and $S_4$, ideally doubling the input voltage at a fixed ratio; (d) switched-inductor boost, with $L_1$ and $L_2$ charged in parallel and discharged in series, $M = (1 + D)/(1 - D)$; (e) two cascaded boost stages, $M = 1/(1 - D)^2$ [34, 53] (a), [34, 38, 39] (b), [54] (c, d) and [34, 55] (e).

- **Voltage-lift techniques** provide another highly effective method to significantly raise the output voltage of a DC-DC converter [35, 52]. This technique operates by charging a capacitor to a specific voltage sourced by the input, and the output voltage is subsequently lifted in proportion to the voltage level of this charged capacitor [35, 52]. The generalized architecture involves integrating a Voltage Lift (VL) cell into the basic boost converter structure [35, 52].

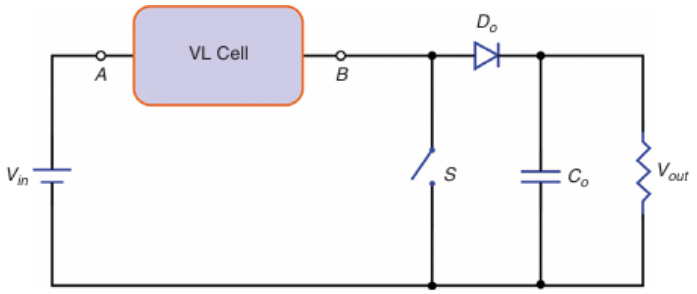



Figure 2-11: Generalized schematic of a DC-DC boost converter equipped with a Voltage Lift (VL) cell, inserted between the switch node and the output diode [35, 52].

By repeating this energy-storing operation with additional capacitors and inductors, more advanced circuits such as elementary-lift, self-lift, and double self-lift cells can be created, yielding an even greater voltage gain [35, 52].

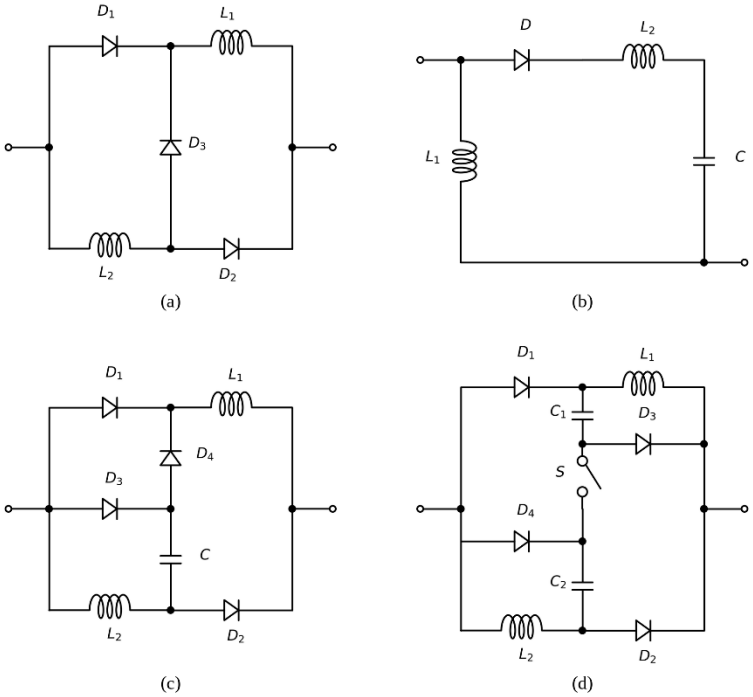



Figure 2-12: Variations in VL cell topology: (a) basic cell, (b) elementary-lift cell, (c) self-lift cell, and (d) double self-lift cell [35, 52].

The overall performance of the VL technique heavily relies on these energy-storage elements [35, 52]. Compared to other advanced step-up methods, the VL technique is favored for its simpler structure, higher power density, higher efficiency, and noticeably smaller output-voltage ripple [35, 52]. These attributes make it exceptionally well-suited for solar energy harvesting systems across a wide power range [35, 52].

Figure 2- compares the ideal gain laws of these routes. At a representative target of tenfold gain, the conventional boost demands $D = 0.90$ (deep in the parasitic collapse region of equation (2.4));

the switched-inductor boost reaches the same gain at $D = 0.82$; a boost with one multiplier stage at $D = 0.80$; and the quadratic cascade at $D = 0.68$ - the practical case for the high-gain literature in a single picture.

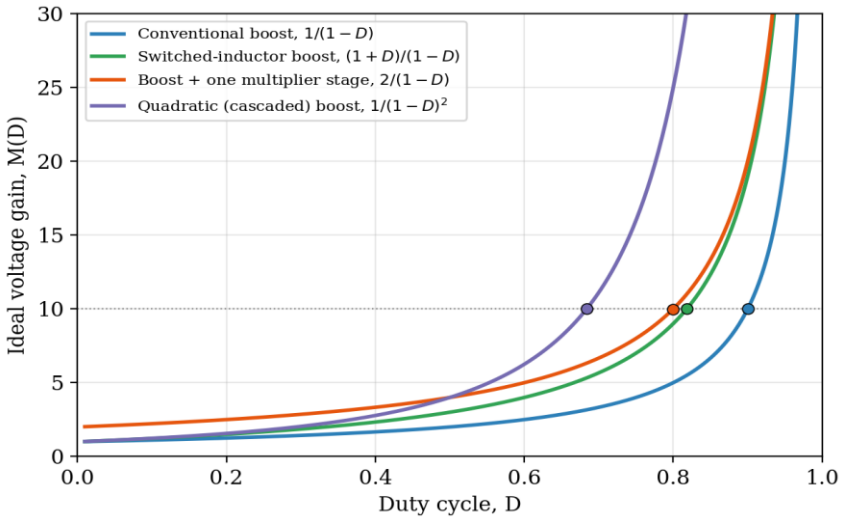



Figure 2-13: Ideal continuous-conduction-mode voltage-gain laws of the principal non-isolated boosting routes: conventional boost (eq. 2.2), switched-inductor boost, boost with one voltage-multiplier stage, and quadratic (cascaded) boost. Markers indicate the duty cycle each route requires for a tenfold gain. Computed by the gain laws of Section 2.4 [34, 35, 39].

### 2.4.2 Combined structures and the photovoltaic reading

The modern high-gain literature is dominated by structures that combine several of the above techniques at once - for example, a coupled inductor whose leakage energy is recycled through a switched-capacitor network, simultaneously achieving high gain at moderate duty and switch stress well below the output voltage [56, 57]. Judged purely as gain-producing machinery, the available techniques are largely interchangeable routes to a required ratio; judged at the array terminals, they differ sharply. Structures that retain a genuine input inductor (interleaved, coupled-inductor, most switched-inductor and multiplier derivatives) preserve the continuous, array-friendly input current that Chapter 1 identified as important for tracking precision, while front ends that place switched-capacitor action directly at the input inherit the pulsating-input weakness of the buck-derived class [34, 44, 54]. This is why the comparative reviews consistently single out coupled-inductor and multiplier-based structures as the preferred high-gain families for photovoltaic service: they combine sub-output-voltage semiconductor stress with a smooth input draw [38, 39].

No single high-gain converter is universally best, however, and the comparative evidence is explicit about why: one survey finds coupled-inductor structures superior at low-to-medium power but fading beyond roughly the kilowatt class as magnetic losses grow [33]; another finds no

consistent winner once component count, stress and efficiency are weighed together across the class [34, 39, 58]. What the comparative literature converges on instead is a set of acceptance conditions rather than a single winner: a high-gain converter should reach its target ratio without an extreme duty cycle or an extreme transformer turns ratio; it should recycle rather than dissipate leakage energy; and it should hold semiconductor stress low enough for low-$R_{on}$ devices and reverse-recovery-free diodes [59]. To these general conditions, the photovoltaic reading adds two further requirements developed in Section 2.5: a continuous, smooth input current, and - because the converter is also an actuator - a duty-to-output relation that is well-behaved from the algorithm's point of view. Table 2-3 collects the boosting techniques of this section against these criteria.

Table 2-3: The principal non-isolated voltage-boosting techniques and what each costs.

| Technique | Effect on ideal gain | Input current at the array | Principal cost | Reference(s) |
|---|---|---|---|---|
| Interleaving | None - each phase obeys the base gain law | Improved: partial ripple cancellation and current sharing | *N*-fold duplication of switch, diode and inductor | [34, 53] |
| Coupled inductor | Scales with the turns ratio | Preserved - the input winding remains an inductor | Leakage inductance, hence voltage spikes and a clamp requirement | [34, 38, 39] |
| Switched capacitor | Multiplies in discrete steps set by cell count | Degraded if placed at the input (pulsed charging currents) | Weak continuous regulation; poor as a stand-alone PV front end | [34, 54] |
| Switched inductor | $M(D) = \frac{(1+D)}{(1-D)}$ | Preserved | Added diodes with their forward drops; higher converter order | [54] |
| Voltage multiplier | Adds a rectified contribution per stage | Preserved when the front end is boost-derived | Growing diode count; component-rating bookkeeping | [35, 52, 56] |
| Cascading | Compounds: $M(D) = \frac{1}{(1-D)^2}$ for two stages | Preserved at the first stage | Duplicated power stage; losses multiply through the chain | [34, 55] |

One structural result deserves separate mention because it is the cheapest apparent route to high gain and also the most frequently misjudged. Cascading $N$ stages compounds both the gain and the losses, $M_{tot} = \prod M_i$ and $\eta_{tot} = \prod \eta_i$, so that two stages of 96% efficiency yield only 92% overall, and the second stage must additionally process the full system power at an already-elevated voltage, requiring higher-voltage devices with larger on-resistance. The quadratic gain of Figure 2- is therefore bought at a compounding efficiency price, which is why the cascaded route, despite using only well-understood parts, is rarely the one the comparative literature recommends for photovoltaic service [3, 58].

A recent single-switch example of a combined structure is the high-gain converter adopted by Akter et al. [102] as the interface of a metaheuristic MPPT (Figure 3-21): two inductors give a quadratic-boost characteristic and a diode–capacitor voltage-doubler stage at the output raises it further, so that the ideal CCM gain is reported as $M(D) = 2/(1 - D)^2$ [102]. The authors select this topology because it draws a continuous input current with low ripple, which they identify as helpful for MPP tracking [102]. Example 2.4 compares its duty-cycle requirement with the routes of Figure 2-15.

**Example 2.4 - Duty cycle for a tenfold gain with the high-gain converter of [102]**

**Given data**

Required gain $M = 10$; ideal gain law $M(D) = 2/(1 - D)^2$ (equation (8) of [102])

**Formula**

$D = 1 - \sqrt{(2/M)}$

**Calculation**

$D = 1 - \sqrt{(2/10)} = 1 - 0.447 = 0.553$

**Result**

| Route | Duty cycle for M = 10 |
|---|---|
| High-gain converter of [102] | ≈ 0.55 |
| Conventional boost | 0.90 |
| Switched-inductor boost | 0.82 |
| One voltage-multiplier stage | 0.80 |
| Quadratic cascade | 0.68 |

Values for the other routes from Figure 2-.

**Interpretation:** the lower duty cycle keeps the converter away from the parasitic collapse of equation (2.4) and from the bandwidth reduction caused by the right-half-plane zero of equation (2.10), at the price of five diodes and four capacitors in addition to the two inductors and the switch (Figure 3-21) - the component-count trade-off of Section 2.4.3. A caveat applies: the derivation printed in [102] arrives at $V_o/V_{in} = 1/(1 - D)^2$ before the factor 2 attributed to the voltage doubler appears in its equation (8); with the quadratic law alone the required duty cycle would be 0.68, the same as for the quadratic cascade.

**Source:** [102]

### 2.4.3 Cost and Reliability Economics

The stress-to-cost chain introduced in Section 2.1.2 has a further consequence worth making explicit before the chapter turns to formal selection criteria: component stress is not merely a design constraint but the dominant proxy through which the academic literature reasons about cost, since detailed component pricing is rarely reported directly in comparative studies. A higher blocking-voltage requirement forces adoption of a higher voltage-class semiconductor, whose larger on-resistance raises conduction loss and whose larger die size raises unit cost; the diode count of a voltage-multiplier or switched-capacitor structure adds a further, linear cost and conduction-loss term with each additional stage [59]. Beyond the semiconductors, magnetics (count, size, and the custom design that coupled and multi-winding structures demand) and gate-

drive complexity (particularly the high-side drivers required by bridge topologies) complete the component bill [34, 40].

Reliability is a related but distinct dimension. Every additional switch, driver and auxiliary supply is, in the most literal sense, an additional failure mode, so hardware complexity carries a reliability cost that a purely performance-oriented comparison tends to underprice: the mean time between failures of a converter falls, other things equal, as component count rises [34]. This consideration is particularly relevant to the module-integrated and high-gain architectures of Section 2.4, whose additional cells, windings and clamp networks buy gain and reduced stress at the cost of a more complex, and in principle less reliable, power stage than the classical six converters of Section 2.2 - a trade-off the selection criteria of Section 2.5 make explicit rather than resolve into a single recommendation.

## 2.5 Converter Selection Criteria

Selecting a converter for photovoltaic service requires two distinct sets of criteria, and this thesis argues - following the review literature's own increasingly explicit recognition of the point - that both must be weighed together rather than separately.

### 2.5.1 Power-processing criteria

The first set concerns the converter purely as a power-processing component: efficiency (conduction, switching and magnetic losses, traded against gain through the parasitic collapse of equation (2.4) and against ripple through switching frequency); voltage gain (the realisable ratio with duty-cycle margin, not the ideal law, paid for in device stress); ripple (measured separately at the array terminals and at the load, a structural property of the topology's port continuity, refined parametrically through inductance, capacitance and frequency); cost (proxied by semiconductor voltage class, device count, magnetics and gate-drive complexity); and complexity (component, switching, control and modelling complexity, the last of these - the effort of obtaining a usable dynamic model of the converter - being the dimension the high-gain literature most conspicuously under-reports) [38, 39, 58, 59]. Each criterion carries a reporting hazard: figures are frequently quoted at a single nominal operating point, whereas a photovoltaic source sweeps its voltage and power continuously, so an honest comparison requires efficiency and ripple to be reported across the operating window rather than at its optimum [60].

### 2.5.2 The converter as MPPT actuator: seven additional criteria

The second set of criteria is largely absent from the power-electronics selection literature, because it prices the converter not as a power processor but as the actuator of a control loop, and it is only visible once the two literatures are read together - the synthesis this thesis undertakes. Seven such criteria can be assembled from evidence distributed across the converter and tracking literatures, and Table 2-4 collects them; each is developed further, from the algorithm's side, in Chapters 3 and 4.

Table 2-4: Converter selection criteria relevant to MPPT implementation.

| Criterion | Converter property that sets it | Consequence for the tracking loop | Reference(s) |
|---|---|---|---|
| Reachable operating range | Family gain law and duty margin across the irradiance/temperature window | The MPP may lie outside the actuator's reach if the family (e.g. boost, buck) has a bounded reflected resistance | [18, 28, 31] |
| Shape of the actuation law | Nonlinearity and steepness of $M(D)$; the parasitic collapse region of eq. (2.4) | A fixed perturbation step produces very different, even wrong-signed, responses at different duty cycles | [31, 38, 39] |
| Constancy of the actuation law | CCM/DCM boundary across the operating window (eq. 2.5) | The duty-to-voltage relation the algorithm assumes may silently change beneath it | [32, 42] |
| Input-ripple noise floor | Port continuity fixed by topology; then $L$, $C$, $f_s$ and interleaving | Bounds the smallest power difference the algorithm can trust, and hence its minimum useful step | [6, 44-46] |
| Dynamics and settling time | Converter order, damping and bandwidth (structurally topology-dependent) | Sets a floor under the tracking sampling interval; sampling before settling risks instability | [18, 46, 61] |
| Control-structure compatibility | Which port is regulated; presence of a right-half-plane zero in boost-derived stages | Determines which control structures (direct duty-cycle vs. reference-based) are viable | [25, 62] |
| Joint operating-window metric | Conversion efficiency curve across the operating window, combined with tracking efficiency | The harvested energy is the *product* of conversion and tracking efficiency, not either alone | [60] |

Two of these criteria deserve a brief technical note because they recur throughout Chapters 3 and 4. First, dynamics and settling time: a perturbation-based tracker must wait for the converter's transient to settle before its next power measurement is meaningful, so the tracking sampling interval $T_p$ must satisfy a bound of the form

$$T_p \geq \frac{-\ln(\varepsilon)}{\xi \cdot \omega_n} \tag{2.9}$$

where $\xi$ and $\omega n$ are the damping ratio and natural frequency of the array-plus-converter interface and $\varepsilon$ the settling tolerance [46, 61]. Because $\xi$ and $\omega_n$ differ by an order of magnitude between converters built from the same components (a boost stage typically presents a single, well-damped

time-varying parameter, while a fourth-order Ćuk or SEPIC stage presents a more elaborate, less forgiving dynamic), the same algorithm may legitimately be tuned to iterate far more slowly on one converter than on another - a fact the algorithm-only comparative literature routinely elides by testing every method on a single default converter [18, 61]. Second, boost-derived converters in CCM exhibit a right-half-plane zero in their control-to-output transfer function, at

$$\omega_z = \frac{R_L \cdot (1 - D)^2}{L} \quad (2.10)$$

a frequency that falls with the *square* of $(1 - D)$, so that the achievable control bandwidth collapses precisely in the high-gain regime ($D$ close to unity) that Section 2.4 showed the module-level architectures demand. This non-minimum-phase behaviour - physically, the energy-transfer delay of inductive storage, whereby stepping up the duty cycle initially causes the output voltage to move the wrong way before rising toward its new value - bounds the achievable closed-loop bandwidth of any output-regulated inner loop and is one reason input-side (array-voltage) regulation is often preferred in photovoltaic chargers over output-side regulation [25, 62].

## 2.6 Interaction Between the Converter and the MPPT Controller

The criteria of Section 2.5.2 are the bridge to the remainder of this thesis. They establish, on purely converter-side evidence, that the choice of power stage is not a preliminary decision that can be made independently of the tracking algorithm that will drive it: the converter fixes the plant's gain law, its constancy, its noise floor and its dynamics, and every one of these quantities reappears in Chapter 3 as an assumption that some MPPT algorithm makes, a parameter it must be tuned to, or a failure mode it inherits. Direct experimental confirmation exists in the comparative literature: studies that vary the converter deliberately while holding the tracking algorithm fixed report that settling time and average steady-state efficiency differ for every converter–algorithm pairing, with no single combination best on all criteria [47], and that the ranking of algorithms can invert when the underlying converter is changed [63]. This evidence - that a reported tracking figure is, in the studies that have actually tested for it, a property of the algorithm–converter pair rather than of the algorithm alone - is the empirical anchor for the comparative discussion of Chapter 4, and it is the reason this thesis treats the converter survey of the present chapter as inseparable from the MPPT survey that follows.

Table 2-5 closes the chapter with a converter-level view, grouped by family, that draws together the power-processing criteria of Section 2.5.1 and the actuator-facing criteria of Section 2.5.2 and

adds the quantitative indicators available in the surveyed sources. Because converter-level rankings proved conditional on the specific requirement - conversion ratio, isolation class, power level - and because the reported efficiencies were obtained under different conditions, each figure is given with its source and test conditions and the comparison is organised by family and by the application for which the reviewed literature recommends each converter, rather than as a single numerical ranking. The one comparison made on a common basis is the duty cycle each converter needs for the 33 V to 380 V example of Section 1.6 (M = 11.5): the conventional boost and the buck–boost family require D = 0.91–0.92, a gain that a boost with a parasitic ratio of 1 % cannot reach at all, whereas the switched-inductor boost, a single multiplier stage, two cascaded boosts and the high-gain converter of Akter et al. reach it at D = 0.84, 0.83, 0.71 and 0.58 respectively.

Table 2-5: Converter-level summary of the topologies surveyed in this chapter, grouped by family, with the quantitative indicators reported in the sources

| Converter | Ideal gain M(D) | D for M = 11.5 | S–D–L–C–T | Input current | Reported efficiency (%) | Actuator dynamics; response, oscillation (P&O / INC) | Ref. |
|---|---|---|---|---|---|---|---|
| ***Basic non-isolated (including soft-switched variants)*** | | | | | | | |
| Buck | D | unreachable (M ≤ 1) | 1–1–1–1–0 | Pulsating | 98 / 96[a] | Heaviest control burden; fast / fast, 0.2 / 0.2 %[a] | [18, 28] [101] |
| Boost | 1/(1 − D) | 0.913; ceiling ≈ 5 if $r_L/R$ = 1 % | 1–1–1–1–0 | Continuous | 98 / 97[a] | Best-behaved, well damped; medium / fast, 0.3 / 0.4 %[a] | [18, 27, 38, 39] [101] |
| Buck–boost | D/(1 − D), inverted | 0.920 | 1–1–1–1–0 | Pulsating | 92 / 90[a] | Medium / medium, 1.2 / 0.9 %[a] | [28, 33] [101] |
| Ćuk | D/(1 − D), inverted | 0.920 | 1–1–2–2–0 | Continuous | 95 / 94[a] | Fourth order; low / low, 1.8 / 1.6 %[a] | [33, 47] [101] |
| SEPIC (hard / ZVS) | D/(1 − D) | 0.920 | 1–1–2–2–0 / 1–2–3–3–0 | Continuous | 97 / 90[a]; 83.4 / 88.6[b]; ZVS 90.6 / 89.0[b] | Fourth order; fast / medium, 2.1 / 0.7 %[a] | [25] [100, 101] |
| Zeta (hard / ZVS) | D/(1 − D) | 0.920 | 1–1–2–2–0 / 1–2–3–3–0 | Pulsating | 87.7 / 94.0[b]; ZVS 89.7 / 98.1[b]; INC exp. 93.5 → 97.8[c] | Fourth order; n/r | [33, 47] [100] |
| ***Isolated*** | | | | | | | |
| Flyback (RCD / active clamp) | nD/(1 − D) | 0.5 with n = 11.5 | 1–2–0–2–1 / 2–1–0–2–1 | Pulsating | n/r | Leakage-inductance dynamics unless actively clamped | [29, 34] |
| Forward | nD | 0.5 with n = 23 | 1–3–1–1–1 | Pulsating | n/r | As flyback | [34] |
| Full-bridge (phase-shift) | set by n | set by n | 4–(2–4)–1–1–1 | Pulsating | n/r | As flyback; natural platform for soft switching | [28, 29, 34, 48] |
| LLC resonant, two-stage | boost × tank (set by n near $f_r$) | boost absorbs range; LLC near $f_r$ | 3–5–2–3–1 | Continuous (boost front end) | n/r | Depends on operating point relative to $f_r$ | [51] |
| Microinverter (flyback + full bridge) | as flyback | 0.5 with n = 11.5 | 5–1–1–2–1 | Pulsating, buffered by $C_{dec}$ | n/r | Twice-line-frequency ripple reaches the tracker unless decoupled | [29, 34] |
| ***High step-up non-isolated*** | | | | | | | |
| Interleaved boost (2 phases) | 1/(1 − D) | 0.913 | 2–2–2–1–0 | Continuous, reduced ripple | n/r | Lower input-ripple noise floor for the tracker | [34, 53] |
| Coupled-inductor boost | scales with n | ≈ 0.4–0.6 for ratios 10–20 | 1–1–0–1–1 (+ clamp) | Continuous | n/r | Actuation law steepened by design | [34, 38, 39] |
| Switched capacitor (charge pump) | 2 (fixed) | unreachable with one cell | 4–0–0–2–0 | Pulsating | n/r | Weak continuous regulation | [34, 54] |
| Switched-inductor boost | (1 + D)/(1 − D) | 0.840 | 1–4–2–1–0 | Continuous | n/r | Actuation law steepened by design | [54] |
| Voltage multiplier (one stage) | 2/(1 − D) | 0.826 | boost + 2 D, 1–2 C per stage | Continuous | n/r | Actuation law steepened by design | [35, 52, 56] |
| Voltage lift | cell-dependent | cell-dependent | boost + VL cell | n/r | n/r | n/r | [35, 52] |
| Two cascaded boosts | $1/(1 - D)^2$ | 0.705 | 2–2–2–2–0 | Continuous | e.g. 2 × 96 → 92 (losses compound) | Actuation law compounded | [34, 55] |
| High-gain converter of [102] | $2/(1 - D)^2$ | 0.583 | 1–5–2–4–0 | Continuous, low ripple | n/r (tracking 99 with POA[d]) | Tracking time 0.20 s with POA[d] | [102] |
| Bidirectional family | high gain in both directions | — | — | — | n/r | Mode-symmetric requirements; doubled control burden | [36, 52] |

Table 2-5 (continued): typical photovoltaic role and main limitation of each converter; sources as above.

| Converter | Typical PV role | Main limitation |
|---|---|---|
| ***Basic non-isolated (including soft-switched variants)*** | | |
| Buck | Chargers with bus below array voltage | Step-down only; input filtering needed |
| Boost | Default two-stage grid-connected front end | Parasitic gain collapse at extreme D |
| Buck–boost | Wide-range chargers, stand-alone systems | Inverted output; weakest of its class on ripple |
| Cuk | Wide-range chargers, stand-alone systems | Inverted output; seven components |
| SEPIC (hard / ZVS) | Array voltage on either side of the bus | Higher output ripple than Zeta; ZVS gain only 0.41 points with INC |
| Zeta (hard / ZVS) | Demanding loads; ZVS for highest efficiency in low-power PV | Pulsating input; ZVS adds $L_r$, $C_r$, D and works near one operating point |
| ***Isolated*** | | |
| Flyback (RCD / active clamp) | Low-power, module-level stages; microinverters | Chopped input current; leakage spikes need a clamp |
| Forward | Isolated buck-type stages | Core-reset mechanism required |
| Full-bridge (phase-shift) | Higher-power, string-level grid-connected service | Four switches; high-side gate drives |
| LLC resonant, two-stage | Efficient isolated stage behind a PWM front end | Resonance tied to the design point; two power stages |
| Microinverter (flyback + full bridge) | Module-integrated grid-tied conversion | Power decoupling at $2f_{grid}$ |
| ***High step-up non-isolated*** | | |
| Interleaved boost (2 phases) | High-current front ends | N-fold duplication of S, D and L |
| Coupled-inductor boost | Module-level, large-ratio architectures | Leakage inductance; clamp required |
| Switched capacitor (charge pump) | Only hybridised with an inductive front end | Pulsed charging currents |
| Switched-inductor boost | Module-level, large-ratio architectures | Added diode drops; higher order |
| Voltage multiplier (one stage) | Grid-connected PV, modular gain | Growing diode count |
| Voltage lift | Solar harvesting over a wide power range | Performance tied to the energy-storage elements |
| Two cascaded boosts | Large ratios at moderate D | Losses multiply; second stage at full power and high voltage |
| High-gain converter of [102] | Stand-alone ≈ 2 kW array with metaheuristic MPPT | Printed gain derivation inconsistent (Worked Example 2.4) |
| Bidirectional family | Storage coupling in stand-alone and hybrid systems | Control complexity |

S–D–L–C–T: numbers of switches, diodes, inductors, capacitors and transformers or coupled inductors in the circuits of this chapter, input capacitor excluded. D for M = 11.5: ideal duty cycle for the 33 V module to 380 V DC-link example of Section 1.6, computed from the gain law in the second column; for isolated converters, the turns ratio that achieves it at D = 0.5 is given. n/r: not reported in the surveyed sources. Efficiencies, responses and oscillations are quoted with their conditions and are not comparable across studies: [a] simulation, 85 W module, irradiance and temperature steps, P&O / INC [101]; [b] simulation, 10 W panel, 1000 W/m$^2$, 25 °C, $f_s$ = 5 kHz, P&O / INC [100]; [c] experiment, conventional → ZVS [100]; [d] MPPT tracking performance with the Pelican optimisation algorithm, not a converter efficiency [102].

# 3 CHAPTER 3 - MAXIMUM POWER POINT TRACKING: STATE OF THE ART

Chapter 1 introduced the maximum power point (MPP) as a device property - the peak of the power–voltage characteristic - and Chapter 2 established the DC–DC converter as the actuator through which any control action reaches the array. This chapter re-reads the MPP as a control objective and surveys, critically, the algorithms that have been proposed to track it. Section 3.1 sets out why the problem is genuinely one of real-time optimisation rather than simple regulation, and fixes the performance criteria used throughout the chapter to judge competing methods. Section 3.2 surveys the classical algorithms that remain the deployed mainstream. Section 3.3 surveys the advanced and intelligent techniques developed to overcome the classical methods' limitations under nonlinear and multi-peaked characteristics. Section 3.4 - reflecting the emphasis of this thesis - surveys the most recent techniques reported in the literature: hybrid two-stage schemes, machine-learning and reinforcement-learning approaches, model predictive control and sliding-mode control, followed by a case study of a recent metaheuristic algorithm (the Pelican Optimisation Algorithm) paired with a high-gain converter. Section 3.5 closes the chapter with a condition-by-condition synthesis of what the assembled evidence establishes.

## 3.1 The Maximum Power Point as a Tracking Problem

### 3.1.1 MPPT as real-time optimisation without a reference

Maximum Power Point Tracking is not a regulation problem in the conventional sense, because no reference signal for the optimal voltage or current is available to the controller. The MPP coordinates depend on irradiance and temperature that a standard implementation does not measure directly, and on device parameters that drift with age; all that is available are the terminal measurements of array voltage and current, from which the location of the (possibly moving, possibly multiple) peak must be inferred [17, 24, 64]. Figure 3-1 shows the resulting control loop: the tracking algorithm senses the array's terminal voltage and current and issues a duty-cycle command that the converter's pulse-width modulator (PWM) realises.

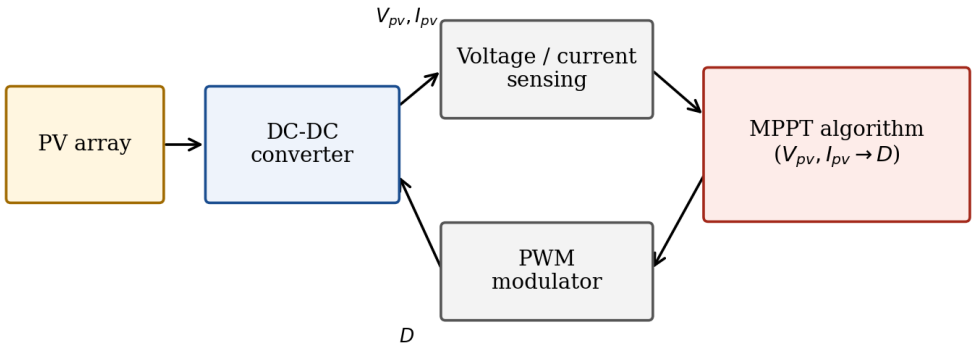



Figure 3-1: Generic Maximum Power Point Tracking control loop: the algorithm senses the array terminal voltage and current and issues a duty-cycle command $D$ to the converter's PWM stage [17, 24, 64].

MPPT is therefore real-time extremum-seeking optimisation, conducted through an actuator - the converter of Chapter 2 - that has its own dynamics, its own noise floor, and, as Section 2.1.2 showed, its own operating-mode boundaries. Every algorithm family surveyed in this chapter is a different answer to the same problem: how to find, hold, and continuously re-find an extremum using only local terminal measurements.

The importance of solving this problem well is quantifiable at every scale. At the scale of a single module, Chapter 1 priced the cost of not tracking at all: a directly connected resistive load can forfeit on the order of 37% of the available power with nothing wrong with the module. At the scale of the installed fleet - with solar PV accounting for more than 2,000 GW of installed capacity worldwide (Chapter 1) - a single percentage point of harvest translates into terawatt-hours, which is why MPPT is standard equipment in essentially every architecture surveyed in Section 1.6 [1, 28, 64].

### 3.1.2 Performance criteria

The tracking literature judges competing algorithms against four largely independent criteria, together with sensitivity to environmental change and dependence on system parameters [40, 64]:

- **Tracking speed** - the time required to reach the MPP, at start-up and after every environmental disturbance;
- **Steady-state oscillation** - the residual power loss once the MPP has (approximately) been reached, unavoidable in perturbation-based methods because the algorithm can only know it is at the peak by stepping off it;
- **Stability** - bounded, non-divergent behaviour of the search itself, which can fail through sampling faster than the plant settles, through drift under fast-changing irradiance (in which the algorithm mistakes an environmental power change for the effect of its own last step),

or, under partial shading, through convergence on a local rather than the global maximum [24, 40, 46, 61];

- **Implementation cost** - sensing requirements, computational burden, and the tuning/training effort needed to commission the method [64-66].

No conventional tracking technique achieves all four simultaneously, reliable global convergence, negligible oscillation, fast response, robustness to system parameters, and low cost, and the algorithm families surveyed below are best read as different resolutions of this same four-way trade rather than as competitors for a single ranking [40, 64]. A single summary metric, the tracking efficiency, integrates all four over a stated operating profile:

$$\eta_{\mathrm{MPPT}} = \frac{\int P(t)\,\mathrm{d}t}{\int P_{av}(t)\,\mathrm{d}t} \tag{3.1}$$

where $P(t)$ is the power actually drawn and $P_{av}(t)$ the maximum available at each instant [46, 67]. This metric is only as honest as the profile over which it is computed and the converter through which it was measured - a point developed further in Section 3.5 and in the comparative discussion of Chapter 4.

Critically, and as Chapter 2 already anticipated, several of these criteria are set jointly by the algorithm and the converter. The perturbation (sampling) interval $T_p$ must exceed the settling time of the array-plus-converter transient (equation 2.9), or the algorithm samples a transient rather than a settled value and may be driven to perturb in the wrong direction [46, 61]; the smallest useful perturbation step is bounded below by the converter's own switching-ripple noise floor [44, 50]; and, as Section 2.1.2 showed, the converter's conduction-mode boundary can silently replace the voltage–duty relation on which a perturbation-based algorithm implicitly relies. A reported tracking-speed or oscillation figure is therefore, strictly, a property of the algorithm–converter pair, not of the algorithm in isolation - a conclusion returned to explicitly in Chapter 4.

### 3.1.3 Mathematical Background

Three formal objects recur throughout the remainder of this chapter and are fixed here once rather than re-derived family by family. The first is the sampled-data gradient estimate on which the classical kernels of Section 3.2 rest: with samples taken at interval $T_p$, defining $\Delta P(k) = P(k) - P(k-1)$ and $\Delta V(k)$, $\Delta I(k)$ likewise, the perturb-and-observe and incremental-conductance decision rules (Sections 3.2.1–3.2.2) are, formally, one-bit and two-sample finite-

difference estimates of the power gradient and the incremental conductance respectively. Reading them this way makes the noise-floor and timing arguments of Section 3.1.2 exact rather than merely descriptive: a difference computed inside the converter's switching-ripple band carries no usable information, and one computed before the converter has settled carries misleading information.

The second is the population-search formalism used by the metaheuristic family of Section 3.3.3: an encoding of candidate solutions (in this application, duty cycles or voltage references - the actuator's own coordinates), a fitness function (the measured array power, so every evaluation is a physical experiment conducted through the converter), an update rule (which differs from one metaheuristic to the next and is what the family names in Section 3.3.3 advertise), and a termination/restart policy (since a converged population must detect an environmental change and search again). Of these four parts, three are shared by every population-based method and coupled to the converter; only the update rule is specific to the named algorithm - an observation that explains why the metaheuristic family's members, despite their different biological or physical metaphors, share so many of the same structural costs (Section 3.3.3).

The third is the profile-integrated efficiency metric of equation (3.1), which is the common yardstick against which every family surveyed in this chapter is ultimately compared in Section 3.5 and Chapter 4. Every criterion of Section 3.1.2 is visible inside it: transient shortfalls enter through the numerator during the tracking phase, steady-state oscillation appears as the standing gap once converged, and instability appears as the additional excursions in between. Because the metric's honesty is exactly as good as the irradiance profile and the converter over which it is evaluated, a tracking-efficiency figure quoted without either is, strictly, incomplete.

## 3.2 Conventional MPPT Algorithms

The conventional methods solve the tracking problem with the least machinery: local terminal measurements, simple decision logic, and no explicit model of the array beyond the shape facts of Chapter 1. They remain the deployed mainstream and the baseline against which essentially every algorithm proposed in the literature is benchmarked [64-66].

### 3.2.1 Perturb and Observe (P&O)

Perturb and Observe is conceptually the simplest MPPT algorithm, and it belongs to the broader family the literature calls hill-climbing methods - techniques that move the operating point in the direction that locally increases power, of which P&O and Incremental Conductance (Section 3.2.2)

are the two most widely deployed representatives. At each sampling instant $k$, the controller compares the measured power $P(k)$ with the previous sample $P(k-1)$; if the power increased, the last perturbation is repeated in the same direction, and if it decreased, the direction is reversed. Formally, with $\Delta D(k)$ the duty-cycle increment applied at step $k$ and $\Delta D$ the (possibly fixed) perturbation amplitude,

$$D(k+1) = D(k) + \Delta D \cdot \text{sign}[\Delta P(k) \cdot \Delta D(k)] \quad (3.2)$$

Figure 3-2 gives the corresponding flowchart. The method requires only a voltage and a current sensor and a handful of arithmetic operations per iteration, which is why it remains the field's reference algorithm [64].

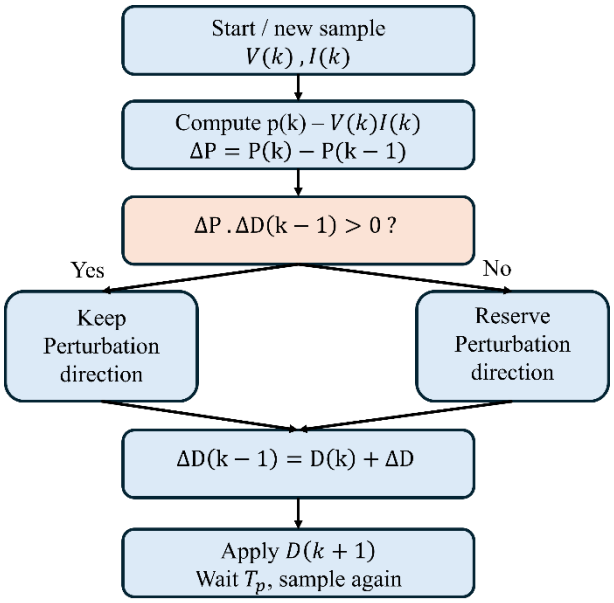



Figure 3-2: Flowchart of the perturb-and-observe (P&O) algorithm in its compact sign form, equation (3.2) [23, 24, 61].

P&O's limitations are equally well documented. Because tracking proceeds by perturbation, the converged operating point oscillates continuously about the true MPP in a characteristic three-level duty-cycle cycle, and the associated power loss scales with the perturbation amplitude - so reducing the step to limit steady-state loss simultaneously slows the transient response, an explicit and unavoidable design compromise [61]. Under rapidly changing irradiance, the algorithm can misinterpret an environmental power change as the effect of its own last step and perturb in the wrong direction - the drift failure mode - continuing away from the peak until the confusion clears [40, 61]. Under partial shading, P&O has no mechanism for distinguishing a local peak from the global one, since the stopping condition of equation (1.6) is satisfied at every local maximum; the

review literature documents fixed-step P&O converging on, and oscillating indefinitely about, a local maximum under such conditions [23, 24].

**Example 3.1 - Steady-state oscillation loss of P&O for the module of Table 1-3**

**Given data**

- Module of Table 1-3 at STC (single-diode model of equation (1.2)): $V_{mpp}$ = 32.0 V, $P_{mpp}$ = 350 W.
- In steady state P&O visits $V_{mpp} - \Delta V$, $V_{mpp}$ (twice) and $V_{mpp} + \Delta V$ in each three-level cycle.

**Formulas**

Average power: $[P(V_{mpp} - \Delta V) + 2P_{mpp} + P(V_{mpp} + \Delta V)]/4$

Oscillation loss: $1 -$ average power$/P_{mpp}$

Ideal boost stage: $V_{pv} = (1 - D)V_o$ (equation (1.7)) with a stiff output voltage $V_o$, so a step $\Delta D$ moves the array voltage by $\Delta V = V_o \Delta D$

**Calculation (equation (1.2) evaluated numerically)**

| Step ΔV | P at $V_{mpp} - \Delta V$ | P at $V_{mpp} + \Delta V$ | Oscillation loss |
|---|---|---|---|
| 0.5 V | 349.6 W | 349.5 W | 0.12 % |
| 1 V | 347.6 W | 346.4 W | 0.49 % |
| 2 V | 340.7 W | 331.9 W | 2.0 % |

With $V_o$ = 380 V (Section 2.1.2), $\Delta V$ = 1 V corresponds to $\Delta D \approx 0.0026$ and $\Delta V$ = 0.5 V to $\Delta D \approx 0.0013$.

**Result**

- Halving the perturbation from 2 V to 1 V reduces the oscillation loss about four times (2.0 % → 0.49 %): the loss grows roughly with the square of the step.
- The excursion towards higher voltage costs more (5.3 % at +2 V against 2.8 % at −2 V), because the characteristic falls more steeply on the voltage-source side (Section 1.4).

**Interpretation:** these numbers make the speed–oscillation compromise of P&O quantitative. The duty-cycle resolution needed for sub-volt steps (about 1/760 at 380 V) is of the order of a 10-bit PWM resolution (1/1024), so the useful step size is set as much by the converter and its modulator as by the algorithm (Section 3.1.2).

**Source:** computed by equation (1.2) with the parameters of Table 1-3, the same model used for Figures 1-2 to 1-5.

Two directions of refinement have substantially narrowed P&O's classical weaknesses without abandoning its local-search character. Variable-step schemes scale the perturbation amplitude to the estimated distance from the peak - large while the power gradient is steep, shrinking as the peak is approached - buying faster transient response together with reduced steady-state oscillation [46, 64]. The founding optimisation of the method derives the perturbation period and amplitude directly from the converter's transient dynamics, formalising equation (2.9) and concluding that both parameters must be customised to the specific converter employed - an early and rigorous instance of the converter–algorithm co-design theme developed in Chapter 4 [61]. Figure 3-3 shows both forms acting on a boost stage: (a) the fixed-step algorithm of equation (3.2) and (b) the variable-step and self-predictive structure described below.

More recent self-predictive and adaptive-gain variants go further:

- One scheme runs the plain P&O kernel only until the first oscillation signals the peak's neighbourhood, then switches to a predictive stage that uses several consecutive operating

points to place the next duty cycle directly, cutting the effective step sharply and achieving an essentially oscillation-free steady state without sacrificing dynamic response, validated on hardware [41];

- A related design pairs an adaptive-gain transient stage with a steady-state stage that detects convergence and holds the duty cycle exactly, releasing it only when a power change exceeding a noise-referenced threshold signals a genuine environmental event - an explicit, quantitative negotiation between the oscillation criterion and the converter's noise floor [46].
- A drift-free variant restores directional correctness under changing irradiance by admitting the measured change in current, not only in power and voltage, into the perturbation decision [40].

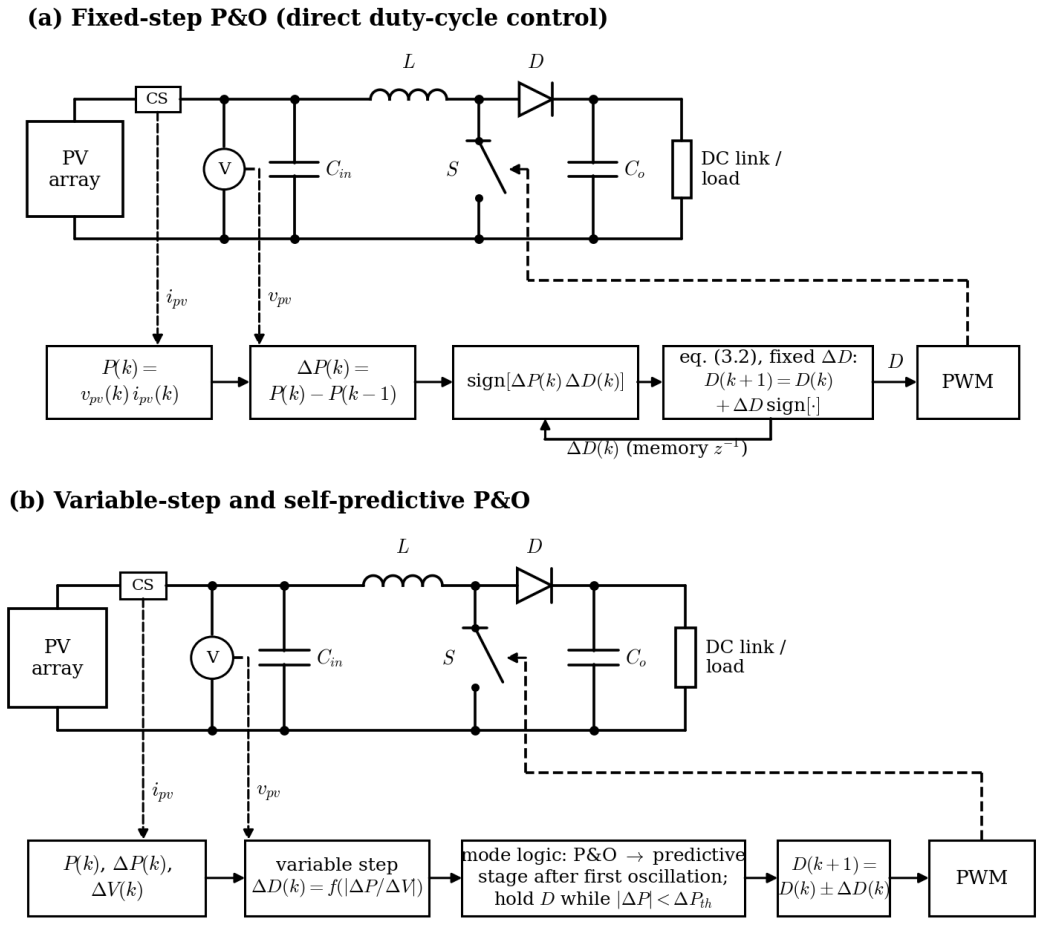



Figure 3-3: Circuit-level schematic of perturb-and-observe tracking on a boost stage, with its control system. (a) Fixed-step P&O in the direct duty-cycle structure: the measured array voltage $v_{pv}$ and current $i_{pv}$ (current sensor CS) give P(k) and ΔP(k), and equation (3.2) updates the duty cycle with a fixed perturbation ΔD, the previous increment ΔD(k) being held in memory ($z^{-1}$). (b) Variable-step and self-predictive P&O: the step is scaled with the power–voltage gradient, and a mode logic switches to a predictive stage after the first oscillation and holds D while |ΔP| stays below a noise-referenced threshold $\Delta P_{th}$, as described in Section 3.2.1 [23, 24, 61] (a) and [40, 41, 46, 64] (b).

### 3.2.2 Incremental Conductance (INC)

Incremental Conductance tests the stationarity condition of equation (1.6) directly, in its equivalent conductance form: the MPP is characterised by

$$\frac{\Delta I}{\Delta V} = -\frac{I}{V} \tag{3.3}$$

so the algorithm compares the incremental conductance $\Delta I/\Delta V$ with the instantaneous conductance $-I/V$ and steps the duty cycle toward higher voltage while the incremental term exceeds the instantaneous one, toward lower voltage in the converse case, and holds - within a small tolerance band - at equality (Figure 3-4). Relative to P&O, INC's principal structural advantage is a defined stopping state: rather than perturbing indefinitely, the algorithm can in principle recognise the MPP and cease perturbing, which the review literature credits with somewhat better discrimination under some patterns of changing irradiance [17, 64]. It is nevertheless best understood as an alternative realisation of the same hill-climbing principle rather than a fundamentally different technique - both kernels are built on the same gradient condition and exhibit broadly similar convergence behaviour, a conclusion reached independently from analysis and from direct experimental comparison [68, 69].

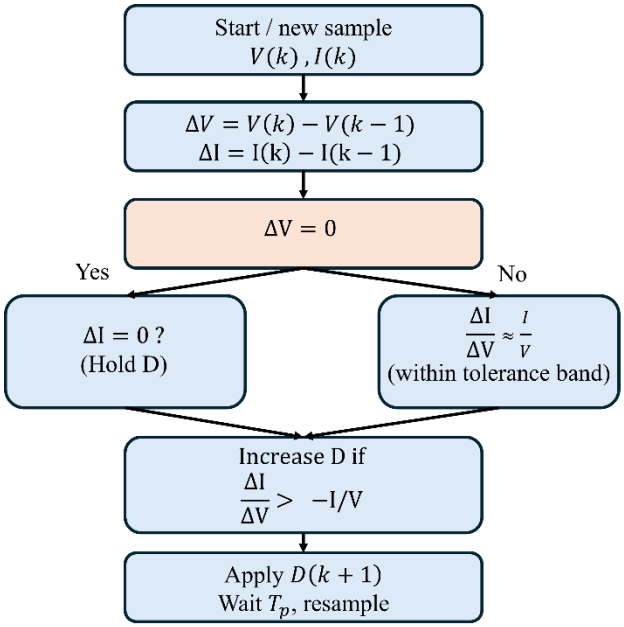



Figure 3-4: Flowchart of the Incremental Conductance (INC) algorithm, testing the conductance-equality condition of equation (3.3) [17, 51, 64, 68-70].

INC's practical hardware implementation must replace the exact equality of equation (3.3) - never met precisely with noisy, quantised measurements - with a tolerance band $\varepsilon$, so that the hold

condition becomes $|\Delta I/\Delta V + I/V| < \varepsilon$: too wide a band and the controller settles away from the true peak; too narrow a band and sensor noise triggers continuous, unnecessary perturbation. The width of $\varepsilon$ therefore trades steady-state sensitivity against oscillation exactly as the perturbation amplitude does for P&O [17, 70]. A representative hardware-validated implementation drives a Ćuk converter directly by duty cycle, the converter chosen specifically for its smooth port currents, which keep the algorithm's finite-difference estimates clear of the converter's own ripple [17] - an explicit instance of algorithm and converter chosen as a pair. Variable-step and drift-aware refinements of INC parallel those of P&O, including logic that explicitly guards against the inaccurate decisions that plain INC can make under fast-changing irradiance [51]. Figure 3-5 shows this tolerance-banded decision acting on the duty cycle of a boost stage.

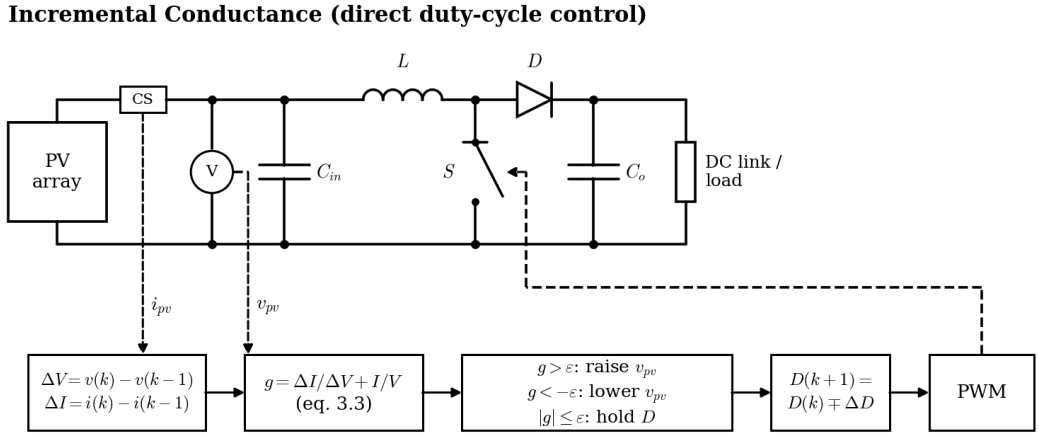


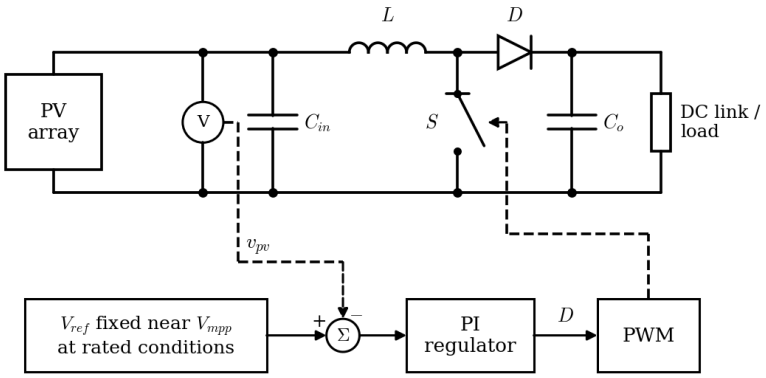

Figure 3-5: Circuit-level schematic of Incremental Conductance tracking on a boost stage in the direct duty-cycle structure: the finite differences ΔV and ΔI of the measured array voltage and current form the conductance test g = ΔI/ΔV + I/V of equation (3.3), compared with the tolerance band ±ε; since $v_{pv} = (1 - D)V_o$ for a boost stage, raising $v_{pv}$ means decreasing D, hence D(k+1) = D(k) ∓ ΔD. The ΔV = 0 branch of the flowchart is omitted for clarity [17, 51, 64, 68-70].

The drift failure mode introduced in Section 3.2.1 is worth making concrete, since it recurs as a benchmark condition throughout the remainder of this chapter. Consider a perturbation that has just increased the duty cycle, moving the operating point away from the peak on the P–V curve, at the same instant that a passing cloud edge reduces irradiance. Both effects reduce the measured power, so the P&O decision rule of equation (3.2) reads the combined power drop as confirmation that the last perturbation direction was wrong, and reverses again - compounding the error rather than correcting it. The controller can, in the worst case, be driven steadily away from the true MPP for as long as the irradiance transient continues, recovering only once conditions stabilise. The drift-free variant addresses this precisely by adding the sign of the measured current change as a second, independent piece of evidence, which the pure power-and-voltage-based test of equation (3.2) does not have access to [40].

### 3.2.3 Constant-Voltage and Constant-Current Methods

The constant-voltage (CV) method dispenses with searching altogether: it regulates the array to a fixed voltage reference, chosen once near the typical maximum-power voltage at rated conditions, exploiting the empirical regularity that $V_{mpp}$ remains a roughly constant fraction of $V_{\mathrm{oc}}$ across a useful range of irradiance (Section 1.5.1). This costs only one sensor and one control loop, at the price of a systematic, condition-dependent tracking error that grows as temperature (and, to a lesser degree, irradiance) moves the true MPP away from the fixed reference [64-66]. The dual constant-current method regulates to a fixed fraction of $I_{sc}$ in the same spirit. Both methods have been directly compared against a properly tracked reference on a hardware PV pumping installation, confirming the harvested-energy penalty relative to genuine tracking [71]. Neither method is competitive where energy yield matters, but both remain relevant as the cheapest possible fallback and as the theoretical basis of the fractional methods below. Figure 3-6 shows both as single-sensor, single-loop structures.

**(a) Constant voltage: one voltage sensor, one loop**




**(b) Constant current: one current sensor, one loop**

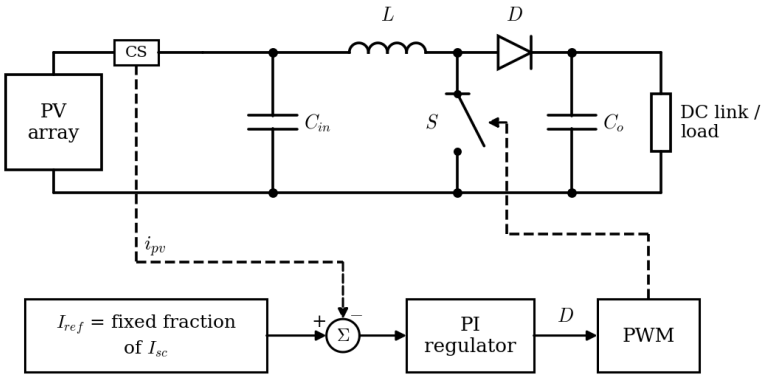



Figure 3-6: Circuit-level schematics of the constant-voltage and constant-current methods in the reference-based structure. (a) Constant voltage: a single voltage sensor and a proportional–integral loop hold $v_{pv}$ at a fixed reference $V_{ref}$ chosen near $V_{mpp}$ at rated conditions. (b) Constant current: a single current sensor (CS) and a proportional–integral loop hold $i_{pv}$ at a fixed fraction of $I_{sc}$. Neither method searches for the maximum power point [64-66, 71].

### 3.2.4 Fractional Open-Circuit Voltage and Short-Circuit Current

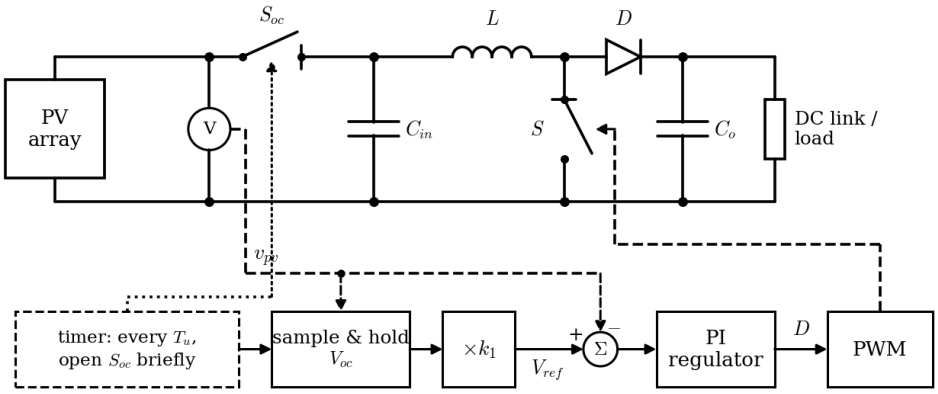
The fractional methods operationalise the same empirical regularity with a periodic re-calibration:

$$V_{mpp} \approx k_1 \cdot V_{oc} \quad , \quad I_{mpp} \approx k_2 \cdot I_{sc} \tag{3.4}$$

with proportionality constants commonly quoted in the region of $k1 = 0.71 - 0.82$ for the voltage and $k2 = 0.78 - 0.92$ for the current [65, 66, 69].

The control law periodically samples $V_{oc}$ or $I_{sc}$ , momentarily disconnecting or short-circuiting the array, or using a small unloaded pilot cell, and commands the corresponding fraction. Implementation is disarmingly cheap (one measurement, one multiplication), but the interruption required to obtain $V_{oc}$ or $I_{sc}$ costs harvested energy at every update, the constants drift with conditions and age, and the method fails outright under partial shading, since no single fraction of $V_{oc}$ identifies the global peak of a multi-modal characteristic [65, 69]. Refinements reduce the measurement tax directly: adaptive sampling adjusts the frequency and duration of the interruption to the prevailing power level [69]; improved formulations reduce the residual proportionality error [43]; and a sensorless hybrid estimates the short-circuit current without interrupting the array at all, handing the estimate to a P&O stage for fine refinement [72]. Given their bounded accuracy, the fractional methods survive in the modern literature less as stand-alone trackers and more as cheap initialisers - supplying a fast first estimate, and, in the global-search methods of Section 3.3.3, the search-space bound within which a more expensive method operates [64, 72, 73]. Figure 3-7 shows both variants, with the switch $S_{oc}$ that disconnects the array and $S_{sc}$ that short-circuits it.

**(a) Fractional open-circuit voltage (eq. 3.4)**




**(b) Fractional short-circuit current (eq. 3.4)**

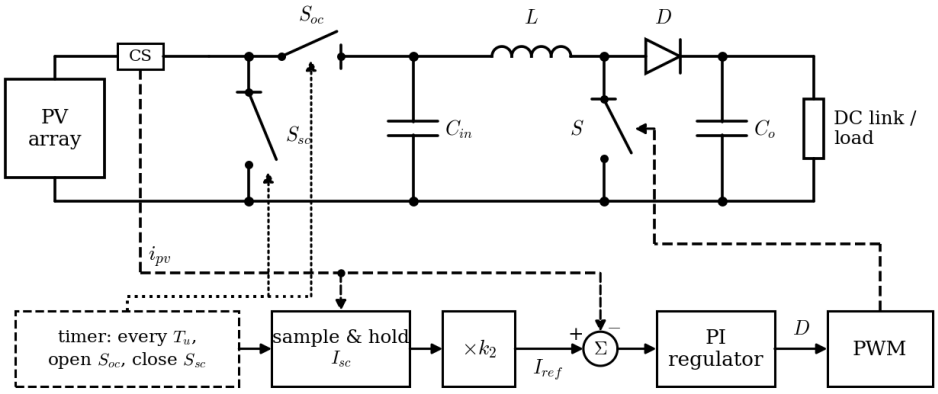



Figure 3-7: Circuit-level schematics of the fractional methods of equation (3.4) in the reference-based structure. (a) Fractional open-circuit voltage: every update period $T_u$ a timer briefly opens $S_{oc}$, so that the voltage sensor reads $V_{oc}$, which is held and scaled by $k_1$ to give $V_{ref}$. (b) Fractional short-circuit current: the timer opens $S_{oc}$ and closes $S_{sc}$, so that the current sensor reads $I_{sc}$, which is held and scaled by $k_2$ to give $I_{ref}$; opening $S_{oc}$ also keeps $C_{in}$ from discharging through $S_{sc}$. The array delivers no power while it is sampled, and a pilot cell can replace the switches [43, 64, 66, 69, 72, 73].

**Example 3.2 - Accuracy of the fractional open-circuit-voltage method**

**Given data**

- Module of Table 1-3: $V_{oc}$ = 39.0 V, $V_{mpp}$ = 32.0 V, $I_{sc}$ = 11.60 A, $I_{mpp}$ = 10.96 A at STC.
- ST090P(36) panel of [101]: $V_{oc}$ = 22.2 V, $V_{mp}$ = 17.6 V, $I_{sc}$ = 5.35 A, $I_{mp}$ = 5.11 A.

**Formulas**

$k_1 = V_{mpp}/V_{oc}$ $k_2 = I_{mpp}/I_{sc}$ (equation (3.4))

Fraction of the available power obtained with a fixed $k_1 = P(k_1 V_{oc})/P_{mpp}$

**Calculation**

Table 1-3 module: $k_1 = 32.0/39.0 = 0.82$; $k_2 = 10.96/11.60 = 0.945$

ST090P(36): $k_1 = 17.6/22.2 = 0.793$; $k_2 = 5.11/5.35 = 0.955$

Single-diode model of the Table 1-3 module at 25 °C (equations (1.2)–(1.3)):

| **Irradiance** | **Optimal $k_1$** | **Power with $k_1$ = 0.82** | **Power with $k_1$ = 0.76 (mid-range)** |
|---|---|---|---|
| 1000 W/m² | 0.819 | 100.0 % | 96.5 % |
| 600 W/m² | 0.839 | 99.5 % | 94.5 % |
| 200 W/m² | 0.857 | 98.5 % | 92.8 % |

**Result**

- Both modules have $k_1$ inside the quoted 0.71–0.82 range and $k_2$ above the quoted 0.78–0.92 range.
- A $k_1$ tuned at STC loses about 1.5 % at 200 W/m², while a mid-range value loses 3.5–7.2 %.

**Interpretation:** the method is accurate only if $k_1$ is chosen for the specific module, and even the optimal constant drifts with irradiance; under partial shading no constant identifies the global peak. The two data points for $k_2$ suggest that the commonly quoted range may underestimate modern modules, but two modules are not sufficient to generalise.

**Source:** [101] (datasheet values)

### 3.2.5 Comparative summary of conventional methods

Table 3-1 summarises the conventional family. It is worth recording explicitly, because it reframes the remainder of this chapter, that enhanced classical kernels (variable-step, adaptive-gain, self-predictive P&O; tolerance-banded INC) have substantially closed the classical speed–oscillation trade-off on ordinary hardware, achieving fast transients together with near-zero steady-state oscillation in validated experiments [41, 46]. What no refinement of step size, gain scheduling or stopping logic can supply, however, is global search capability: every method in this section climbs a local gradient, and under the multi-peak characteristics of Section 1.5.3 it will, by its own stopping criterion, converge on whichever peak it happens to find. This single limitation is the technical motivation for the advanced methods of Section 3.3.

Table 3-1: Comparative summary of conventional MPPT methods.

| Method | Principle | Sensors | Steady-state oscillation | Global search under shading | Typical implementation cost | Reference(s) |
|---|---|---|---|---|---|---|
| P&O (fixed step) | Perturb, compare power, keep/reverse direction | $V$, $I$ | Present, scales with step | No | Very low | [23, 24, 61] [64] |
| P&O (variable-step / self-predictive) | As above with adaptive step or predictive placement | $V$, $I$ | Reduced to near zero | No | Low | [40, 41, 46, 64] |
| Incremental Conductance | Test conductance equality, hold within a tolerance band | $V$, $I$ | Present, scales with band width | No | Low–moderate | [17, 51, 64, 68-70] |
| Constant Voltage / Current | Regulate to a fixed reference fraction of $V_{oc}$ or $I_{sc}$ | $V$, or $I$ | None (fixed operating point) | No | Very low | [64-66, 71] |
| Fractional $V_{oc}$/ $I_{sc}$ | Periodically sample $V_{oc}/I_{sc}$, command the fraction | $V$, or $I$ | Low, but a systematic bias | No | Low, with periodic energy loss | [43, 64, 66, 69, 72, 73] |

**Example 3.3 - P&O versus INC on the same converters: what the efficiency figures show**

**Given data**

- [100]: MATLAB simulation at 1000 W/m² and 25 °C; P&O and INC on conventional and ZVS Zeta and SEPIC converters (Table 1 of [100]).
- [101]: simulation with irradiance and temperature steps; P&O and INC on the buck, boost, buck–boost, Ćuk and SEPIC converters (Table I of [101]).
- The full data are collected in Table 4-5.

**Formulas**

$\Delta\eta = \eta_{INC} - \eta_{P\&O}$ (percentage points)  relative change of delivered power = $(P_{out,INC} - P_{out,P\&O})/P_{out,P\&O}$

**Calculation**

| **Converter [100]** | **Efficiency P&O → INC** | **Δη** | **Delivered power** |
|---|---|---|---|
| Zeta | 87.71 % → 93.98 % | +6.27 points | 8.780 → 8.672 W (−1.2 %) |
| ZVS Zeta | 89.68 % → 98.12 % | +8.44 points | +0.9 % |
| SEPIC | 83.39 % → 88.59 % | +5.20 points | 8.169 → 8.832 W (+8.1 %) |
| ZVS SEPIC | 90.62 % → 89.00 % | −1.62 points | −3.5 % |

| **Converter [101]** | **Efficiency P&O / INC** | **Tracking oscillation P&O / INC** |
|---|---|---|
| Buck | 98 / 96 % | 0.2 / 0.2 % |
| Boost | 98 / 97 % | 0.3 / 0.4 % |
| Buck–boost | 92 / 90 % | 1.2 / 0.9 % |
| Ćuk | 95 / 94 % | 1.8 / 1.6 % |
| SEPIC | 97 / 90 % | 2.1 / 0.7 % |

**Result**

- In [100] INC gives the higher efficiency on three of the four converters.
- In [101] P&O gives an equal or higher efficiency on all five, while INC gives the lower oscillation on the buck–boost, Ćuk and SEPIC converters.

**Interpretation:** the ranking of the two simplest algorithms reverses between studies and, within [100], between converters (ZVS SEPIC). In [100] the efficiency is the converter efficiency $P_{out}/P_{in}$, not the tracking efficiency of equation (3.1): with identical irradiance and temperature, INC settled at a lower input power for the Zeta (9.23 W against 10.01 W), so its higher conversion efficiency coexists with a lower delivered power, and ranked by delivered power INC is better only for the ZVS Zeta and the SEPIC. Because [100] does not report the available PV power, the tracking efficiency cannot be computed - an illustration of the joint operating-window criterion of Table 2-4. [101] does not define its efficiency metric, and its text and

> table disagree in places (its text credits INC with high efficiency on the boost converter, whereas its table gives 97% against 98% for P&O), so its figures support only coarse conclusions.
> **Source:** [100], [101]

### 3.2.6 Sensing and Practical Implementation Considerations

Every method surveyed in this section, and indeed every method surveyed in this chapter, is ultimately implemented on top of a physical sensing chain whose properties condition what the algorithm can actually achieve, independently of the decision logic itself. Two voltage and current transducers are the practical minimum: a voltage sensor (typically a resistive divider or an isolated Hall-effect or isolation-amplifier transducer for higher-voltage strings) and a current sensor (a shunt resistor, a Hall-effect sensor, or a current transformer for AC-coupled measurement points). Current sensing is, in practice, both the more expensive and the more noise-prone of the two measurements, which is part of the reason the single-sensor methods of Sections 3.2.3–3.2.4 remain attractive in strictly cost-driven designs despite their accuracy penalty [67]. The analogue-to-digital converter (ADC) resolution and sampling rate of the embedded controller set a further, often-overlooked floor: a 10-bit ADC resolves a 40 V range only to approximately 40 mV per bit, which can be comparable to or larger than the converter's own switching-ripple contribution (Section 2.1.2) and therefore becomes, in that case, the dominant term in the noise floor introduced in Section 3.1.2 rather than the switching ripple itself.

The choice between the two canonical control structures introduced conceptually in Chapter 2 - a direct duty-cycle structure, in which the tracking algorithm's output drives the pulse-width modulator with no intervening regulator, and a reference-based structure, in which the algorithm instead generates a voltage or current reference that a conventional proportional–integral inner loop enforces - is itself a sensing and implementation decision as much as a control-theoretic one. The direct structure is cheaper (fewer control loops to tune, no additional feedback sensor beyond the array-side pair) and is the structure used by several of the hardware-validated designs surveyed in this chapter [17, 73]; the reference-based structure adds design and tuning effort but conditions the plant the tracking algorithm sees, presenting it with a faster, better-damped closed-loop response than the raw converter would offer on its own, and is the structure typically preferred in stand-alone chargers and grid-connected two-stage systems where the inner loop's dynamics are engineered deliberately [25].

Table 3-2 compares the two structures directly, and Figure 3-8 shows them as block diagrams.

Table 3-2: The two canonical MPPT control structures compared [25]

| Attribute | Direct duty-cycle | Reference-based |
|---|---|---|
| Algorithm output | Duty-cycle increment | Voltage or current reference |
| Inner regulation loop | Absent | Present - typically proportional–integral |
| Sensing | Array voltage and current only | Array voltage/current plus the inner-loop feedback variable |
| Commissioning effort | Lower - no compensator to design | Higher - the inner loop must be designed and tuned |
| Dynamic behaviour presented to the tracking algorithm | Determined by the raw, open-loop converter dynamics | Determined by the designed closed-loop response, generally faster and better damped |
| Typical use | Simple, cost-driven designs; several hardware-validated research prototypes | Stand-alone chargers; two-stage grid-connected systems |

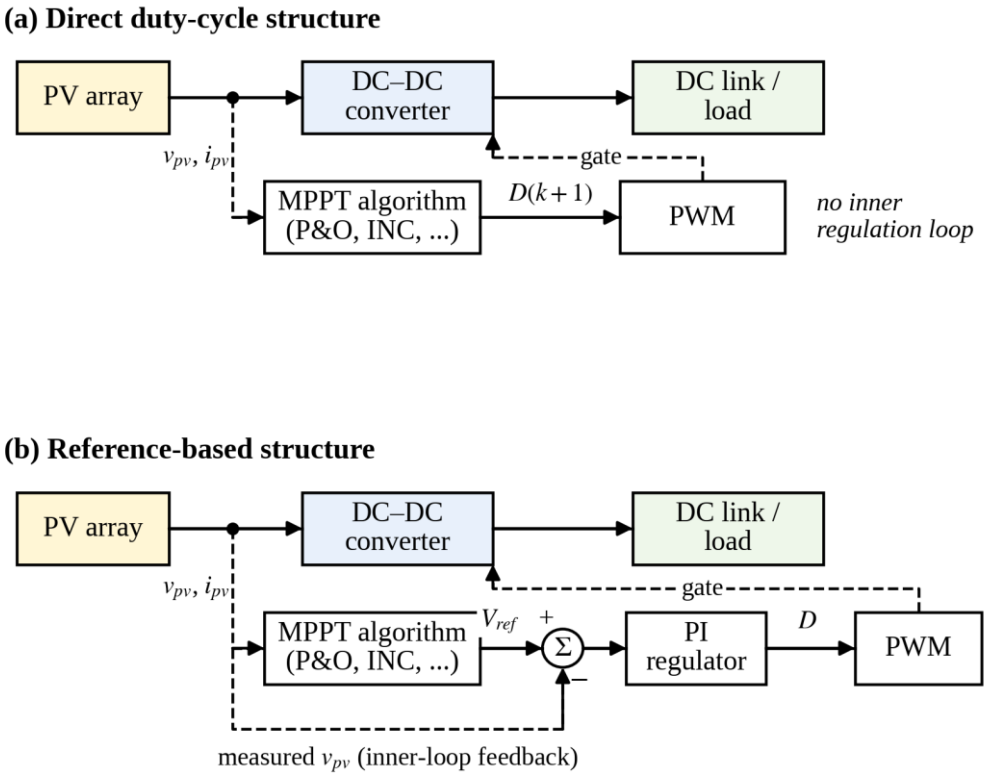



Figure 3-8: The two canonical MPPT control structures of Table 3-2: (a) direct duty-cycle structure, in which the algorithm output drives the PWM stage directly; (b) reference-based structure, in which the algorithm generates a voltage reference $V_{\mathrm{ref}}$ enforced by an inner proportional–integral (PI) loop [17, 25, description in Section 3.2.6].

## 3.3 Advanced and Intelligent MPPT Algorithms

Figure 3-9 places the families surveyed in this section within the overall classification used throughout the chapter. The advanced techniques share a common wager: replace the fixed local-search kernel with a structure that carries additional knowledge, encoded by a designer (fuzzy logic), learned from data (artificial neural networks), or discovered by a population of candidate solutions (metaheuristic optimisation), in order to buy either native handling of the array's nonlinearity without explicit modelling, or, in the population-based methods, genuine escape from the local-search ceiling identified in Section 3.2.5 [24, 64, 66].

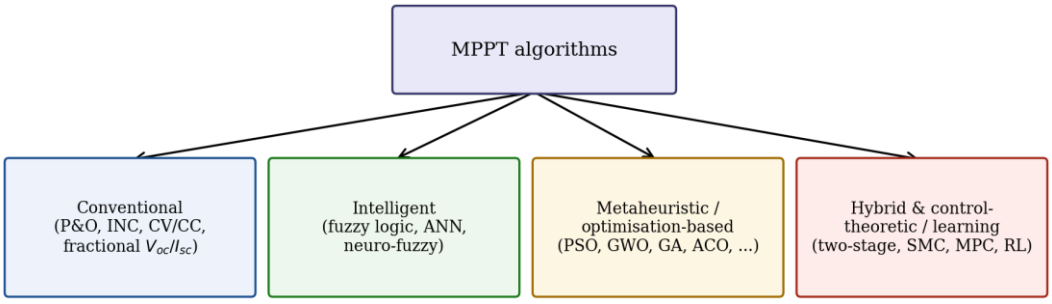


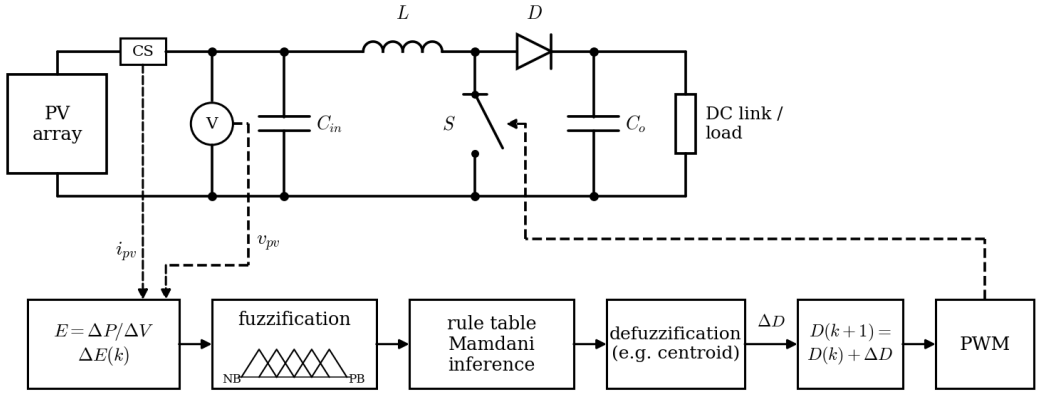

Figure 3-9: Classification of MPPT algorithm families surveyed in this chapter [24, 64, 66].

### 3.3.1 Fuzzy Logic Control

A fuzzy-logic MPPT controller replaces the crisp decision thresholds of the classical kernels with graded ones: tracking-error coordinates - typically a slope-based error $E = \Delta P/\Delta V$ and its increment $\Delta E$ - are mapped through membership functions into linguistic categories (e.g. negative big, zero, positive small), combined through a rule base, and defuzzified into a duty-cycle command or increment.

Two design choices govern the controller's behaviour: the shape of the membership functions (triangular, trapezoidal or Gaussian, typically five to seven per input variable) and the inference method - Mamdani inference, which is the more common and the more interpretable, and Takagi–Sugeno inference, which replaces the fuzzy output sets with a direct function of the inputs and is generally cheaper to compute, an advantage in real-time embedded implementation. Figure 3-10 shows both inference types acting on the duty cycle of a boost stage.

**(a) Fuzzy logic, Mamdani inference (direct duty-cycle control)**




**(b) Fuzzy logic, Takagi–Sugeno inference (direct duty-cycle control)**

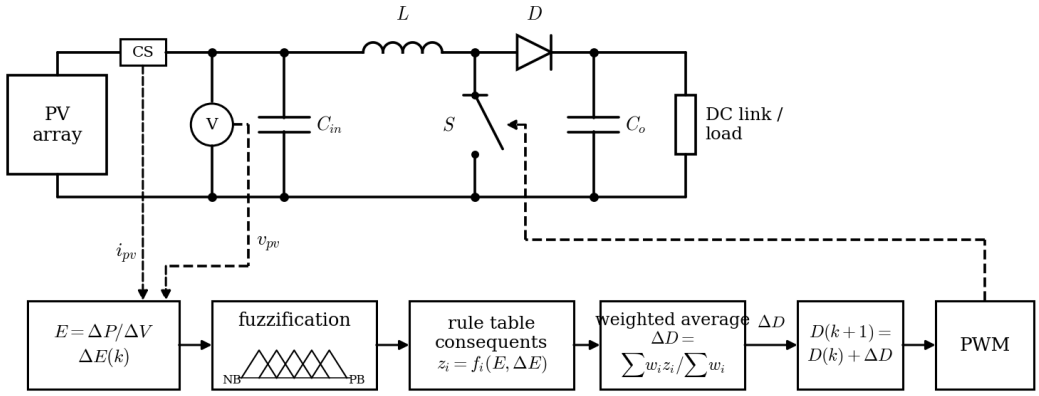



Figure 3-10: Circuit-level schematics of fuzzy-logic MPPT on a boost stage in the direct duty-cycle structure. The measured array voltage and current give the slope error E = ΔP/ΔV and its increment ΔE, which are fuzzified with typically five to seven membership functions per input (sketched from negative big, NB, to positive big, PB) and processed by a rule table. (a) Mamdani inference: the rules activate fuzzy output sets, which are defuzzified, for example by the centroid method, into the duty-cycle increment ΔD. (b) Takagi–Sugeno inference: the consequent of each rule is a direct function $z_i = f_i(E, \Delta E)$ of the inputs, and ΔD is the average of the consequents weighted by the rule firing strengths $w_i$, which is cheaper to compute online [64, 65, 74, 75].

The approach requires no explicit array model, accommodates the characteristic's nonlinearity natively, and the comparative record generally credits it with faster response, better drift avoidance and quieter steady-state behaviour than the classical kernels [64, 65]; implementation need not be expensive, having been realised on low-cost microcontroller boards [74]. The cost is concentrated entirely in design: the membership functions, rule table and defuzzification method constitute the controller, and a dedicated evaluation that varied both the membership-function shape and the converter's switching frequency found that the best-performing shape depends on the converter driving it - even a nominally model-free, "intelligent" controller is, in this sense, tuned to its actuator [75].

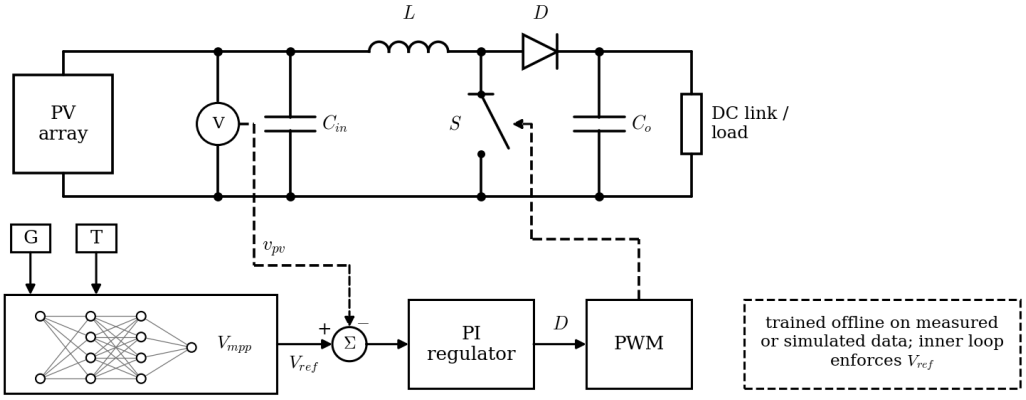
### 3.3.2 Artificial Neural Networks and Neuro-Fuzzy Methods

Artificial neural network (ANN) trackers use a network, generally trained offline on measured or simulated data, as a function approximator somewhere in the tracking chain - most commonly mapping measured or forecast irradiance and temperature to the maximum-power voltage, which is then enforced by a conventional inner regulator. A well-trained network reproduces the array's nonlinear mapping at negligible online computational cost and with no search-induced oscillation [64, 65]; its price is concentrated in training data, in silent performance degradation as the array ages or drifts away from the conditions represented in the training set, and in the recurring maintenance cost of retraining [65].

Network architecture ranges from shallow feed-forward multilayer perceptrons - the historical mainstream, mapping a handful of environmental inputs to a duty cycle or reference voltage through one or two hidden layers - to the deeper, sequence-aware architectures discussed as part of the recent literature in Section 3.4.2.

Neuro-fuzzy architectures, most commonly realised as an Adaptive Neuro-Fuzzy Inference System (ANFIS), combine the two ideas by using a trained network to generate the reference that a fuzzy-logic stage then enforces, so that the fuzzy layer absorbs the plant uncertainty and switching ripple that the network's static mapping does not itself model, while the network's training tunes the membership functions and rule weights automatically rather than by hand. A hardware-validated design of this kind - a neural reference generator feeding a fuzzy-controlled coupled-inductor interleaved boost converter, the converter explicitly selected for its stress and efficiency properties - was shown to outperform a conventional proportional–integral alternative on identical hardware, a clear instance of the converter and the intelligent controller having been co-selected [76]. Figure 3-11 shows (a) a neural reference generator with its inner regulator and (b) the neuro-fuzzy arrangement just described.

**(a) Artificial neural network reference generator (reference-based control)**




**(b) Neuro-fuzzy (ANFIS-type): neural reference, fuzzy enforcement**

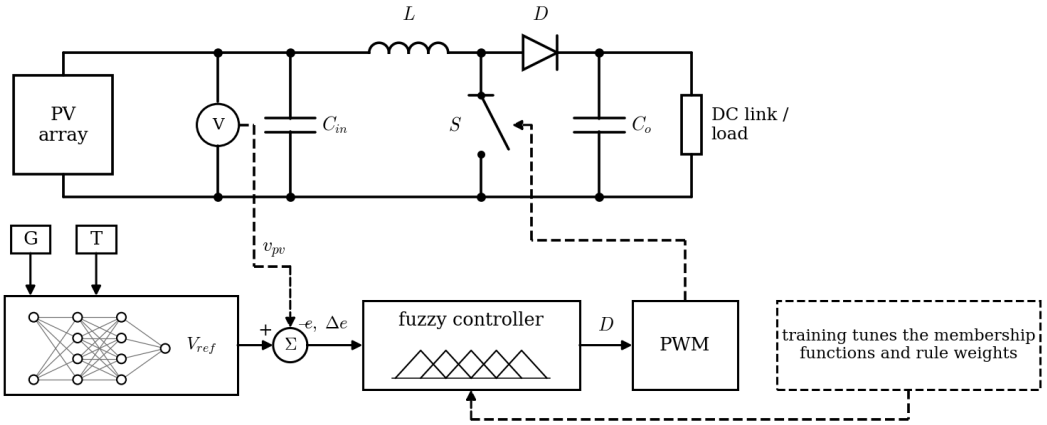



Figure 3-11: Circuit-level schematics of neural and neuro-fuzzy MPPT on a boost stage in the reference-based structure. (a) A feed-forward network with one or two hidden layers, trained offline, maps the measured irradiance G and module temperature T to the maximum-power voltage, which serves as the reference $V_{ref}$ of a conventional proportional–integral inner loop. (b) Neuro-fuzzy (ANFIS-type) arrangement: a trained network generates the reference, and a fuzzy controller acting on the error e and its increment Δe enforces it, its membership functions and rule weights being tuned by training rather than by hand [65, 86] (a) and [76] (b).

Table 3-3 collects the intelligent-tier methods against the same criteria used for the conventional family, to make explicit what the added sophistication buys and what it costs before the chapter turns to the population-based (metaheuristic) methods.

Table 3-3: Comparative summary of intelligent (fuzzy-logic, ANN, neuro-fuzzy) MPPT methods.

| Method | Model required | Global search under shading | Design/training cost | Real-time hardware cost | Reference(s) |
|---|---|---|---|---|---|
| Fuzzy logic (Mamdani) | None | No (unless explicitly trained/tuned for it) | High - membership functions and rule base by hand | Low; realised on low-cost microcontrollers | [64, 65, 74, 75] |
| Fuzzy logic (Takagi–Sugeno) | None | No | High, but cheaper to evaluate online | Very low | [64, 65] |
| Artificial neural network | Implicit, learned from data | Only if trained on shaded conditions | High - training data and offline training effort | Low at inference; training is offline | [64, 65] |
| Neuro-fuzzy (e.g. ANFIS) | Implicit + fuzzy structure | Only if trained for it | Highest - both training and rule design | Low–moderate | [76] |

### 3.3.3 Metaheuristic and Optimisation-Based Methods

The metaheuristic family replaces a single operating point with a population of candidate duty cycles, evaluated by the measured array power as a fitness function, and evolved by an update rule borrowed from stochastic global optimisation. Because a population sweeps a much wider portion of the characteristic than any local kernel, these methods are the ones demonstrated capable of locating the global maximum power point under the multi-peak characteristics of Section 1.5.3, at a cost that is structural and shared across the whole family: every fitness evaluation is a physical excursion of the operating point through the converter, which must be allowed to settle (equation 2.9) before the corresponding power measurement is trustworthy, so population size multiplied by the converter's settling time is the currency in which global search is purchased [24, 73, 77].

**Particle Swarm Optimisation (PSO)** is the most thoroughly documented representative. Each particle *i* is a candidate duty cycle $d_i$, updated by the canonical velocity–position rule

$$v_i(k+1) = w \cdot v_i(k) + c_1 r_1 (p_{\text{best,i}} - d_i(k)) + c_2 r_2 (g_{\text{best}} - d_i(k)) \quad (3.5)$$

$$d_i(k+1) = d_i(k) + v_i(k+1) \quad (3.6)$$

with $w$ the inertia weight, $c_1$, $c_2$ acceleration coefficients and $r_1$, $r_2$ uniform random numbers [73]. Figure 3-12 shows the swarm acting through a boost stage, together with the settling wait that every fitness evaluation requires.

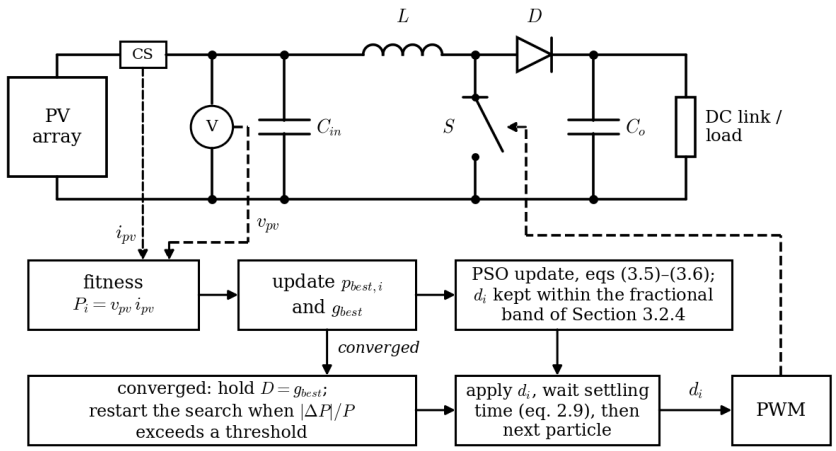



Figure 3-12: Circuit-level schematic of particle swarm optimisation MPPT on a boost stage in the direct duty-cycle structure. Each of the N particles is a candidate duty cycle $d_i$, applied through the PWM stage; after the settling time of equation (2.9), the measured power $P_i = v_{pv}i_{pv}$ is its fitness. The personal and global bests are updated, and equations (3.5)–(3.6) generate the next candidates, kept within the fractional band of Section 3.2.4 as in the hardware design discussed in the text. Once the swarm has converged, D is held at $g_{best}$ until a power change exceeding a threshold restarts the search [73].

- A hardware-validated direct duty-cycle implementation restricts the search domain a priori to the fractional band of Section 3.2.4 (importing known structure to shrink the search), eliminates the inner regulation loop entirely, and reports both global capture under partial shading and near-zero steady-state oscillation once the swarm collapses to a point [73].
- **Grey Wolf Optimisation (GWO)** organises its population by a leadership hierarchy with a contracting search radius, offering a comparable convergence record with fewer free tuning parameters than the classical PSO formulation, and is frequently deployed in a hybrid configuration - a global GWO stage locating the neighbourhood of the true peak, handed over to a classical P&O kernel for fast, quiet local refinement [64].
- **Genetic Algorithms (GA)** apply selection, crossover and mutation over generations; they are thorough but the slowest of the population methods in the tracking role, since every generation requires a full population of settled fitness evaluations, and their most durable role in the surveyed literature is accordingly offline - for instance tuning a fuzzy controller's membership functions and rule base by evolutionary search before that controller is deployed online at ordinary fuzzy-controller cost [78].
- **Ant Colony Optimisation (ACO)** imports a pheromone-biased sampling metaphor and has been reported to converge in fewer iterations than an equivalent PSO implementation and largely independently of the initial condition, in a centralised single-sensor-pair architecture for large, heavily shaded arrays [79].

- Further population-based methods reported for the shaded-tracking role include the bat algorithm [77] and cuckoo search [80], together with firefly variants adapted specifically for shaded operation [81]; the review literature catalogues this expanding family collectively as bio-inspired metaheuristics [82].
- A recent member of this family, the Pelican Optimisation Algorithm (POA), applied to MPPT on a high-gain converter with experimental validation, is examined as a case study in Section 3.4.6 [102].

A recurring practical concern across the whole population-based class, and one worth stating explicitly, is premature convergence: if the balance between the exploration and exploitation terms of an update rule such as equation (3.5) is set poorly, the population can collapse onto a local rather than a global peak before it has adequately explored the characteristic, defeating the purpose for which the method was chosen in the first place. This is why the parameter-tuning effort for a population method (inertia weight and acceleration coefficients for PSO, mutation and crossover rates for GA, and so on) is itself a non-trivial part of the method's implementation cost, alongside the physical settling-time cost already discussed - and why restricting the search domain a priori, as the fractional-band PSO implementation above does, is valuable for reasons of convergence reliability as well as of speed.

Deterministic alternatives to stochastic population search also exist**.** Golden-section and related interval-halving line-search methods maintain a bracket known to contain the peak and shrink it by a fixed geometric rule, reusing one evaluation per iteration; they require no stochastic parameters, converge in few, predictable evaluations, and a dedicated photovoltaic adaptation reports the ability to handle partial shading, though its own comparison found its static efficiency below that of an adaptive fuzzy–P&O hybrid - a reminder that even within the global-search class, rankings remain conditional on the comparison performed [83]. Figure 3-13 shows the corresponding update blocks of the other methods surveyed here, each of which takes the place of the PSO update block in the loop of Figure 3-12.

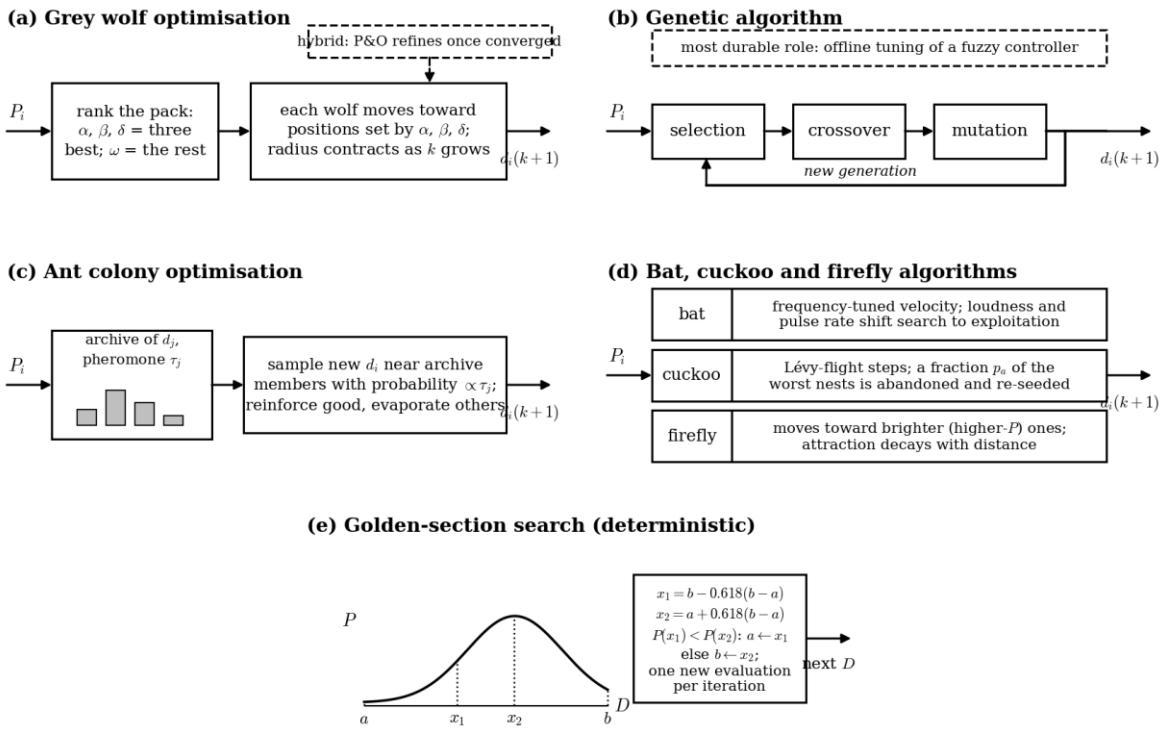



Figure 3-13: Update blocks of the other population-based methods and of golden-section search, each taking the place of the PSO update block in the loop of Figure 3-12: each receives the measured fitness $P_i$ of the current candidates and returns the next candidate duty cycles. (a) Grey wolf optimisation: the three best candidates (α, β, δ) guide the rest within a contracting radius, often followed by a P&O hand-over. (b) Genetic algorithm: selection, crossover and mutation produce each new generation; its most durable role is the offline tuning of a fuzzy controller. (c) Ant colony optimisation: new candidates are sampled near archive members with a probability proportional to their pheromone $\tau_j$. (d) Bat, cuckoo and firefly algorithms: family-specific stochastic steps. (e) Golden-section search: a deterministic bracket [a, b] around the peak is reduced by the golden ratio, reusing one evaluation per iteration [64] (a), [78] (b), [79] (c), [77, 80-82] (d) and [83] (e).

Table 3-4 collects the metaheuristic family. Three findings recur across essentially every comparative study in this class. First, the global-capture claim is genuine and repeatedly demonstrated: under conditions that defeat every method of Section 3.2, the population methods locate the true global peak [69, 73, 77, 80, 82]. Second, the differences advertised by the family names are frequently second-order relative to the costs the whole class shares - physical fitness evaluation at the converter's settling floor, harvest lost during the search itself, and the need for an explicit trigger to detect that a converged population has become stale and must search again [69, 73]. Third, the field's own practical compromise is consistently a hybrid: spend a global method's search budget only until the correct peak's neighbourhood is found, then hand over to a fast, quiet classical kernel for final convergence - the subject of Section 3.4.1.

Table 3-4: Metaheuristic and population-based MPPT methods.

| Method | Update principle | Global capture under shading | Principal cost | Typical role | Reference(s) |
|---|---|---|---|---|---|
| Particle Swarm Optimisation | Velocity/position update toward personal and global best | Demonstrated, hardware-validated | Population × settling time per fitness evaluation | Global tracker, direct duty-cycle | [73] |
| Grey Wolf Optimisation | Hierarchy-led encircling with contracting radius | Demonstrated | As above, fewer free parameters | Global stage of a hybrid scheme | [64] |
| Genetic Algorithm | Selection, crossover, mutation over generations | Demonstrated, in principle | Slowest of the class; disruptive search phases | Offline tuning of other controllers | [78] |
| Ant Colony Optimisation | Pheromone-biased candidate sampling | Demonstrated | Iteration-hungry; evidence largely simulation-based | Centralised tracker for large shaded arrays | [79] |
| Bat / Cuckoo / Firefly | Family-specific stochastic update rules | Demonstrated (dedicated studies) | Class-typical | Dedicated shaded-service trackers | [77, 80-82] |
| Golden-section / interval search | Deterministic bracket reduction | Reported for a dedicated adaptation | Low; no stochastic parameters | Low-cost global/quasi-global search | [83] |

## 3.4 Most Recent MPPT Algorithms in the Literature

This section surveys the techniques that currently define the active research frontier of MPPT:

- hybrid two-stage architectures that combine global and local search deliberately (Section 3.4.1);
- machine-learning and deep-learning predictors (Section 3.4.2);
- reinforcement learning, in which the tracking policy itself is learned through interaction (Section 3.4.3);
- model predictive control, in which the converter's own dynamic model becomes the centrepiece of the tracking law (Section 3.4.4);
- sliding-mode control, which answers the same problem from the opposite direction, requiring no converter model at all (Section 3.4.5).

These five families are followed by a case study of a recent metaheuristic algorithm, the Pelican Optimisation Algorithm, implemented on a high-gain converter with experimental validation (Section 3.4.6) [102].

For each, the discussion foregrounds the specific problem the technique addresses, its principal contribution, its demonstrated performance, its limitations, its computational requirements, and its suitability for practical deployment.

### 3.4.1 Hybrid MPPT Algorithms

The hybrid family is less a distinct set of algorithms than a design pattern applied across nearly every family already surveyed: assemble two stages whose failure modes are complementary, typically a coarse or global stage that relocates the operating point near the correct peak, followed by a fine, local stage that converges on it precisely and then stops perturbing. The pattern addresses directly the conclusion of Sections 3.2 and 3.3 - that no single technique combines global reach with a quiet, cheap steady state - by purchasing each capability only where it is needed.

The design carries a supervisory cost that belongs to neither stage individually:

- a handover condition, by which the coarse stage declares the correct neighbourhood found;
- a re-search trigger, by which the assembly recognises that a converged steady state has been invalidated by a new environmental disturbance and must search again.

Both are thresholds, and both must be set against the same converter-imposed noise floor that governs the classical kernels of Section 3.2 - a supervisor is not exempt from the interface arguments that apply to either of the stages it coordinates. Figure 3-14 summarises this two-stage structure and its supervisory logic.

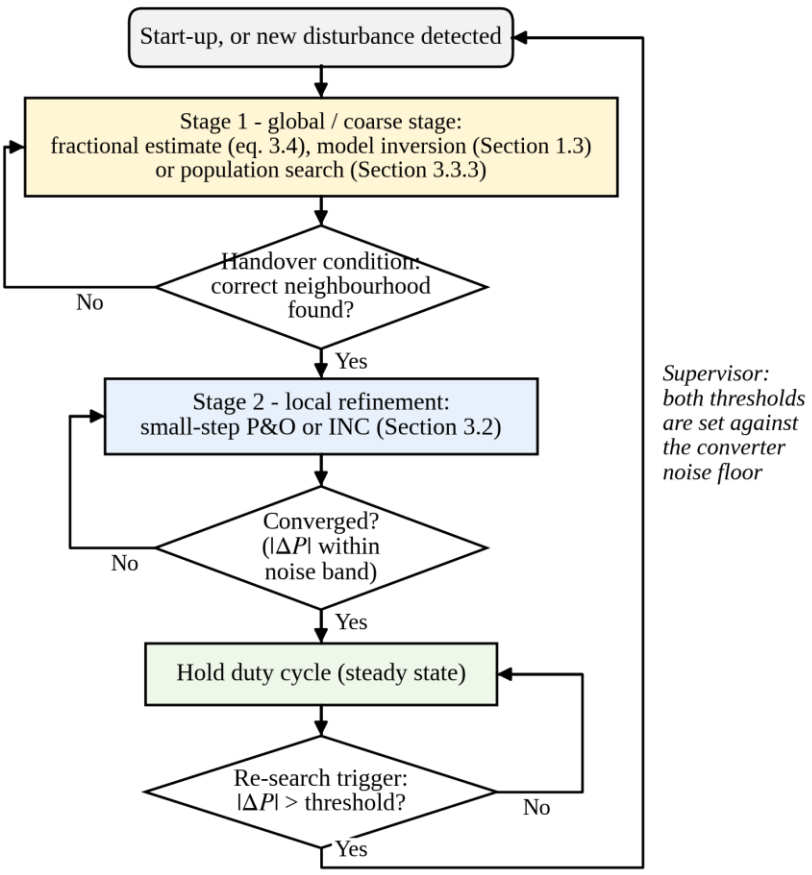



Figure 3-14: Generic two-stage (hybrid) MPPT structure and its supervisory logic: a global or coarse stage relocates the operating point near the correct peak, a local stage refines it, and two thresholds - the handover condition and the re-search trigger - coordinate the stages [64, 69, 72, description in Section 3.4.1].

Three recognisable sub-patterns recur in the literature.

1. Analytical–heuristic hybrids pair the fractional relations of equation (3.4) with a classical kernel: the fractional stage estimates the MPP voltage or current at start-up or after a detected disturbance, and a small-step P&O or INC loop refines the result, never having to perform a slow cold-start climb from an arbitrary point; a sensorless variant estimates the short-circuit current without interrupting the array, removing the fractional method's principal cost [72].

2. Model-based hybrids replace the fractional approximation with computation: an equivalent-circuit model of the array (Section 1.3) is identified online, the peak coordinates are computed by inversion rather than searched for, and a local kernel compensates the residual mismatch between the model's prediction and the hardware's actual peak - a double-diode-based implementation of this kind estimates the unmeasured irradiance and hands the estimate to a P&O stage for refinement [16, 84].

3. Metaheuristic–classical hybrids pair a population method with a classical kernel exactly as described in Section 3.3.3, the grey-wolf-assisted P&O scheme being the most cited representative [64].

4. A fourth, less common pattern combines two optimisers rather than an optimiser and a classical kernel - for instance a swarm method coupled with a gravitational-search stage - with one member supplying exploration and the other refinement; the review literature's verdict on this variant is candid that it deepens the global-search capability at a substantial cost in algorithmic and computational complexity, restricting it in practice to higher-end or experimental systems rather than low-cost installations [69].

The consistent finding across all three sub-patterns is that the hybrid assembly buys each stage's strength at each stage's price, plus a supervisor that must decide when to hand over from one stage to the other - a threshold that must itself be set against the converter's noise floor, exactly as the zero-oscillation hold of Section 3.2.1 requires [46]. Figure 3-15 shows a circuit-level implementation on a boost stage, in which the supervisor selects which stage commands the duty cycle.

**Hybrid (global + local) tracker with supervisor**

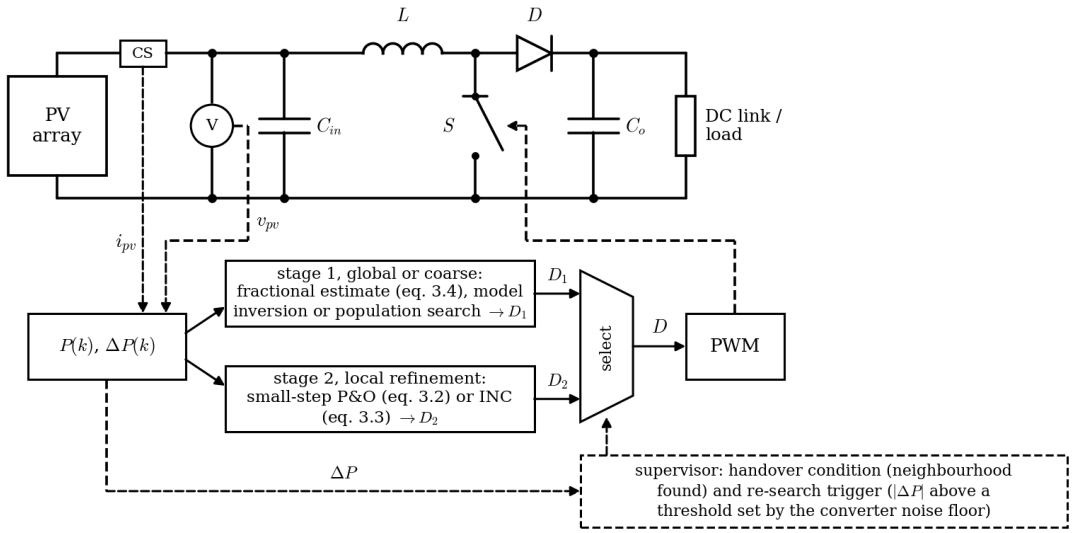



Figure 3-15: Circuit-level schematic of a hybrid (global + local) tracker on a boost stage: a global or coarse stage (fractional estimate, model inversion or population search) and a local refinement stage (small-step P&O or INC) each propose a duty cycle, and the supervisor selects which of them commands the converter, applying the handover condition and the re-search trigger described in Section 3.4.1 [16, 64, 69, 72, 84].

The value of pairing a global stage with a converter chosen to suit it is demonstrated quantitatively in the literature that varies both jointly:

- a hybrid particle-swarm/perturb-and-observe scheme implemented on a SEPIC converter reached approximately 99.5% tracking efficiency under uniform irradiance and retained roughly 83–99% under medium-to-high partial shading, outperforming the same algorithm family implemented on boost and Ćuk stages under identical shading scenarios [63] - direct evidence that the hybrid pattern's benefit is inseparable from the converter it is implemented on, reinforcing the central argument of Chapter 2;
- a separate comparison of four converters (buck–boost, SEPIC, Ćuk and Zeta) under three tracking algorithms similarly found that settling time and steady-state efficiency differed for every converter–algorithm pairing tested, with no single combination best on every criterion [47];
- two simulation studies in which P&O and INC are applied to several converters likewise find that the efficiency ranking of the two algorithms changes with the converter and between studies [100, 101] (Example 3.3 and Table 4-5).

A further, architectural form of hybridisation deserves mention because it relocates the solution from the algorithm to the hardware**:** distributed tracking and differential power processing, in which each module or sub-string is given its own small converter and its own simple local kernel, reduce mismatch loss at its physical source rather than tracking around it after the fact, at the cost of additional converters and sensors [11, 85]. The review literature states the underlying principle explicitly: tracking performance can be improved not only by modifying the algorithm but by co-designing the system architecture and the placement of the power electronics [69] - the same conclusion this thesis reaches independently from the converter side in Chapter 2.

### 3.4.2 Machine Learning and Deep Learning-Based MPPT

The data-driven line extends the neural-network idea of Section 3.3.2 into deeper, sequence-aware and attention-based architectures, and into richer input representations. A dedicated review of neural-network MPPT reports that trained trackers commonly average close to 98% tracking performance under uniform conditions, with faster convergence and reduced steady-state oscillation than conventional methods once trained [86]. A significant recent development is the shift toward sensorless input sets: rather than requiring irradiance and temperature sensors (expensive, in need of calibration, and - for a partially shaded array - sampling the environment only at a point while the shading pattern varies across the array), sensorless formulations train on sequences of terminal voltage and current alone, inferring the characteristic's shape from electrical

feedback and reducing the sensing chain to the pair of measurements every classical method already uses [65, 86].

Sequence-aware architectures (e.g. long short-term memory networks) extend the mapping temporally, exploiting the fact that irradiance arrives in patterns and temperature drifts with thermal mass rather than changing instantaneously; attention-based (transformer) architectures have been applied to predict the maximum-power operating voltage from a rich set of environmental and temporal features, one study reporting a mean absolute percentage error of 0.47% on the predicted operating voltage using meteorological data from fifty locations [87]. Figure 3-16 shows a sensorless, sequence-based tracker of this kind acting on a boost stage through an inner voltage loop.

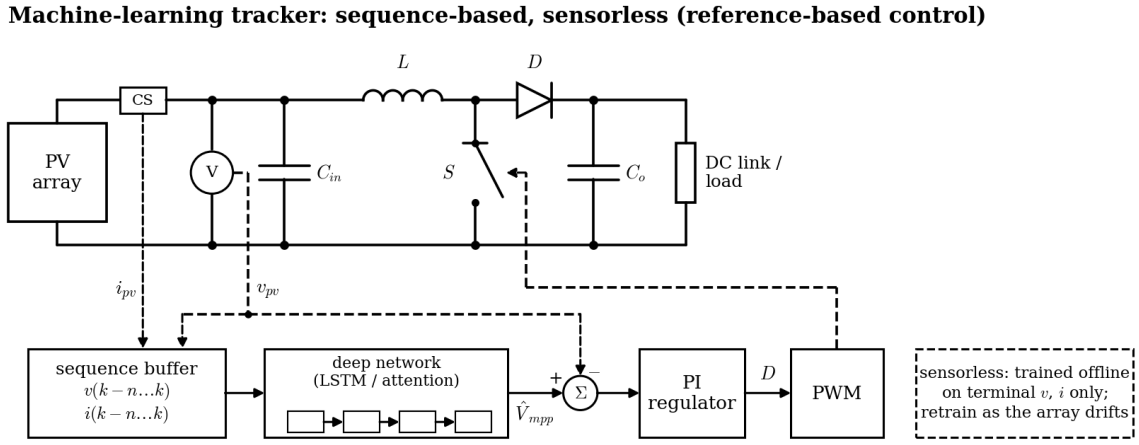



Figure 3-16: Circuit-level schematic of a sensorless machine-learning tracker on a boost stage in the reference-based structure: a buffer of recent terminal voltage and current samples feeds a sequence-aware deep network (for example a long short-term memory or attention-based network), whose prediction of the maximum-power voltage is enforced by a proportional–integral inner loop. The network is trained offline and must be retrained as the array drifts away from its training conditions [65, 86, 87].

Reported accuracy figures of this kind require a specific qualification, however: where the predicted voltage is evaluated only against a simulated current–voltage curve, with no converter in the control loop, the reported figure is a property of a predictor evaluated against a model, not of a tracking system evaluated against hardware, and none of the converter-facing criteria of Chapter 2 are exercised by such an evaluation [87]. This qualification does not diminish the genuine value of the predictive approach, but it does bound what the reported figure licenses a reader to conclude.

Four limitations recur across the data-driven class as a whole, and each is, at root, a version of the same problem - the knowledge embedded in the model is borrowed from training data rather than derived from physics:

1. Data dependence: a network knows the array and conditions represented in its training set, and ageing, soiling and location-specific weather move the deployment distribution away from that set silently, without any signal that the mapping has degraded [65, 86].
2. Implementation cost: deep architectures strain the embedded controllers that a low-cost installation can support, and the review literature identifies this gap between simulated performance and commercially deployable hardware as a recurring barrier [65].
3. Interpretability: where a P&O or INC kernel has a transparent operating principle, a deep network does not, which complicates the already under-formalised question of stability guarantees (Section 3.4.4).
4. Evidence base (the most consequential limitation for a review of this kind): a dedicated review of the neural-MPPT literature notes explicitly that many of the studies it surveys report results in simulation environments the reviewers could not independently verify [86] - a reproducibility observation echoed by the comparative discussion of Chapter 4.

### 3.4.3 Reinforcement Learning Approaches

Reinforcement learning (RL) formalises what every perturbation-based tracker has, in effect, been doing informally since Section 3.2.1: acting on the plant, observing a reward, and adjusting behaviour. The tracking problem is cast as a Markov decision process - the state assembled from terminal measurements and their recent history, the action a duty-cycle adjustment (or, in the finite-control-set coupling of Section 3.4.4, a switch state directly), and the reward built from the extracted power - with the policy, which the classical kernels hard-code as a fixed rule, instead learned through interaction [37, 65, 88].

- Value-based methods (Q-learning and its deep variant, the Deep Q-Network) learn an action-value function that estimates the expected future reward of taking a given action in a given state, and select actions that maximise it; because the action space in a value-based formulation is discrete, the duty cycle must be quantised, trading resolution against the size of the resulting table or network.
- Actor–critic architectures, including deterministic policy-gradient methods, instead learn a continuous policy directly - an actor network that outputs the duty-cycle command, and a critic network that estimates the value of the actor's choices and supplies the learning signal - which better matches a continuously adjustable duty cycle and is accordingly the more common choice in recent photovoltaic applications of RL.

The promise of the approach is genuinely distinctive: a model-free policy, adapted specifically to the array–converter pair on which it is trained, in principle internalises the actuation-law shape, the settling dynamics and the ripple signature that the rest of this thesis has treated as design inputs to be reasoned about explicitly. Continuous-action architectures (actor–critic methods, including deterministic policy-gradient variants) are the natural fit for a continuously adjustable duty cycle, since tabular value-learning methods (Q-learning) require the action space to be discretised, trading resolution against table size and convergence time [88]. Figure 3-17 shows an actor–critic tracker of this kind acting on the duty cycle of a boost stage.

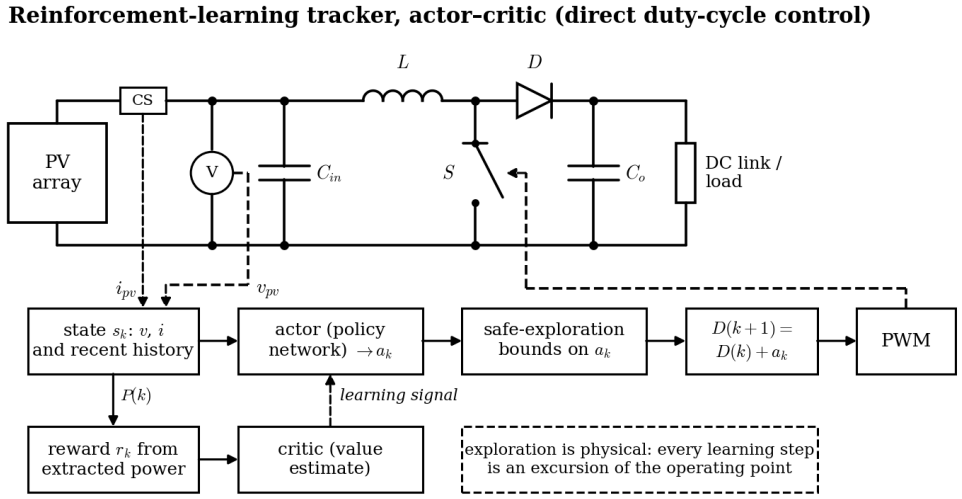



Figure 3-17: Circuit-level schematic of an actor–critic reinforcement-learning tracker on a boost stage in the direct duty-cycle structure: the actor maps the state (terminal voltage, current and their recent history) to a duty-cycle adjustment $a_k$, limited by safe-exploration bounds, while the critic estimates the value of the actor's choices from a reward built on the extracted power and supplies the learning signal. Every learning step is a physical excursion of the operating point [37, 65, 88].

A widely cited application addresses partial-shading tracking with a continuous state–action deep RL formulation and an accompanying open-source shaded-array simulation environment, reporting deviations of under one per cent from the theoretical maximum power point [89]. This particular result, however, was subsequently the subject of a formal published comment identifying methodological problems - an approximate array model, a metric computed against that same approximate model, and, most tellingly, a finding that the proposed technique always converged to the first peak encountered on the shaded characteristic rather than reliably to the global one [90]. This episode is recorded here because it is directly instructive for how RL-based MPPT results should be read: a claimed accuracy figure is only as trustworthy as the model against which it was computed, and a "global-capture" claim under partial shading must be demonstrated on shading patterns whose global peak is not the first one a local climb would encounter, or the

demonstration shows only that the agent, like the classical kernels of Section 3.2, climbed the nearest hill.

The costs of reinforcement learning are distinctive and structurally serious for a photovoltaic actuator:

- Exploration is physical: every learning step is a real, generally sub-optimal excursion of the operating point through the converter, recovering the population-method cost of Section 3.3.3 in sequential form, and an insufficiently constrained exploratory policy can, in principle, drive the converter into voltage or current excursions that stress or damage it - designing safe exploration bounds remains an open problem and a principal reason RL deployment on hardware lags the simulation literature [37, 65].
- Training contends with a non-stationary environment, since the irradiance trajectory of Section 1.5.2 moves the problem under the learner.

The strongest experimentally validated evidence for learning-based control of power converters in this corpus in fact sits on the converter-control side rather than the pure-tracking side: an online actor–critic scheme that learns to compensate unmodelled converter dynamics within a model-predictive structure, with closed-loop boundedness established by a formal (Lyapunov) argument rather than merely assumed, and validated on hardware [37] - a result that anticipates the fusion with model predictive control discussed next.

### 3.4.4 Model Predictive Control

Model Predictive Control (MPC) brings a receding-horizon optimisation directly to the converter interface: at each control step, a model of the array-plus-converter system predicts the consequence of each candidate actuation over a short horizon, a cost function scores the candidates, the best candidate's first action is applied, and the computation repeats at the next step with fresh measurements [91]. In its finite-control-set form, native to power electronics, the candidate set is simply the converter's discrete switch states, so the pulse-width modulator disappears from the loop entirely and the controller's structure coincides with the actuator's [91]. A representative cost function for MPPT service weighs the predicted array power error against penalties on inductor current and switching activity,

$$J = \lambda_1(P_{mx} - P_{pv}(k+1))^2 + \lambda_2(i\mathrm{L}(k+1) - I_{max})^2 + \lambda_3 \cdot f_{sw} \quad (3.7)$$

so that power extraction, component stress, and switching effort are balanced inside a single control layer rather than through nested, separately tuned loops [91].

The line's photovoltaic origin is comparatively well hardware-validated:

- the founding implementation combines a modified, current-based incremental-conductance objective with a two-step-horizon predictive controller on a boost stage, reporting both simulation and experimental results, faster and more accurate than the conventional baseline during irradiance transients [92];
- recent formulations extend the approach across converter families and system contexts, including coordinated tracking and DC-link or droop regulation in distribution-connected service [93], and a predictive tracker paired explicitly with a purpose-designed high step-up converter, in which the algorithm additionally replaces an output-voltage sensor with an observer to reduce sensor count [94].

Two implementation families divide the MPC literature, and the distinction maps directly onto the two control structures introduced in Chapter 2:

- In the fixed-switching family, a predictive observer of the photovoltaic model estimates the optimal array voltage or current, which is then compared with the measured value and converted into a duty-cycle command by a conventional proportional–integral regulator and modulator; the switching frequency remains constant, so downstream filter and electromagnetic-interference design proceeds conventionally, and the scheme integrates readily into existing pulse-width-modulated platforms.
- In the variable-switching (finite-control-set) family, the converter's discrete-time model selects the switch state directly with no modulator at all, which buys the fastest possible actuation at the cost of a switching frequency that is variable and spectrally spread, complicating filter design.

The fixed-switching form is therefore the lower-risk retrofit onto an existing platform, while the finite-control-set form is the more thoroughgoing realisation of the predictive idea. The finite-control-set structure is shown in Figure 3-18(a).

MPC's principal limitation is named in its own title: it requires a model.

- Prediction quality is bounded by model quality, and prediction accuracy therefore degrades under parameter drift, unmodelled switching-frequency effects, and - critically for

photovoltaic service - a change in which equations describe the plant: a predictive controller built on the continuous-conduction-mode relations of Chapter 2 computes confident forecasts from equations that no longer describe the converter once it crosses into discontinuous conduction, a specific and, on the reviewed evidence, under-treated exposure of the method.

- Computationally, enumerating candidate switch states within each control period grows with horizon length and converter order, pushing implementations toward digital signal processors or programmable logic [91, 95].

The response the literature has converged on is learning-augmented prediction: where the converter's model is unknown, drifting, or simply unpublished by the topology literature that proposed it (Chapter 2), a learned estimator or network approximates the missing dynamics online, restoring predictive control's benefits where its admission requirement - a usable model - would otherwise not be met [37].

### 3.4.5 Sliding-Mode Control

Sliding-Mode Control (SMC) answers the model-dependency problem of MPC from the opposite direction: it is a variable-structure method that requires no explicit converter model at all. A sliding surface $\sigma$ is defined directly on the tracking objective - for instance on the power gradient, $\sigma = dP/dI_{pv}$, or on the conductance-equality condition of equation (3.3) - and a discontinuous switching law drives the system trajectory onto that surface and holds it there; once on the surface, the closed-loop dynamics are fixed by the surface itself rather than by the converter's parameters, giving guaranteed robustness against parameter, line and load uncertainty and, unlike a linear controller designed on a small-signal model valid at one operating point, consistent large-signal transient behaviour across the entire operating range that a photovoltaic source visits [96, 97].

The practical cost of SMC has a name: chattering. Because real switching cannot occur at the infinite frequency the ideal law assumes, the trajectory overshoots and oscillates about the sliding surface rather than gliding along it, which appears at the array terminals as high-frequency ripple, forces the operating point off the true peak, radiates electromagnetic interference, and inflates conduction losses (which scale with the square of the r.m.s. current) [96].

The literature has converged on two mitigations that preserve the method's robustness while smoothing the resulting command:

- integral/double-integral surface terms, which suppress steady-state error and reduce high-frequency switching under wide load variation;
- second-order super-twisting formulations, which apply the discontinuous action to a higher derivative of the sliding variable - rather than to the duty cycle directly - so that the gate command itself is continuous even though the underlying control law remains discontinuous one derivative up, substantially reducing output ripple relative to conventional SMC while retaining the large-signal robustness that motivates the technique in the first place [98].

The two control-theoretic methods surveyed in this section are complementary rather than competing along a single axis, and the complementarity is worth stating plainly because it recurs, in different clothing, throughout the emerging hybrid and learning-augmented literature of Sections 3.4.1 to 3.4.3: SMC trades a converter model for switching-induced ripple, while MPC trades model-free operation for anticipation.

- A designer facing a converter whose dynamic model is unpublished or unreliable (Section 2.5.2) has, in sliding-mode control, a genuinely model-independent route to robust large-signal tracking;
- a designer with access to a validated model and the computational budget to exploit it has, in model predictive control, the more direct route to jointly optimised performance against explicit constraints.

Figure 3-18 contrasts the two control structures. Figure 3-19 shows the fixed-switching and super-twisting variants described above.

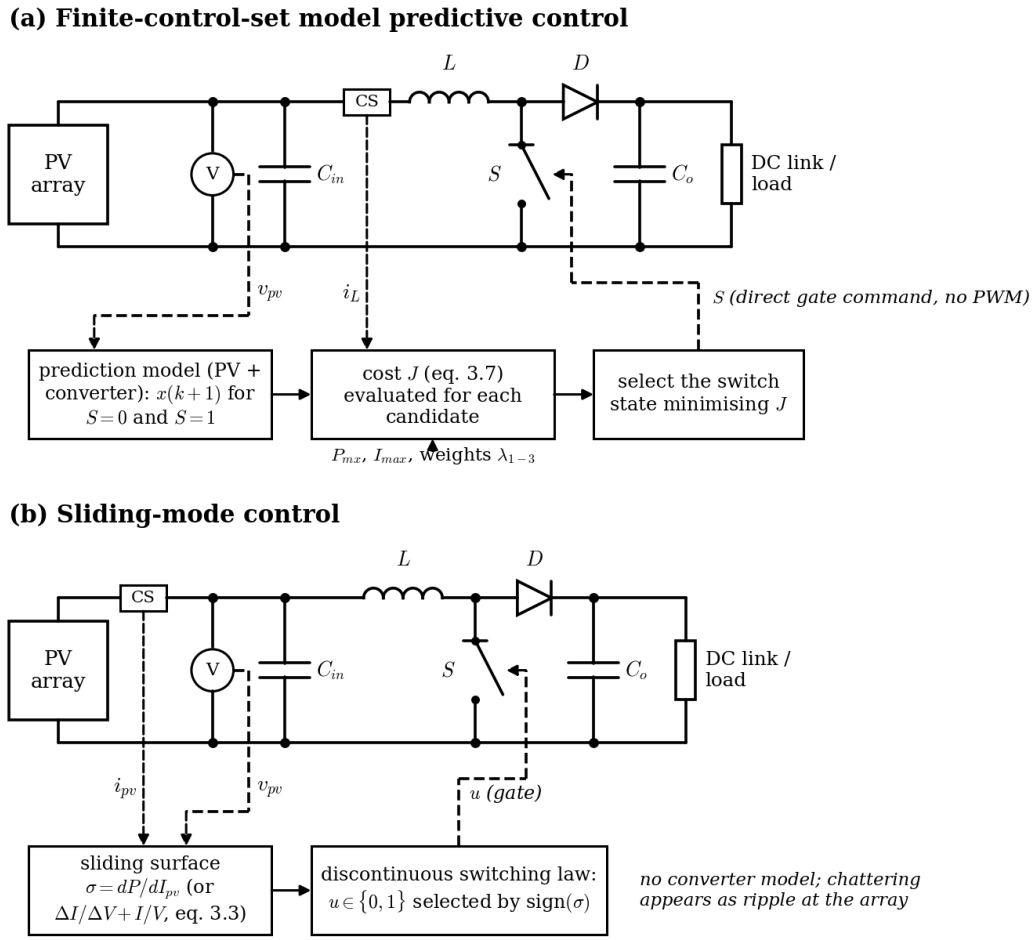



Figure 3-18: Circuit-level control structures, on a boost stage, of (a) finite-control-set model predictive control, in which a prediction model fed by the measured $v_{pv}$ and $i_L$ and the cost function of equation (3.7) select the switch state directly, and (b) sliding-mode control, in which a discontinuous switching law drives the system onto a sliding surface defined on the tracking objective [91, 96, 97, descriptions in Sections 3.4.4–3.4.5].

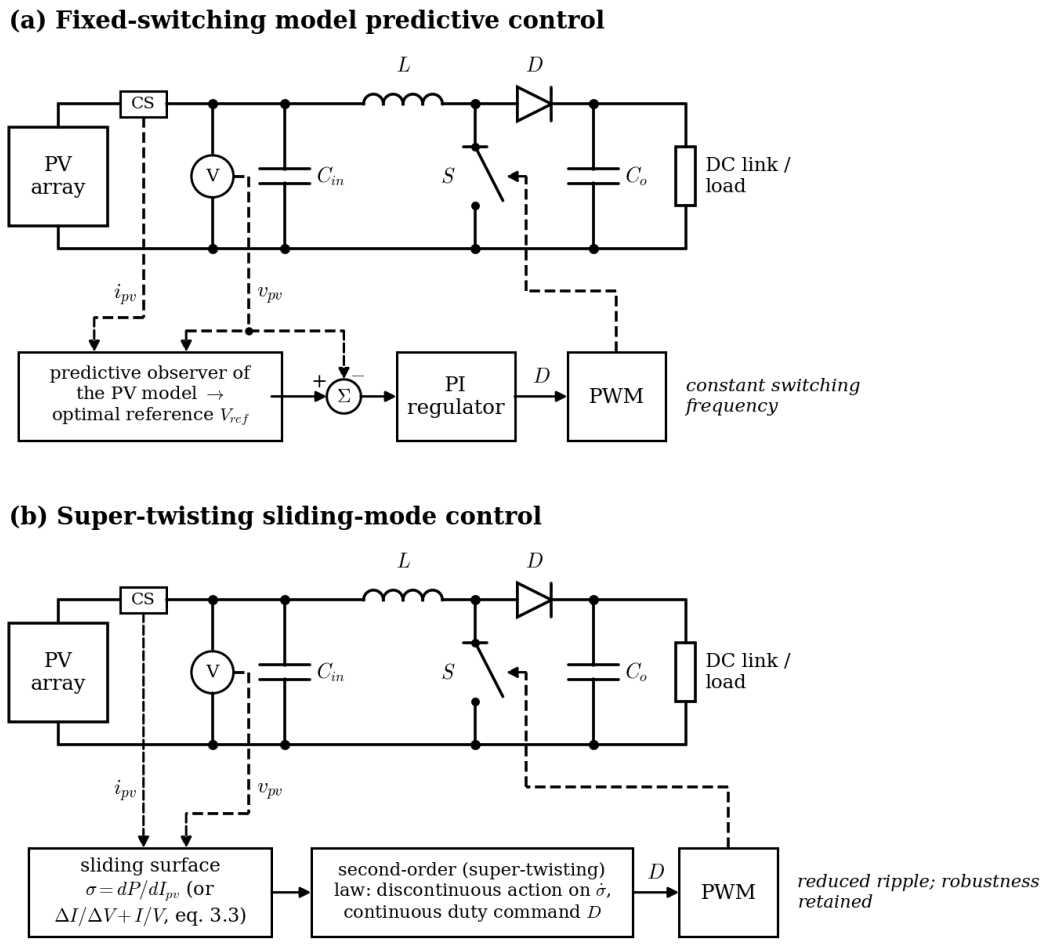



Figure 3-19: Circuit-level schematics of the two variants described in Sections 3.4.4–3.4.5: (a) fixed-switching model predictive control, in which a predictive observer of the photovoltaic model supplies the optimal reference to a conventional proportional–integral regulator and modulator, so that the switching frequency stays constant; (b) super-twisting sliding-mode control, in which the discontinuous action is applied to the derivative of the sliding variable, so that the duty-cycle command passed to the modulator is continuous [91] (a) and [98] (b).

Table 3-5 sets sliding-mode and model predictive control against one another across the dimensions that decide their selection for a given application. One structural asymmetry deserves particular emphasis: because SMC assumes no plant model, it cannot be surprised by the conduction-mode boundary of Section 2.1.2 the way MPC can - a controller that knows nothing about its plant's equations cannot be invalidated by a change in those equations. Predictive control buys anticipation at the price of a model's fragility; sliding-mode control buys invariance to the model at the price of switching-induced ripple. The strongest sliding-mode evidence in the surveyed literature, similarly to the reinforcement-learning case above, is concentrated on the converter-control side rather than on dedicated MPPT studies, with tracking-specific applications documented but comparatively less numerous [96, 97].

Table 3-5: Sliding-mode control and model predictive control compared for photovoltaic MPPT service.

| Dimension | Sliding-mode control | Model predictive control | Reference(s) |
|---|---|---|---|
| Dependence on the plant model | None once on the surface | Total - prediction quality is model quality | [96, 97] |
| Large-signal validity | Consistent across the operating range | Explicit prediction replaces small-signal design | [96, 97] |
| Computational demand | Low to moderate | High - enumeration each control period | [96] |
| Characteristic failure mode | Chattering (ripple, EMI, thermal cost) | Degradation under model mismatch / mode change | [96, 98] |
| Constraint handling | Indirect, via surface/gain design | Direct, inside the cost function | [91] |
| Photovoltaic tracking evidence | Documented; converter-control literature stronger | Hardware-validated from its founding implementation | [96, 97] |

Table 3-6 draws the five techniques of this section into a single comparative view against the criteria that most directly determine practical adoption: the problem each technique addresses, its main contribution, its principal advantage and limitation, its computational requirement, and its practical suitability.

Table 3-6: Critical comparison of the most recent MPPT techniques surveyed in Section 3.4.

| Technique | Problem addressed | Main contribution | Computational requirement | Response to fast irradiance changes | Practical suitability | Reference(s) |
|---|---|---|---|---|---|---|
| Hybrid (global + local) | No single classical method is both global and quiet | Combines a coarse global/analytical stage with a fast, quiet local kernel | Low to moderate (dominated by the coarse stage) | Good once converged; transition governed by an explicit handover rule | High - the field's default practical compromise under shading | [16, 64, 69, 72, 84] |
| Machine learning / deep learning | Nonlinear, shading-affected mapping learned from data rather than derived online | Fast inference; sensorless (electrical-feedback-only) variants remove environmental sensors | Low at inference; high for training, offline | Good if representative training data exists | Moderate - limited by data dependence and ageing drift | [65, 86, 87] |
| Reinforcement learning | Fixed decision rules cannot adapt to the specific array–converter pair | Learns a pair-specific policy through interaction; can fuse with MPC to compensate unmodelled dynamics | High during training; moderate at deployment | Potentially strong, but exploration itself is physical and costly | Low to moderate - safety during exploration and validation maturity remain open issues | [37, 65, 88-90] |
| Model predictive control | Converter constraints and tracking objective are not jointly optimised by cascaded linear loops | Single cost function unifying tracking, current limits and switching effort; anticipates rather than waits out transients | High - enumeration of candidates each control period | Very good, provided the model remains valid | Moderate to high - limited chiefly by model availability and DSP/FPGA cost | [91-95] |
| Sliding-mode control | Linear controllers are only valid near one operating point; PV sweeps a wide range | Model-free invariance to a wide operating range; immune to conduction-mode changes | Low to moderate | Very good - large-signal consistency by design | High, subject to managing chattering (e.g. via super-twisting forms) | [96-98] |

### 3.4.6 Case Study: Pelican Optimisation Algorithm on a High-Gain Converter

Metaheuristic MPPT research continues to produce new population-based algorithms (Section 3.3.3), and the most recent examples increasingly pair the algorithm with a purpose-selected converter. A representative 2025 study by Akter et al. [102] applies the Pelican Optimisation Algorithm (POA) - a population-based algorithm modelled on the two-phase hunting behaviour of pelicans and originally proposed for general engineering optimisation - to MPPT, and couples it with a single-switch high-gain DC–DC converter (Figure 3-21). The study is

examined here because it combines three elements that this thesis argues should be read together: a recent global-search algorithm, a high-gain converter selected for its input-current behaviour, and an experimental set-up of the kind the comparative reviews find scarce (Section 4.3.5).

In the MPPT formulation of [102], each pelican is a candidate PV operating voltage and its fitness is the corresponding measured power. The population is initialised randomly between the lower and upper bounds of the search space; each iteration then comprises an exploration phase, in which every candidate moves towards or away from a randomly generated prey position depending on whether that position has a better fitness, and an exploitation phase, in which each candidate searches a neighbourhood whose radius $R(1 - t/T)$ shrinks with the iteration count $t$ ($R = 0.2$, $T$ the maximum number of iterations). A new position is accepted only if it improves the fitness (Figure 3-20) [102]. The authors report that only two parameters require tuning, against three ($w$, $c_1$, $c_2$) for PSO [102]; the pseudocode given in the appendix of [102], however, uses a simplified update with a step size and a control factor that is not identical in form to the two-phase equations.

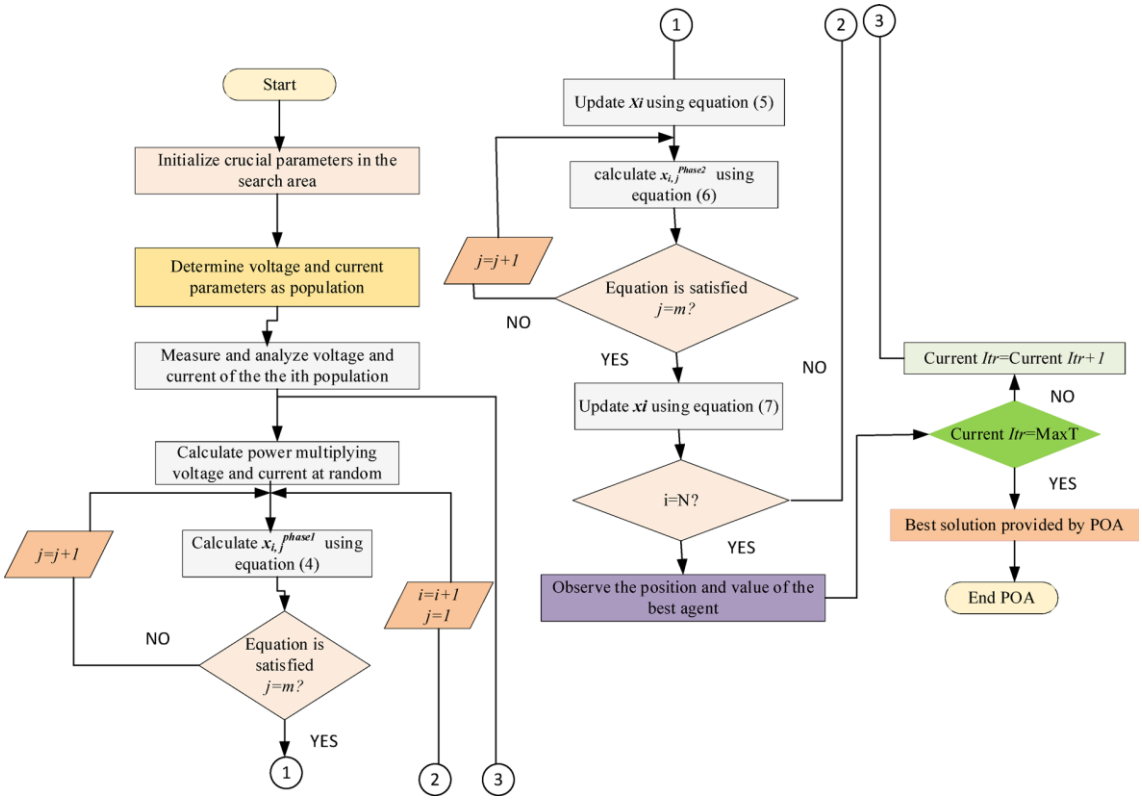



Figure 3-20: Flowchart of the Pelican Optimisation Algorithm (POA) applied to MPPT [102] (Fig. 5) under a CC BY 4.0 licence.

The converter (Figure 3-21) uses one switch, two inductors and a network of five diodes and four capacitors; its operating modes are analysed in [102] by volt-second balance, and its ideal gain allows a high step-up ratio at a moderate duty cycle (Example 2.4). The authors chose it because

it draws a continuous input current with low ripple, and contrast it with the SEPIC and Ćuk converters, whose input-current ripple they consider large enough to amplify the steady-state fluctuations near the MPP [102] - a judgement that differs from the continuous-input classification of Table 2-1 and shows that a continuous input current can still carry a ripple large enough to matter for tracking (Section 2.1.2).

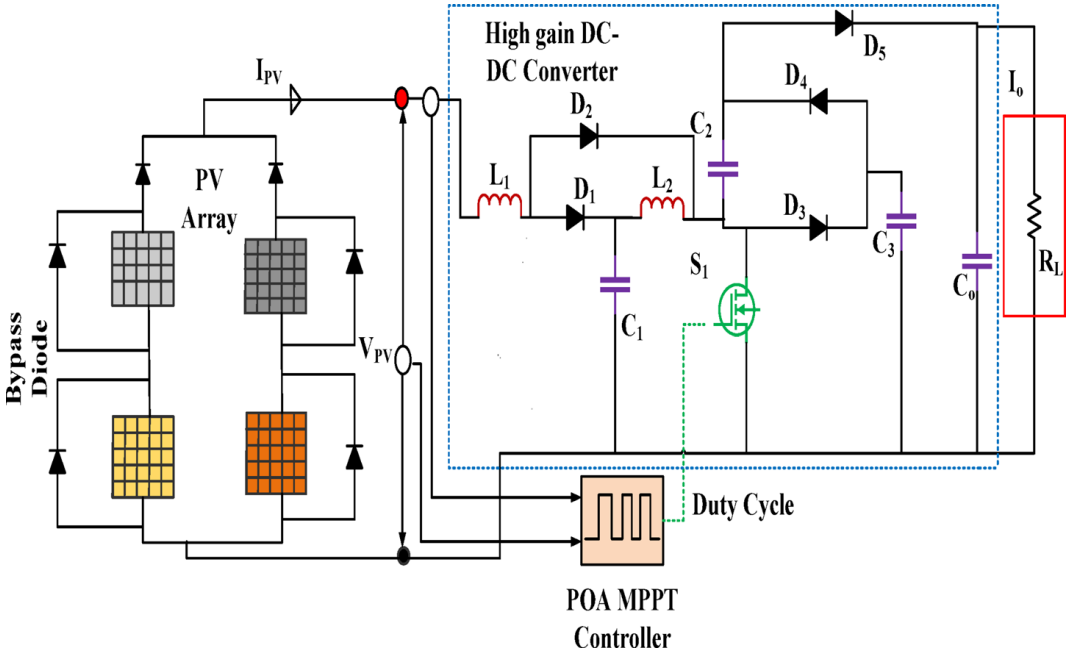



Figure 3-21: Stand-alone photovoltaic system of a partially shaded PV array with bypass diodes feeding a single-switch high-gain DC–DC converter whose duty cycle is set by the POA-based MPPT controller [102] (Fig. 6) under a CC BY 4.0 licence.

In MATLAB/Simulink, POA was benchmarked against P&O, PSO, cuckoo search (CS) and grey wolf optimisation (GWO) on a PV array of six 349.59 W modules (2095.54 W in total) under fixed and step-changing irradiance and temperature and under partial shading [102]. Table 3-7 transcribes the reported performance summary, and Example 3.4 derives the relative improvements. The authors report that POA tracked the MPP in about 0.2 s with no visible steady-state oscillation, whereas PSO needed about 600 ms for the initial tracking and GWO oscillated around the MPP at each irradiance level [102]. These narrative figures do not coincide with the tracking times of Table 3-7 (0.23 s for PSO), and the same paper also describes GWO as the slowest method (300–600 ms to reach a stable state), so the tabulated values are best read as indicative of the ranking rather than as precise measurements.

Table 3-7: Performance of the POA-based MPPT and of four benchmark algorithms on the high-gain converter (MATLAB/Simulink simulation; values transcribed from Table 4 of [102]).

| MPPT algorithm | Tracking time (s) | Tracking efficiency (%) | Fluctuation at transient | Steady-state oscillation (%) | Works under partial shading |
|---|---|---|---|---|---|
| P&O | 0.25 | 98 | High | 0.2 | No |
| PSO | 0.23 | 97.8 | Moderate | 0.005 | Yes |
| CS | 0.22 | 97.6 | Low | 0.00008 | Yes |
| GWO | 0.24 | 97.7 | High | 0.004 | Yes |
| POA (proposed in [102]) | 0.20 | 99 | Low | 0.00006 | Yes |

Experimental validation used four small PV panels in a 2S-2P arrangement, partially shaded by thin plastic sheets, a PIC16F-series microcontroller regulating the converter duty cycle, a resistive load and a digital storage oscilloscope (DSO) (Figure 3-22) [102]. For irradiance steps of 1000 → 800 → 600 W/m², the POA-controlled system settled in 82.2 ms and the PSO-controlled system in 99.2 ms, with output powers of 20, 18.01 and 11.95 W (POA) and 19.87, 17.84 and 11.77 W (PSO) at a constant 14.4 V (Figure 3-23) [102].

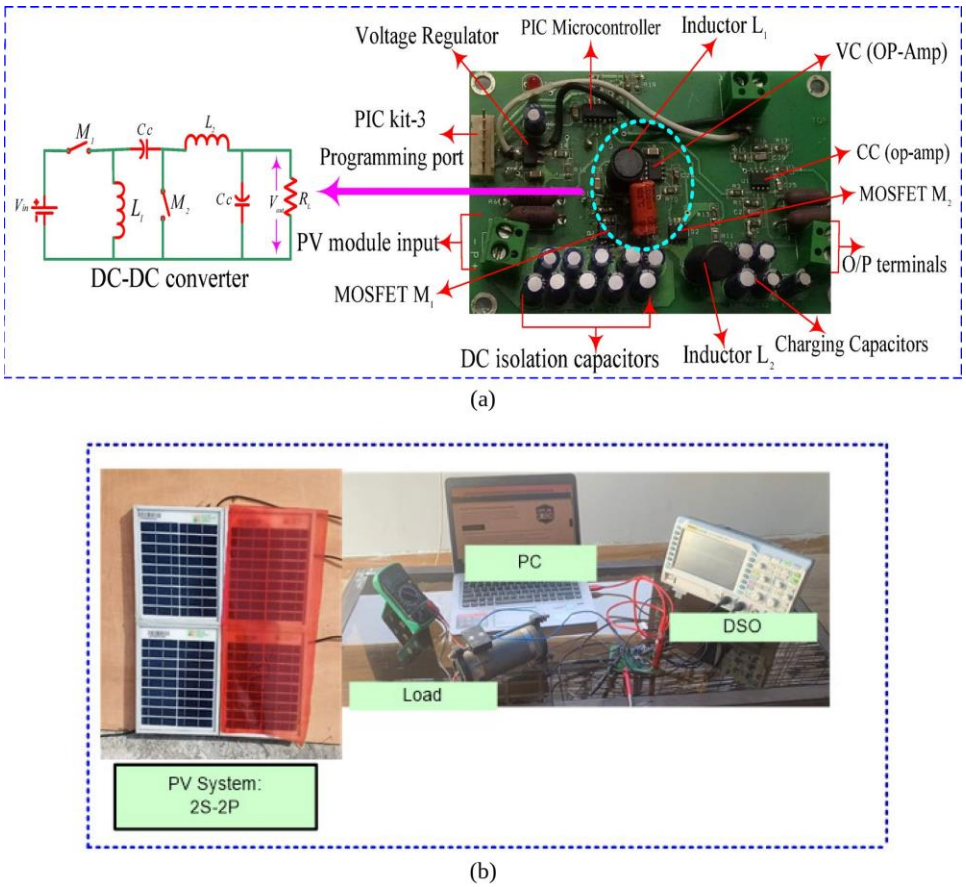



Figure 3-22: Experimental hardware used to validate the POA-based MPPT in (a) prototype board of the DC–DC converter and PIC-microcontroller-based MPPT controller, with the schematic of the converter; (b) laboratory set-up with the 2S-2P array of four PV panels (partial shading produced by a thin plastic sheet), resistive load, host PC and digital storage oscilloscope (DSO). Adapted from [102] (Figs. 13 and 14) under a CC BY 4.0 licence.

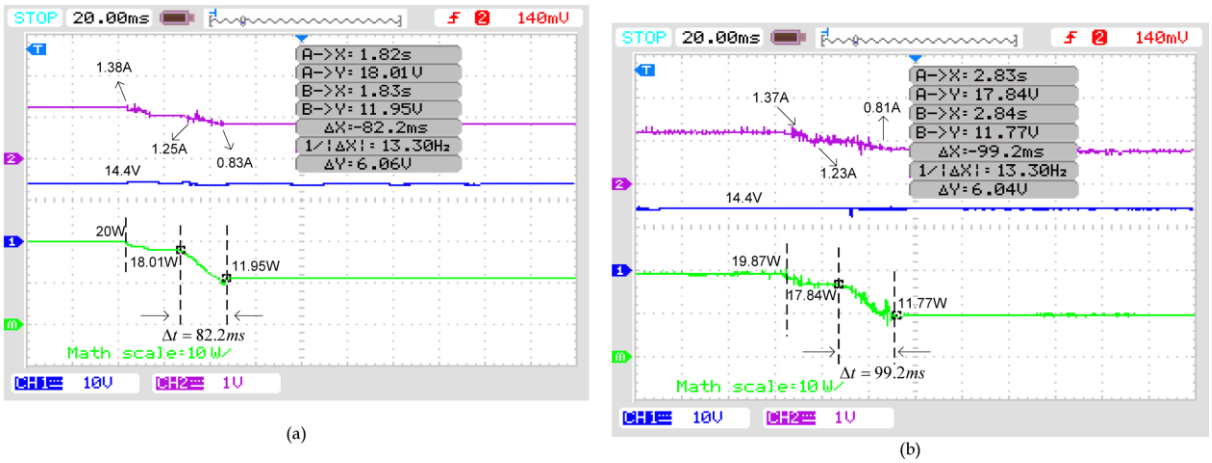



Figure 3-23: Measured transient response for irradiance steps of 1000 → 800 → 600 W/m² with (a) POA, settling in 82.2 ms, and (b) PSO, settling in 99.2 ms (oscilloscope traces of array voltage, current and computed power; math scale 10 W/div) [102] (Fig. 15) under a CC BY 4.0 licence.

**Example 3.4 - Relative improvements reported for POA [102]**

**Given data**

Table 3-7; measured settling times of 82.2 ms (POA) and 99.2 ms (PSO) and output powers after each irradiance step (Figure 3-23).

**Formula**

Relative reduction = $(x_{\mathrm{ref}} - x_{\mathrm{POA}})/x_{\mathrm{ref}}$

**Calculation**

| | |
|---|---|
| Tracking time: | (0.25 − 0.20)/0.25 = 20 % versus P&O; 13 % versus PSO, 9 % versus CS and 17 % versus GWO |
| Tracking efficiency: | 99 − 98 = 1.0 percentage point versus P&O (99/98 = 1.0102, i.e. 1.02 % relative); 1.2–1.4 points versus PSO, CS and GWO |
| Steady-state oscillation: | (0.00008 − 0.00006)/0.00008 = 25 % versus CS |
| Experiment: | (99.2 − 82.2)/99.2 = 17 % shorter settling; output power higher by 0.13, 0.17 and 0.18 W (0.7–1.5 %) at 1000, 800 and 600 W/m² |

**Result**

The 20 % (tracking time), 1.02 % (tracking efficiency) and 25 % (steady-state oscillation) figures coincide with those stated in the conclusion of [102].

**Interpretation:** in energy terms the advantage is modest: one percentage point of tracking efficiency on the 2095.54 W array corresponds to about 21 W, and a convergence faster by a few hundredths of a second matters only when irradiance steps are frequent. The steady-state advantage over P&O is the more consequential one: the 0.2% steady-state oscillation tabulated for P&O is of the same order as the oscillation losses computed in Example 3.1 for steps of 0.5–1 V, although the two quantities are defined differently.

**Source:** [102]

Three qualifications follow from the criteria of this thesis:

- the hardware converter is not the simulated one: the prototype schematic of Figure 3-22(a) and its description show a converter built around two n-channel MOSFETs and a coupling capacitor, not the single-switch topology of Figure 3-21 [102]; the experiment therefore validates the algorithm on a different actuator, and the high-gain converter results (for example the output voltage of about 432 V) are simulation-only;

- the comparison is algorithm-centred: all algorithms run on the same converter, so - as argued in Section 2.6 - the reported ranking is a property of the POA–converter pair rather than of POA alone, and the hardware comparison covers PSO only;
- the reported test system is not fully consistent: Table 1 of [102] describes the simulated array as three series modules × two parallel strings ($V_{MPP}$ = 129 V, $I_{MPP}$ = 16.26 A), whereas Fig. 2 of the same paper shows two series modules × three parallel strings with the MPP at 86 V; and the improvements over the benchmarks (about one percentage point in tracking efficiency and 0.02–0.05 s in tracking time) are small relative to these uncertainties.

POA is therefore best read as a promising, partially validated addition to the metaheuristic family of Section 3.3.3; the study does not support the conclusion that POA is the best, or the most recent, MPPT algorithm in general.

### 3.4.7 Computational Platforms Across the Surveyed Families

The computational burden surveyed family by family in this chapter maps onto a recognisable hierarchy of embedded hardware, and making this mapping explicit is useful for a designer working under a fixed hardware budget.

- The classical kernels of Section 3.2 and the constant-voltage/fractional methods run comfortably on eight-bit microcontrollers, and this is precisely why they remain the deployed mainstream in cost-sensitive products [25].
- Fuzzy-logic controllers occupy similar territory once the rule base is fixed, having been realised on low-cost boards [74], while the offline training required by neural and neuro-fuzzy methods is generally performed on a desktop or server and only the trained inference step - a small number of multiply–accumulate operations - needs to run on the embedded target.
- Population-based metaheuristics and their hybrids demand more: maintaining and updating several candidate solutions per iteration, together with the physical settling time each fitness evaluation requires (Section 3.1.3), typically pushes implementations toward 32-bit microcontrollers or digital signal processors.
- Model predictive control is the most demanding of the surveyed families in the finite-control-set form, since enumerating switch-state candidates within a single control period is a hard real-time computational task that commonly requires a digital signal processor or field-programmable gate array, particularly as converter order grows (Chapter 2); sliding-

mode control, by contrast, requires comparatively little online computation once the sliding surface is defined, and runs on standard microcontroller platforms.

- Deep-learning and reinforcement-learning methods sit at both ends simultaneously: cheap at inference once trained or converged, but dependent on a training phase that is computationally heavy and, for reinforcement learning, physically enacted on the hardware itself unless a simulated or digital-twin environment is available (a possibility returned to in Chapter 4).

This spread in computational requirement is, together with the shading environment of the intended installation, the second axis - alongside the condition-dependent performance discussed in Section 3.5 - on which a practical algorithm choice should be made.

## 3.5 Synthesis: MPPT Performance Under Key Operating Conditions

The chapter closes by reading the whole population of surveyed methods against the three conditions under which the families actually separate in practice: partial shading, dynamic irradiance, and measurement noise. Under partial shading, the separation is structural and near-absolute: every method of Section 3.2, however refined, satisfies its own local stopping criterion at whichever peak it happens to find, while the population-based and trained methods of Sections 3.3 and 3.4 are the ones demonstrated to capture the global peak reliably, at the shared cost of a physical search conducted through the converter [24, 69, 73]. Under dynamic irradiance, the ranking substantially inverts: fast, change-aware classical kernels and control-theoretic methods with consistent large-signal dynamics perform strongly, while population methods are at their weakest between convergences, since a converged swarm is blind to a new disturbance until an explicit re-search trigger fires [46, 61, 73, 96]. Under measurement noise, every perturbation-based method, classical or intelligent, is bounded by the same mechanism: the useful perturbation step must produce a power difference larger than the converter's own ripple and sensor noise, or the comparison on which the algorithm's decision rests carries no information; a dedicated analysis of this trade-off derives the resulting optimum jointly for step size and sampling rate and verifies it by both simulation and hardware experiment [50].

Table 3-8 condenses this condition-by-condition reading into a single method-level reference view spanning every method surveyed in the chapter, from the classical kernels of Section 3.2 through the most recent control-theoretic and learning methods of Section 3.4, and adds the quantitative indicators reported in the sources, each with its conditions. Only one comparison in it rests on a

common basis: in the benchmark of [102], run on a single converter under the same simulated conditions, the five algorithms span 0.20–0.25 s in tracking time and 97.6–99 % in tracking efficiency, while their steady-state oscillation spans more than three orders of magnitude, from 0.2 % for P&O to 0.00006 % for POA. The computed examples of this chapter add two further reference points: the oscillation loss of P&O grows from 0.12 % to 2.0 % as the step rises from 0.5 V to 2 V (Example 3.1), and a fractional method with a mid-range $k_1$ forgoes 3.5–7.2 % of the available power (Example 3.2).

No single family occupies the top row under all three conditions simultaneously, and the families that are strongest under partial shading (metaheuristic, hybrid) are generally not the same families that are strongest under fast dynamics or noise (enhanced classical, sliding-mode, model predictive control) taken alone. This is the technical basis for the hybrid design pattern of Section 3.4.1, and it is also the reason the comparative discussion of Chapter 4 treats algorithm selection as a condition-dependent decision rather than seeking a single best answer.

Three conclusions: First, a reported tracking figure is never a property of an algorithm alone: every verdict is conditional on the specific shading pattern, irradiance profile and converter used to obtain it. Second, the field's three headline performance criteria, speed, oscillation, and noise tolerance, are not three independent axes but effectively one three-way constraint, whose coefficients are set by the converter rather than chosen freely by the algorithm designer. Third, and most consistently across every family, algorithmic sophistication is not free: what a more advanced method buys - global reach, learned nonlinearity handling, model-based anticipation, or invariance to the plant - is bought at a specific, identifiable cost in sensing, computation, tuning or training effort, and the appropriate choice of algorithm is accordingly a function of the application's shading environment, cost target and computational budget rather than a single best answer.

Table 3-8: Method-level summary of the MPPT methods surveyed in this chapter, grouped by family, with the quantitative indicators reported in the sources; all verdicts are conditional on the shading pattern, irradiance profile and converter of the underlying studies.

| Method | Sensors | Global under shading | Tracking time | Tracking efficiency (%) | Steady-state oscillation | Ref. |
|---|---|---|---|---|---|---|
| ***Classical and fractional (Section 3.2)*** | | | | | | |
| P&O, fixed step | v, i | No | 0.25 s[a] | 98[a]; 92–98[d] | 0.2 %[a]; loss 0.12 / 0.49 / 2.0 % at $\Delta V$ = 0.5 / 1 / 2 V[b] | [23, 24, 61] [101, 102] |
| P&O, variable step / self-predictive | v, i | No | n/r | n/r | Near zero once held | [40, 41, 46, 64] |
| Incremental Conductance | v, i | No | n/r | 90–97[d]; 88.6–98.1[e] | 0.2–1.6 %[d] | [17, 51, 64, 68-70] [100, 101] |
| Constant voltage / current | v or i | No | — (no search) | n/r | None | [64-66, 71] |
| Fractional (FOCV / FSCC) | v or i, plus switch | No | n/r | 98.5–100 ($k_1$ = 0.82); 92.8–96.5 ($k_1$ = 0.76)[c] | Low; systematic bias | [43, 64, 66, 69, 72, 73] |
| ***Intelligent (Sections 3.3.1–3.3.2)*** | | | | | | |
| Fuzzy logic (Mamdani / Takagi–Sugeno) | v, i | Only if tuned for it | n/r | n/r | Quieter than classical kernels | [64, 65, 74, 75] |
| Artificial neural network | G, T (or v, i) | Only if trained for it | n/r | ≈ 98[g] | Reduced | [65, 86] |
| Neuro-fuzzy (ANFIS) | G, T, v | Only if trained for it | n/r | n/r (outperformed PI on the same hardware) | n/r | [76] |
| ***Metaheuristic (Section 3.3.3); rows marked a share one converter and one set of conditions*** | | | | | | |
| Particle swarm optimisation | v, i | Yes | 0.23 s[a]; 99.2 ms[f] | 97.8[a] | 0.005 %[a] | [73] [102] |
| Grey wolf optimisation | v, i | Yes | 0.24 s[a] | 97.7[a] | 0.004 %[a] | [64] [102] |
| Cuckoo search | v, i | Yes | 0.22 s[a] | 97.6[a] | 0.00008 %[a] | [80] [102] |
| Pelican optimisation (POA) | v, i | Yes | 0.20 s[a]; 82.2 ms[f] | 99[a] | 0.00006 %[a] | [102] |
| Genetic algorithm | v, i | Yes, in principle | Slowest of the class | n/r | n/r | [78] |
| Ant colony optimisation | v, i | Yes | n/r | n/r | n/r | [79] |
| Bat / firefly algorithms | v, i | Yes (dedicated studies) | n/r | n/r | n/r | [77, 80-82] |
| Golden-section search | v, i | Reported (dedicated adaptation) | Few, predictable evaluations | Below an adaptive fuzzy–P&O hybrid (static) | n/r | [83] |
| ***Most recent (Section 3.4)*** | | | | | | |
| Hybrid (global + local) | v, i | Yes, via the global stage | n/r | 99.5 uniform; 83–99 under shading[h] | As the local stage | [63] [16, 64, 69, 72, 84] |
| Machine / deep learning | v, i (sensorless) or G, T | If trained on shaded data | n/r | ≈ 98[g]; voltage error 0.47 %[j] | Reduced | [65, 86, 87] |
| Reinforcement learning | v, i | Possible; evidence mixed | n/r | < 1 % deviation claimed[i] | n/r | [37, 65, 88-90] |
| Model predictive control | v, $i_L$ | Not inherent | Faster than baseline in transients | n/r | n/r | [91-95] |
| Sliding-mode control | v, i | Not inherent | n/r | n/r | Chattering unless mitigated | [96-98] |

Table 3-8 (continued): behaviour under dynamic irradiance and noise, cost, typical role and main limitation of each method; sources as above.

| Method | Dynamic irradiance; noise | Cost: computation; tuning | Typical role | Main limitation |
|---|---|---|---|---|
| ***Classical and fractional (Section 3.2)*** | | | | |
| P&O, fixed step | Drift risk; step-versus-noise trade-off | Very low; one parameter (step) | Default low-cost tracker | Speed–oscillation trade-off |
| P&O, variable step / self-predictive | Enhanced variants perform well; noise-referenced hold | Low; thresholds against the noise floor | Improved classical tracker | Threshold setting |
| Incremental Conductance | Tolerance band ε mitigates noise | Low–moderate; band ε | Classical tracker | Ranking against P&O reverses between studies |
| Constant voltage / current | Poor dynamics; robust but biased | Very low; one sensor | Very low-cost systems | Fixed reference misses the MPP |
| Fractional (FOCV / FSCC) | Periodic recalibration; harvest lost while sampling | Low; $k_1$, $k_2$ per module | Start-up or coarse stage of hybrids | Optimal k drifts with irradiance |
| ***Intelligent (Sections 3.3.1–3.3.2)*** | | | | |
| Fuzzy logic (Mamdani / Takagi–Sugeno) | Good once tuned; graded decisions | Low online (lower for Takagi–Sugeno); high design effort | Microcontroller-level trackers | Tuning tied to the converter |
| Artificial neural network | Good if training data are representative | Low inference; offline training | Reference generator | Data dependence; ageing drift |
| Neuro-fuzzy (ANFIS) | As ANN; fuzzy layer absorbs ripple | Highest: training plus rule design | Co-selected with an interleaved boost | Two design burdens |
| ***Metaheuristic (Section 3.3.3); rows marked a share one converter and one set of conditions*** | | | | |
| Particle swarm optimisation | Weak between convergences; needs a re-search trigger | Population × settling time; w, $c_1$, $c_2$ | Global tracker under shading | Tuning; premature convergence |
| Grey wolf optimisation | High transient fluctuation[a] | Fewer free parameters | Global stage of hybrids | Slow to settle in [102] |
| Cuckoo search | Low transient fluctuation[a] | Class-typical | Shaded-service tracker | Class-typical costs |
| Pelican optimisation (POA) | Low transient fluctuation[a] | Two parameters | Stand-alone ≈ 2 kW array | One study; internal inconsistencies |
| Genetic algorithm | Disruptive search phases | A full generation per step | Offline tuning of other controllers | Too slow for online tracking |
| Ant colony optimisation | Fewer iterations than PSO | Iteration-hungry | Large, heavily shaded arrays | Mostly simulation evidence |
| Bat / firefly algorithms | Class-typical | Class-typical | Dedicated shaded trackers | Class-typical costs |
| Golden-section search | Deterministic | Low; no stochastic parameters | Low-cost quasi-global search | Bracket must contain the peak |
| ***Most recent (Section 3.4)*** | | | | |
| Hybrid (global + local) | Good after handover | Low–moderate | Default compromise under shading | Supervisor thresholds |
| Machine / deep learning | Good if training data are representative | Low inference; high training | Sensorless trackers | Data dependence; evidence base |
| Reinforcement learning | Potentially strong; non-stationary training | High during training | Research stage | Exploration is physical |
| Model predictive control | Very good (anticipation) | High; DSP or FPGA | Constrained, high-performance stages | Needs a valid model (CCM/DCM) |
| Sliding-mode control | Very good (large-signal consistency) | Low–moderate | Robust tracking without a converter model | Chattering |

n/r: not reported in the surveyed sources. Values are quoted with their conditions and, except within the rows marked a, are not comparable across studies: [a] benchmark on one high-gain converter under the same simulated conditions, values indicative (Example 3.4) [102]; [b] computed in this thesis, Example 3.1; [c] computed in this thesis under uniform irradiance of 200–1000 W/m$^2$, Example 3.2; [d] simulation over five converters, efficiency metric not defined [101]; [e] converter efficiency $P_{out}/P_{in}$, not tracking efficiency [100]; [f] experimental settling time after irradiance steps [102]; [g] review average under uniform conditions [86]; [h] hybrid PSO–P&O on a SEPIC converter [63]; [i] methodology later rebutted [89, 90]; [j] predicted voltage against a simulated curve, no converter in the loop [87]. A directly connected resistive load forfeits about 37 % of the available power (Chapter 1).

# 4 CHAPTER 4 - COMPARATIVE ANALYSIS, DISCUSSION AND CONCLUSIONS

Chapters 2 and 3 surveyed, in turn, the DC–DC converter topologies used in photovoltaic power conditioning and the Maximum Power Point Tracking (MPPT) algorithms reported in the literature to control them. This closing chapter draws the two surveys together. Section 4.1 compares the MPPT algorithm families against the performance criteria established in Chapter 3. Section 4.2 briefly revisits the converter topologies of Chapter 2 specifically as MPPT actuators, connecting converter choice to algorithm performance. Section 4.3 discusses critically what the assembled evidence does and does not establish. Section 4.4 sets out the future directions the recent literature itself points toward. Section 4.5 concludes.

## 4.1 Comparative Analysis of MPPT Algorithms

Table 4-1 collects, in a single view, the qualitative comparison that Chapter 3 built up family by family. Because the underlying literature does not report every quantity for every method under common test conditions, the comparison is deliberately qualitative and conditional rather than a numerical ranking - a discipline consistent with the finding, developed throughout Chapter 3 and returned to in Section 4.3, that reported numerical figures are only comparable when the test conditions, converter and profile that produced them are also compared. Because the full comparison spans seven algorithm families, it is presented as two linked tables for readability: Table 4-1 covers the classical and intelligent tiers, and

Table 4-2 covers the metaheuristic, hybrid and most recent (ML/DL/RL, MPC/SMC) tiers.

Table 4-1: Comparative overview of the classical and intelligent MPPT tiers against the performance criteria of Chapter 3. For detailed per-method evidence and references, see Table 3-1 (Conventional, Constant V/I) and Table 3-3 (Intelligent).

| Criterion | Conventional (P&O, INC) | Constant V/I, fractional | Intelligent (fuzzy, ANN) |
|---|---|---|---|
| Tracking speed | Moderate; tunable via step size | Fast (no search) but inaccurate | Fast once tuned/trained |
| Steady-state accuracy | Residual oscillation, tunable | Systematic bias | Good |
| Global search (partial shading) | No | No | Only if trained for it |
| Dynamic response (irradiance steps) | Good with enhancements; drift risk | Poor | Good |
| Computational complexity | Very low | Very low | Low–moderate |
| Sensing requirements | *V*, *I* | *V* or *I* | *V*, *I* |
| Robustness to noise | Bounded by step-vs-noise trade-off | High (no search) | Good (graded decisions) |
| Implementation / tuning cost | Low | Very low | Moderate (design effort) |
| Real-time suitability on low-cost hardware | Excellent | Excellent | Good |

Table 4-2: Comparative overview of the metaheuristic, hybrid and most recent MPPT tiers against the performance criteria of Chapter 3. For detailed per-method evidence and references, see Table 3-4 (Metaheuristic), Table 3-6 (Hybrid, ML/DL/RL, MPC/SMC), and Table 3-5 (MPC vs. SMC in detail).

| Criterion | Metaheuristic (PSO, GWO, GA, …) | Hybrid | ML / DL / RL | MPC / SMC |
|---|---|---|---|---|
| Tracking speed | Slower - population settling dominates | Fast after handover | Fast at inference; slow to train | Fast (anticipatory) |
| Steady-state accuracy | Very good once converged | Very good | Good if well trained | Very good |
| Global search (partial shading) | Yes | Yes (via global stage) | Possible, evidence mixed | Not inherent; depends on search layer |
| Dynamic response (irradiance steps) | Weak between convergences | Good | Good if trained on transients | Very good |
| Computational complexity | Moderate–high | Moderate | Moderate (inference) – high (training) | High |
| Sensing requirements | *V*, *I* | *V*, *I* | *V*, *I* (sensorless variants) | *V*, *I*, model parameters |
| Robustness to noise | Good once converged | Good | Depends on training data | Good (SMC); model-sensitive (MPC) |
| Implementation / tuning cost | Moderate–high (tuning + physical search) | Moderate–high | High (data, training) | High (model, computation) |
| Real-time suitability on low-cost hardware | Limited | Good | Limited (deep variants) | Limited (needs DSP/FPGA) |

Three observations follow directly from Table 4-1 and

Table 4-2 and organise the discussion in Section 4.3. First, no single family dominates on every criterion - the trade-off between global-search capability and implementation cost is essentially monotonic across the two tables, from the cheapest and narrowest (constant-voltage) to the most capable and most demanding (MPC, RL). Second, the criterion that separates families most sharply is not steady-state accuracy, on which several families now perform comparably well, but global search capability under partial shading, which remains structurally unavailable to the purely local methods regardless of how thoroughly they are refined. Third, computational and sensing cost scale, broadly, with the sophistication needed to secure that global-search capability, so the appropriate choice is a function of the deployment's shading risk and hardware budget rather than a single best algorithm.

Where studies report numerical results under stated conditions, these are collected with their test conditions in Table 3-7 (metaheuristic algorithms on one converter [102]) and Table 4-5 (conventional algorithms on several converters [100, 101]), and Examples 3.1–3.4 derive quantitative comparisons from them. Because each set of numbers was obtained with its own module, converter, load and irradiance profile, the numbers are compared within studies only, never across them.

## 4.2 Converter Topology and MPPT Implementation

Chapter 2 established that the converter is not a neutral, interchangeable actuator: its gain law, its conduction-mode boundary, its input-ripple noise floor and its dynamics all condition what any MPPT algorithm can achieve through it. This connection is not merely theoretical. Studies that vary the converter deliberately while holding the tracking algorithm fixed report that settling time and steady-state efficiency differ for every converter–algorithm pairing tested, with no single combination best on every criterion [47]; a comparable study pairing hybrid metaheuristic algorithms with different converter families reports that the ranking of algorithms changes according to which converter they are implemented on, with one particular converter–algorithm pairing achieving markedly higher tracking efficiency under shading than the same algorithms implemented on other converters [63]. Table 4-3 summarises the qualitative link between converter family and MPPT suitability established in Chapter 2.

Table 4-3: Qualitative link between converter family and MPPT implementation (see Table 2-5. [47, 63]).

| Converter family | Tracking range | Dynamic behaviour as an actuator | Best-suited MPPT role |
|---|---|---|---|
| Boost | Bounded at low irradiance | Best-behaved of the classical set - simple, well-damped | Default two-stage front end; classical or enhanced-classical kernels |
| Buck | Bounded at high load resistance | More elaborate, lightly damped | Only where bus voltage is reliably below array voltage |
| Buck–boost / Ćuk / SEPIC / Zeta | Unbounded (full I–V range) | Higher order (fourth-order dynamics) | Preferred class for wide-range tracking; chargers, stand-alone systems |
| High-gain non-isolated | Depends on realisation; duty-headroom must be verified | Actuation law steepened/compounded by design; conduction-mode structure often richer | Module-level and large-ratio architectures; dynamic models rarely published |
| Isolated (flyback, bridge) | Extended via turns ratio | Leakage inductance adds dynamics unless actively clamped | Microinverters; isolation-mandated installations |

The practical implication for a designer selecting a converter–algorithm combination is that the two choices cannot be made independently: a converter chosen purely on power-processing criteria (efficiency, cost, component count) may present a plant that is poorly matched to the intended algorithm's assumptions - an actuation law with too little duty-cycle headroom, a conduction-mode boundary crossed routinely at the irradiance levels the installation will actually see, or a settling time that forces an unacceptably slow sampling interval. This is, in essence, the central critical conclusion of the present thesis, developed from the converter side in Chapter 2 and from the algorithm side in Chapter 3: the converter and the tracking algorithm should be regarded, and where possible selected, as a single co-designed system rather than as two independently optimised components.

A joint design procedure follows directly from the criteria assembled in Chapters 2 and 3, and Table 4-4 sets it out as seven ordered steps. Every step crosses the boundary between the two literatures surveyed in this thesis at least once, which is precisely why no single converter-only or algorithm-only survey states the procedure in full.

Table 4-4: Joint converter–algorithm design procedure assembled from the criteria of Chapters 2 and 3.

| Step | Decision | Governed by |
|---|---|---|
| 1 | Fix the system architecture and required voltage-gain window | Section 1.6 (granularity), Section 1.5 (temperature/irradiance corridor) |
| 2 | Select the converter topology and, where possible, obtain its dynamic model | Chapter 2 selection criteria (Table 2-4), including the seven MPPT-facing criteria |
| 3 | Choose the control structure (direct duty-cycle or reference-based) and the regulated port | Right-half-plane-zero and dynamics considerations (Section 2.5.2) |
| 4 | Set the inner-loop bandwidth, if a reference-based structure is used | Converter settling dynamics; switching frequency |
| 5 | Compute the MPPT sampling interval from the actuator's settling behaviour | Equation (2.9), evaluated across the operating window, not only at rated conditions |
| 6 | Set the perturbation amplitude (or equivalent parameter) against the converter's ripple floor | Section 3.1.2; equations (2.8)–(2.9) |
| 7 | Validate across the full operating window, including conduction-mode crossings | Section 2.1.2; Section 3.5 |

Two further studies, both simulation-based, reach the same conclusion for the conventional algorithms and provide numbers that make the point quantitative (Table 4-5). Raj et al. [100] tested P&O and INC on conventional and ZVS versions of the Zeta and SEPIC converters at 1000 W/m² and 25 °C: INC raised the converter efficiency on three of the four converters, by 5.2 to 8.4 percentage points, but lowered it by 1.6 points on the ZVS SEPIC. Soriano et al. [101] tested the same two algorithms on the buck, boost, buck–boost, Ćuk and SEPIC converters under irradiance and temperature steps and found the opposite ordering - P&O equal to or more efficient than INC on all five converters - together with a lower tracking oscillation for INC on the buck–boost, Ćuk and SEPIC converters. Read together with [47] and [63], these results confirm that even the ranking of the two simplest algorithms depends on the converter, and on the study, in which it is measured.

Table 4-5: Quantitative results of the two studies in which converter and conventional MPPT algorithm are varied jointly [100, 101].

| Converter | Algorithm | $P_{in}$ (W) | $P_{out}$ (W) | Losses (W) | Efficiency (%) |
|---|---|---|---|---|---|
| ***(a) Raj et al. [100]: MATLAB simulation, 1000 W/m², 25 °C, single PV panel with nominal operating point 17 V, 0.58 A (Appendix A of [100]), maximum available power not reported; 60 Ω load, $f_s$ = 5 kHz*** | | | | | |
| Zeta | P&O | 10.01 | 8.78 | 1.23 | 87.71 |
| ZVS Zeta | P&O | 10.01 | 8.977 | 1.157 * | 89.68 |
| SEPIC | P&O | 9.796 | 8.169 | 1.626 | 83.39 |
| ZVS SEPIC | P&O | 10.13 | 9.181 | 0.95 | 90.62 |
| Zeta | INC | 9.2276 | 8.672 | 0.555 | 93.98 |
| ZVS Zeta | INC | 9.2276 | 9.055 | 0.1726 | 98.12 |
| SEPIC | INC | 9.97 | 8.832 | 1.1372 | 88.59 |
| ZVS SEPIC | INC | 9.97 | 8.864 | 1.106 | 89.00 * |
| ***(b) Soriano et al. [101]: simulation, ST090P(36) panel with $P_{max}$ = 85 W at $V_{mp}$ = 17.6 V, $I_{mp}$ = 5.11 A (STC), irradiance and temperature steps (Fig. 3 of [101]); efficiency metric not defined in [101]*** | | | | | |
| **Converter** | **Components** | **Efficiency P&O (%)** | **Efficiency INC (%)** | **Oscillation P&O (%)** | **Oscillation INC (%)** |
| Buck | 5 | 98 | 96 | 0.2 | 0.2 |
| Boost | 5 | 98 | 97 | 0.3 | 0.4 |
| Buck–boost | 5 | 92 | 90 | 1.2 | 0.9 |
| Ćuk | 7 | 95 | 94 | 1.8 | 1.6 |
| SEPIC | 7 | 97 | 90 | 2.1 | 0.7 |

** As reported in [100]; recomputed from $P_{in} - P_{out}$, the losses are 1.033 W (ZVS Zeta, P&O) and the efficiency is 88.91% (ZVS SEPIC, INC). Efficiency in (a) is the converter efficiency $P_{out}/P_{in}$, not the tracking efficiency of equation (3.1); neither study reports the maximum available power under its test conditions, so the tracking efficiency cannot be computed for either.*

## 4.3 Critical Discussion

### 4.3.1 Which approaches perform well, and under what conditions

The evidence surveyed in Chapters 2 and 3 supports a condition-dependent rather than a universal answer to the question of which MPPT method is "best." Under uniform or slowly varying irradiance, on a well-matched converter, an enhanced classical kernel (variable-step or self-predictive P&O, tolerance-banded INC) delivers fast transient response together with near-zero steady-state oscillation at very low implementation cost, and the evidence reviewed in Section 3.2 gives no reason to prefer a more elaborate technique in this regime [41, 46]. Under partial shading, this changes qualitatively rather than incrementally: no refinement of a local method changes its inability to distinguish a local peak from the global one, so a genuinely global capability - metaheuristic search, a trained global predictor, or a hybrid combining a global stage with a fast local one - is required if the installation's shading environment makes multiple peaks likely [23, 24, 73, 77]. Under fast-changing irradiance, fast, change-aware classical and control-theoretic methods (drift-aware P&O variants, sliding-mode control, model predictive control) perform strongly, while a population-based global method is at its weakest between convergences, since it must first detect that the environment has changed before it searches again [40, 61, 73, 96].

### 4.3.2 Limitations of conventional methods and the value added by advanced methods

The principal, well-documented limitation of the conventional family is the coupling between perturbation amplitude and the speed–oscillation trade-off, compounded by vulnerability to drift under fast irradiance transients and structural inability to guarantee global convergence under partial shading (Section 3.2.5). The advanced and intelligent methods of Section 3.3 address the first two limitations substantially (fuzzy and neural controllers handle the array's nonlinearity without an explicit model and without a fixed step-size compromise) and the third limitation only through population-based or trained-global variants specifically designed for it. The methods of Section 3.4 extend this picture further: hybrid architectures make the field's practical answer to the shading problem explicit (spend a global search only where needed); model predictive control and sliding-mode control bring the converter's own behaviour into the control law itself, at the price of a model dependency (MPC) or switching-induced ripple (SMC); and the learning-based methods offer, in principle, pair-specific adaptation at the price of data, training cost, and - as the discussion of a formally rebutted deep-reinforcement-learning result in Section 3.4.3 illustrates - an evidence base that is not yet uniformly mature [89, 90].

### 4.3.3 Trade-offs between performance and computational complexity

Table 4-1 and Table 4-2 make the trade-off explicit: global-search capability, model-based anticipation, and learned adaptation are each purchased at an identifiable cost in sensing, tuning effort, training data, or online computation. For low-cost, well-conditioned installations—small residential or commercial systems with limited shading risk—the additional capability of the advanced families is frequently not worth its cost, and the review literature's own comparative studies support fielding an enhanced classical kernel on a well-matched converter. For large or heavily shaded arrays, where the mismatch penalty of Chapter 1 is largest, the additional cost of a global or hybrid method is more easily justified by the energy it recovers. This is not a deficiency of the literature but a genuine engineering trade-off that the comparative evidence assembled in this thesis makes explicit rather than resolves into a single recommendation.

### 4.3.4 Suitability for practical applications

Read jointly, Chapters 2 to 4 suggest the following practical guidance, stated as a condition-dependent recommendation rather than a ranking:

- Where the installation is a single string or module under a largely uniform irradiance profile and cost is the binding constraint, an enhanced classical kernel (variable-step P&O or

tolerance-banded INC) on a boost or SEPIC/Ćuk converter, chosen according to the required tracking range (Table 4-3), remains a well-supported, low-cost choice.

- Where partial shading is a realistic operating condition, building-integrated arrays, arrays overshadowed by vegetation or adjacent structures, or large arrays with unavoidable module-to-module mismatch, a hybrid architecture combining a global stage (metaheuristic or trained predictor) with a fast local kernel is the combination best supported by the reviewed evidence.
- Where the application can support the computational and sensing cost, model predictive control offers the most direct route to jointly optimising tracking accuracy against converter constraints (current limits, switching effort), and sliding-mode control offers the most robust behaviour across a wide operating range with the least dependence on an accurate converter model.
- Reinforcement-learning and deep-learning approaches are, on the reviewed evidence, promising but not yet the safest default for unsupervised field deployment, given the physical cost of exploration, the data-dependence of trained mappings, and the documented case in which a prominent published result did not survive independent scrutiny.

### 4.3.5 Unresolved challenges

Three challenges recur across the literature surveyed in this thesis and remain, on the evidence available, unresolved. First, benchmarking heterogeneity: shading patterns, irradiance profiles and performance metrics are chosen individually by the authors of each study, so reported figures aggregate poorly between papers, and the apparently conflicting verdicts of different comparative studies typically resolve once the test conditions behind each verdict are made explicit - a discipline the present thesis has tried to observe throughout, but one the primary literature does not consistently apply to itself [65, 77]. Second, the scarcity of joint converter–algorithm evaluation: the great majority of MPPT studies test several algorithms on a single, usually conventional, converter, or test several converters under a single algorithm, but studies that vary both deliberately - of the kind reviewed in Section 4.2 [47, 63], [100, 101] - remain a small minority, so the literature's own evidence base is least developed precisely where Chapter 2 and this chapter argue it matters most. Third, validation maturity: a substantial share of the advanced and recent methods surveyed in Sections 3.3 and 3.4 are validated in simulation only, and the comparative reviews cited throughout this thesis consistently identify the shortage of long-duration hardware and field validation as a limitation on the strength of the conclusions the literature can

support [32, 65, 77]. Even where hardware validation is reported, the tested converter may differ from the simulated one, as in the recent case study of Section 3.4.6 [102].

### 4.3.6 Evidence Quality in the Most Recent Literature

Because this thesis gives particular weight to the most recent MPPT techniques (Section 3.4), the quality of the evidence behind those specific techniques deserves a dedicated, and more cautious, comment.

Two patterns recur:

- The first is a published-model dependency: the model-predictive and, increasingly, the learning-augmented control methods surveyed in Sections 3.4.3 and 3.4.4 are only as trustworthy, and only as reproducible, as the converter model on which they are built or trained, and Chapter 2 already established that the topology literature proposing new high-gain converters only inconsistently publishes that model;
- The second is a documented instance of a claim not surviving scrutiny: the deep-reinforcement-learning result discussed in Section 3.4.3, in which a widely cited claim of near-perfect tracking accuracy under partial shading was subsequently shown, in a formal published comment, to rest on an approximate model and a technique that in fact converged to the first peak encountered rather than to the global one [89, 90]. This episode is not evidence that reinforcement learning is unsuited to MPPT - the same family also includes the converter-control literature's strongest, formally-verified results [37] - but it is a concrete, citable illustration of why this thesis treats reported figures for the most recent methods with the same demand for stated test conditions that it applies to the classical literature, rather than extending them a presumption of maturity merely because they are recent.

The POA case study of Section 3.4.6 offers a second, more ordinary illustration: its headline improvements over established metaheuristics are small - about one percentage point in tracking efficiency and a few hundredths of a second in tracking time - relative to the internal inconsistencies of its reported test system, and its hardware experiment uses a different converter from its simulations [102]. None of this invalidates the study, but it shows why recent results are best read as indicative until they are reproduced under declared, common conditions.

### 4.3.7 Answering the Thesis Objective

Read against the three specific aims stated in Section 1.8, the review conducted in this thesis supports the following direct answers. The converter topologies most relevant to photovoltaic power conditioning are, for gain-matched applications, the buck–boost-derived family, and for large step-up ratios, the coupled-inductor and voltage-multiplier branches of the non-isolated high-gain family (Chapter 2); no converter is universally best, and the applicable choice is fixed by the required gain, the isolation requirement and the power level. The MPPT algorithms most active in the recent literature are the hybrid, learning-based, model-predictive and sliding-mode families surveyed in Section 3.4, each addressing a specific weakness of the classical and intelligent methods that precede it, at an identifiable and, in this thesis's reading, unavoidable cost in sensing, computation or training effort (Chapter 3). And bringing the two literatures into a single frame (Sections 4.1–4.3) shows that the trade-offs between converter-level and controller-level properties are real, quantifiable where the evidence exists, and currently under-explored where it matters most - the joint evaluation of specific converter–algorithm pairs.

## 4.4 Future Perspectives

The literature reviewed in this thesis points to three directions along which the field is currently developing, each discussed here only to the extent it is supported by the reviewed sources.

**Artificial-intelligence-enabled tracking** continues to move from shallow, sensor-based neural mappings toward deeper, sequence-aware and attention-based architectures, and toward sensorless formulations that infer the array's behaviour from terminal electrical measurements alone rather than from dedicated irradiance and temperature sensors [65, 86, 87]. The clearest emerging practical pattern is not the wholesale replacement of classical control but its augmentation: a learned component supplies a fast, informed estimate (of the MPP location, or of otherwise unmodelled converter dynamics), while a conventional control law - a classical kernel, or a model-predictive or sliding-mode regulator - supplies the robustness and, where formally analysed, the stability guarantees that a learned policy alone does not yet reliably provide [37, 65]. Three prerequisites recur in the literature as conditions for large-scale deployment of this trend: explainability sufficient to support formal stability arguments, robustness to the sensor noise that the comparative literature already under-reports (Section 3.5), and transferability across converter topologies and climates - the last of these being, in the terms of this thesis, the pair-dependence of Chapters 2 and 3 restated as an explicit deployment requirement.

**Connected monitoring and simulation infrastructure**, of which the digital twin is the most developed instance, offers a route to a specific and identified gap in the literature: the shortage of joint, factorial converter–algorithm evaluation under common, declared conditions (Section 4.3.5). A digital twin, a simulation model kept in bidirectional correspondence with a physical converter and array through connected instrumentation, is, in principle, well suited both to fault diagnosis (comparing predicted and measured behaviour to localise a fault to the array, the converter, or the sensing chain) and to serving as a training environment for a reinforcement-learning tracker, moving the physical exploration cost identified in Section 3.4.3 into a simulated setting.

This capability is, however, gated by exactly the modelling gap Chapter 2 identified: a converter's digital twin requires a validated dynamic model of that converter, which the high-gain topology literature only inconsistently publishes, and - as of the literature surveyed in this thesis - no standard protocol or platform yet exists for applying the concept at scale in photovoltaic installations.

Of the three trends discussed in this section, the digital twin is arguably the one best matched to the field's most consequential gap, precisely because it is not a new algorithmic capability but a new instrument: it is what would make the joint, condition-declared evaluation campaigns called for in Section 4.3.5 affordable to run at scale, provided the modelling prerequisite is met. This thesis notes the concept as a promising direction rather than as an established, widely validated practice, since the reviewed corpus does not contain a mature, dedicated body of photovoltaic-specific digital-twin studies comparable in depth to the converter and MPPT literatures surveyed in Chapters 2 and 3.

**Wide-bandgap semiconductor devices** (silicon carbide and gallium nitride) permit higher switching frequencies and lower conduction losses than silicon devices at comparable voltage ratings, and their adoption is recommended outright in recent converter-design reviews [12, 28]. For the MPPT loop specifically, the resulting frequency dividend can be spent in two different ways with opposite consequences: applied to shrink the input filter while holding ripple constant, it pushes the converter closer to the discontinuous-conduction boundary of Chapter 2 and makes mode changes more frequent across the operating window; applied instead to reduce ripple at constant filter size, it lowers the tracking algorithm's noise floor and permits finer, more precise perturbations. This trade-off is not uniform across the algorithm families surveyed in Chapter 3: for the perturbative and intelligent kernels, lower ripple is an unambiguous improvement in measurement quality, but for ripple-correlation-type methods, which use the converter's own

switching ripple as the signal from which the tracking gradient is extracted, reducing that ripple degrades the very signal the method depends on - a further, concrete instance of a technology trend interacting with the algorithm–converter pair rather than improving it uniformly. No source reviewed in this thesis reports a dedicated experimental study of a tracking loop's behaviour on a wide-bandgap converter stage, which is accordingly identified here as a well-defined and practically significant opening for further work rather than as an established result.

Table 4-6 summarises the three trends against the gaps identified in Section 4.3.5: which gaps each trend eases, and which it leaves untouched or widens.

Table 4-6: Emerging trends assessed against the challenges of Section 4.3.5.

| Trend | Gap eased | Gap left untouched or widened | Reference(s) |
|---|---|---|---|
| AI-enabled tracking | Nonlinearity handling; sensorless operation | Benchmark heterogeneity; data-dependence and ageing drift | [37, 65, 86, 87] |
| Digital twin / connected monitoring | Joint, factorial converter–algorithm evaluation (if the converter model exists) | Gated by the same unpublished-converter-model gap it would otherwise ease | [86, 99] |
| Wide-bandgap devices | Noise floor, if the frequency dividend is spent on ripple | New converter topologies proposed faster than their tracking behaviour is characterised | [12, 28] |

## 4.5 Conclusions

This thesis set out to provide a structured, critical bibliographic review of DC–DC converter topologies and Maximum Power Point Tracking algorithms for photovoltaic systems, with particular attention to the most recent MPPT techniques reported in the literature. Four conclusions follow from the review conducted in Chapters 1 to 4.

First, the physical origin of the tracking problem is well established and admits no shortcut: a photovoltaic generator has no intrinsic mechanism for holding itself at its maximum power point, that point moves continuously with irradiance and temperature and, under partial shading, multiplies into several local maxima of which only one is global - a condition that fundamentally divides the MPPT literature into methods that can and cannot guarantee global convergence.

Second, the DC–DC converter is not a passive, interchangeable interface but the actuator through which every tracking algorithm acts, and its properties - voltage-gain law, conduction-mode constancy, ripple, and dynamics - condition what any algorithm implemented through it can actually achieve. The high step-up converter literature has, largely independently of the tracking literature, developed an extensive set of topologies to overcome the classical boost converter's

gain ceiling, but the dynamic behaviour of these converters as MPPT actuators is comparatively under-characterised.

Third, the MPPT literature has matured along a clear trajectory—from the classical perturb-and-observe and incremental-conductance methods, through enhanced classical variants that have substantially closed the classical speed–oscillation trade-off, through intelligent (fuzzy, neural) and metaheuristic (population-based) methods that add nonlinearity handling and global-search capability, respectively, to the current frontier of hybrid, machine-learning, reinforcement-learning, model-predictive and sliding-mode methods that increasingly bring the converter's own dynamics into the control law. No single technique dominates on every performance criterion; the appropriate choice is a function of the shading environment, the required tracking speed and accuracy, and the computational and sensing budget available, as summarised in Table 4-1 and Table 4-2.

Fourth, and most consequential for future work, the literature's evidence base is strongest where converter and algorithm are evaluated together and weakest where they are not - and the latter is, on the evidence reviewed in this thesis, still the common case. Advancing the field further is therefore, on the evidence of this review, less a matter of proposing yet another tracking algorithm in isolation than of evaluating existing and new algorithms jointly with the converters that will actually carry them, under declared and, where possible, standardised operating conditions - a conclusion that follows directly from treating the photovoltaic converter and its tracking algorithm, as this thesis has argued throughout, as a single system rather than as two separately optimised parts.

## 4.6 Recommendations for Future Research

The gaps identified in Section 4.3.5 and the evidence-quality issues discussed in Section 4.3.6 translate into six concrete directions for future research. Each follows from a limitation documented in this thesis, and each would strengthen the evidence on which the choice of a converter and its tracking algorithm can be based:

1. **Factorial converter–algorithm studies.** Extend the design of the few studies that vary both the converter and the tracking algorithm under one set of conditions [47, 63], [100, 101] to the high-gain converters of Chapter 2 and to the global-search and most recent algorithms of Chapter 3, so that the ranking of each algorithm can be stated for a given converter rather than in general.
2. **Declared, common test conditions.** Report every tracking result together with its shading pattern, irradiance profile, converter and an explicit definition of the efficiency metric, so that results from different studies can be compared and aggregated; in this thesis, apparently conflicting verdicts largely resolved once these conditions were made explicit [65, 77].
3. **Long-duration hardware and field validation.** Validate the advanced and recent methods of Sections 3.3 and 3.4 on hardware, over realistic irradiance days and seasons, and on the same converter that was simulated, rather than in simulation alone [32, 65, 77].
4. **Published converter models.** Accompany each new converter topology with a validated dynamic model, the prerequisite for model predictive control, for training learning-based trackers and for building the digital twins discussed in Section 4.4 [86, 99].
5. **Safe and verified learning-based tracking.** Bound the exploration of reinforcement-learning trackers so that learning neither wastes energy nor stresses the converter, and verify claimed performance against the global maximum under partial shading - a check whose necessity is shown by the rebutted result discussed in Section 3.4.3 [37, 65, 88-90].
6. **Wide-bandgap devices in the tracking loop.** Quantify how the higher switching frequency of silicon carbide and gallium nitride devices, spent either on smaller filters or on lower ripple, shifts the conduction-mode boundary and the noise floor that limit the step size of classical trackers (Sections 2.1.2 and 3.2) [12, 28].

# REFERENCES


[1] IRENA, *Renewable Capacity Statistics 2026.* Abu Dhabi, United Arab Emirates: International Renewable Energy Agency, 2026.

[2] IEA, *Global Energy Review 2026.* Paris, France: International Energy Agency, 2026.

[3] R. L. Cummerow, "Photovoltaic Effect in p− n Junctions," *Physical Review,* vol. 95, no. 1, p. 16, 1954.

[4] D. M. Chapin, C. S. Fuller, and G. L. Pearson, "A New Silicon p-n Junction Photocell for Converting Solar Radiation into Electrical Power," *Journal of Applied Physics,* vol. 25, no. 5, pp. 676–677, 1954, doi: 10.1063/1.1721711.

[5] A. Goetzberger, C. Hebling, and H.-W. Schock, "Photovoltaic materials, history, status and outlook," *Materials science and engineering: R: Reports,* vol. 40, no. 1, pp. 1–46, 2003.

[6] W. Shockley and H. J. Queisser, "Detailed Balance Limit of Efficiency ofp-nJunction Solar Cells," *Journal of Applied Physics,* vol. 32, no. 3, pp. 510–519, 1961, doi: 10.1063/1.1736034.

[7] S. A. Gorji, H. G. Sahebi, M. Ektesabi, and A. B. Rad, "Topologies and Control Schemes of Bidirectional DC–DC Power Converters: An Overview," *IEEE Access,* vol. 7, pp. 117997–118019, 2019, doi: 10.1109/access.2019.2937239.

[8] J. Pastuszak and P. Wegierek, "Photovoltaic Cell Generations and Current Research Directions for Their Development," *Materials (Basel),* vol. 15, no. 16, Aug 12 2022, doi: 10.3390/ma15165542.

[9] K. K. Ng and S. M. Sze, *Physics of semiconductor devices*. Wiley-Interscience Hoboken, NJ, 2007.

[10] S. Reis-Dennis, "Review of Rethinking Health Care Ethics by Stephen Scher and Kasia Kozlowska : Palgrave Macmillan, available open access: https://link.springer.com/content/pdf/10.1007/978-981-13-0830-7.pdf," *Monash Bioeth Rev,* vol. 38, no. 1, pp. 83–86, May 2020, doi: 10.1007/s40592-020-00107-z.

[11] H. Bergveld *et al.*, "Module-level DC/DC conversion for photovoltaic systems," in *2011 IEEE 33rd International Telecommunications Energy Conference (INTELEC)*, 2011: IEEE, pp. 1–9.

[12] Martin A. Green *et al.*, "Solar Cell Efficiency Tables (Version 67)," *Progress in Photovoltaics: Research and Applications,* vol. 34, no. 4, pp. 482–496, 2026, doi: 10.1002/pip.70068.

[13] M. G. Villalva, J. R. Gazoli, and E. R. Filho, "Comprehensive Approach to Modeling and Simulation of Photovoltaic Arrays," *IEEE Transactions on Power Electronics,* vol. 24, no. 5, pp. 1198–1208, 2009, doi: 10.1109/tpel.2009.2013862.

[14] W. De Soto, S. A. Klein, and W. A. Beckman, "Improvement and validation of a model for photovoltaic array performance," *Solar Energy,* vol. 80, no. 1, pp. 78–88, 2006, doi: 10.1016/j.solener.2005.06.010.

[15] K. Ishaque, Z. Salam, and H. Taheri, "Simple, fast and accurate two-diode model for photovoltaic modules," *Solar Energy Materials and Solar Cells,* vol. 95, no. 2, pp. 586–594, 2011, doi: 10.1016/j.solmat.2010.09.023.

[16] M. C. Cavalcanti, F. Bradaschia, A. J. do Nascimento, G. M. S. Azevedo, and E. J. Barbosa, "Hybrid Maximum Power Point Tracking Technique for PV Modules Based on a Double-Diode Model," *IEEE Transactions on Industrial Electronics,* vol. 68, no. 9, pp. 8169–8181, 2021, doi: 10.1109/tie.2020.3009592.

[17] A. Safari and S. Mekhilef, "Simulation and Hardware Implementation of Incremental Conductance MPPT With Direct Control Method Using Cuk Converter," *IEEE Transactions on Industrial Electronics,* vol. 58, no. 4, pp. 1154–1161, 2011, doi: 10.1109/tie.2010.2048834.

[18] W. Xiao, N. Ozog, and W. G. Dunford, "Topology Study of Photovoltaic Interface for Maximum Power Point Tracking," *IEEE Transactions on Industrial Electronics,* vol. 54, no. 3, pp. 1696–1704, 2007, doi: 10.1109/tie.2007.894732.

[19] E. Duran, M. Piliougine, M. Sidrach-de-Cardona, J. Galan, and J. Andujar, "Different methods to obtain the I–V curve of PV modules: A review," in *2008 33rd IEEE Photovoltaic Specialists Conference*, 2008: IEEE, pp. 1–6.

[20] E. Karatepe, M. Boztepe, and M. Çolak, "Development of a suitable model for characterizing photovoltaic arrays with shaded solar cells," *Solar Energy,* vol. 81, no. 8, pp. 977–992, 2007, doi: 10.1016/j.solener.2006.12.001.

[21] A. Woyte, J. Nijs, and R. Belmans, "Partial shadowing of photovoltaic arrays with different system configurations: literature review and field test results," *Solar Energy,* vol. 74, no. 3, pp. 217–233, 2003, doi: 10.1016/s0038-092x(03)00155-5.

[22] A. Dolara, G. C. Lazaroiu, S. Leva, and G. Manzolini, "Experimental investigation of partial shading scenarios on PV (photovoltaic) modules," *Energy,* vol. 55, pp. 466–475, 2013, doi: 10.1016/j.energy.2013.04.009.

[23] A. Mohapatra, B. Nayak, P. Das, and K. B. Mohanty, "A review on MPPT techniques of PV system under partial shading condition," *Renewable and Sustainable Energy Reviews,* vol. 80, pp. 854–867, 2017, doi: 10.1016/j.rser.2017.05.083.

[24] K. Ishaque and Z. Salam, "A review of maximum power point tracking techniques of PV system for uniform insolation and partial shading condition," *Renewable and Sustainable Energy Reviews,* vol. 19, pp. 475–488, 2013, doi: 10.1016/j.rser.2012.11.032.

[25] S. J. Chiang, S. Hsin-Jang, and C. Ming-Chieh, "Modeling and Control of PV Charger System With SEPIC Converter," *IEEE Transactions on Industrial Electronics,* vol. 56, no. 11, pp. 4344–4353, 2009, doi: 10.1109/tie.2008.2005144.

[26] R. K. Akikur, R. Saidur, H. W. Ping, and K. R. Ullah, "Comparative study of stand-alone and hybrid solar energy systems suitable for off-grid rural electrification: A review," *Renewable and Sustainable Energy Reviews,* vol. 27, pp. 738–752, 2013, doi: 10.1016/j.rser.2013.06.043.

[27] C. Levis, C. O'Loughlin, T. O'Donnell, and M. Hill, "A comprehensive state-space model of two-stage grid-connected PV systems in transient network analysis," *International Journal of Electrical Power & Energy Systems,* vol. 110, pp. 441–453, 2019, doi: 10.1016/j.ijepes.2019.03.032.

[28] M. Z. Hossain, N. A. Rahim, and J. a. l. Selvaraj, "Recent progress and development on power DC-DC converter topology, control, design and applications: A review," *Renewable and Sustainable Energy Reviews,* vol. 81, pp. 205–230, 2018, doi: 10.1016/j.rser.2017.07.017.

[29] L. Quan and P. Wolfs, "A Review of the Single Phase Photovoltaic Module Integrated Converter Topologies With Three Different DC Link Configurations," *IEEE Transactions on Power Electronics,* vol. 23, no. 3, pp. 1320–1333, 2008, doi: 10.1109/tpel.2008.920883.

[30] F. Nejabatkhah, S. Danyali, S. H. Hosseini, M. Sabahi, and S. M. Niapour, "Modeling and Control of a New Three-Input DC–DC Boost Converter for Hybrid PV/FC/Battery Power System," *IEEE Transactions on Power Electronics,* vol. 27, no. 5, pp. 2309–2324, 2012, doi: 10.1109/tpel.2011.2172465.

[31] N. Mohan, T. M. Undeland, and W. P. Robbins, *Power electronics: converters, applications, and design*. John wiley & sons, 2003.

[32] K. V. G. Raghavendra *et al.*, "A Comprehensive Review of DC–DC Converter Topologies and Modulation Strategies with Recent Advances in Solar Photovoltaic Systems," *Electronics,* vol. 9, no. 1, 2019, doi: 10.3390/electronics9010031.

[33] F. Mumtaz, N. Zaihar Yahaya, S. Tanzim Meraj, B. Singh, R. Kannan, and O. Ibrahim, "Review on non-isolated DC-DC converters and their control techniques for renewable energy applications," *Ain Shams Engineering Journal,* vol. 12, no. 4, pp. 3747–3763, 2021, doi: 10.1016/j.asej.2021.03.022.

[34] M. Forouzesh, Y. P. Siwakoti, S. A. Gorji, F. Blaabjerg, and B. Lehman, "Step-Up DC–DC Converters: A Comprehensive Review of Voltage-Boosting Techniques, Topologies, and Applications," *IEEE Transactions on Power Electronics,* vol. 32, no. 12, pp. 9143–9178, 2017, doi: 10.1109/tpel.2017.2652318.

[35] T. Sutikno, H. S. Purnama, N. S. Widodo, S. Padmanaban, and M. R. Sahid, "A review on non-isolated low-power DC–DC converter topologies with high output gain for solar photovoltaic system applications," *Clean Energy,* vol. 6, no. 4, pp. 557–572, 2022, doi: 10.1093/ce/zkac037.

[36] I. Alhurayyis, A. Elkhateb, and J. Morrow, "Isolated and nonisolated DC-to-DC converters for medium-voltage DC networks: A review," *IEEE Journal of Emerging and Selected Topics in Power Electronics,* vol. 9, no. 6, pp. 7486–7500, 2020.

[37] X.-F. Cheng, C. Liu, D. Wang, and Y. Zhang, "State-of-the-Art Review on Soft-Switching Technologies for Non-Isolated DC-DC Converters," *IEEE Access,* vol. 9, pp. 119235–119249, 2021, doi: 10.1109/access.2021.3107861.

[38] W. Li and X. He, "Review of Nonisolated High-Step-Up DC/DC Converters in Photovoltaic Grid-Connected Applications," *IEEE Transactions on Industrial Electronics,* vol. 58, no. 4, pp. 1239–1250, 2011, doi: 10.1109/tie.2010.2049715.

[39] Y. Koç, Y. Birbir, and H. Bodur, "Non-isolated high step-up DC/DC converters – An overview," *Alexandria Engineering Journal,* vol. 61, no. 2, pp. 1091–1132, 2022, doi: 10.1016/j.aej.2021.06.071.

[40] M. Killi and S. Samanta, "Modified Perturb and Observe MPPT Algorithm for Drift Avoidance in Photovoltaic Systems," *IEEE Transactions on Industrial Electronics,* vol. 62, no. 9, pp. 5549–5559, 2015, doi: 10.1109/tie.2015.2407854.

[41] N. Kumar, I. Hussain, B. Singh, and B. K. Panigrahi, "Framework of Maximum Power Extraction From Solar PV Panel Using Self Predictive Perturb and Observe Algorithm," *IEEE Transactions on Sustainable Energy,* vol. 9, no. 2, pp. 895–903, 2018, doi: 10.1109/tste.2017.2764266.

[42] A. M. Noman, H. S. Sheikh, A. F. Murtaza, S. Z. Almutairi, M. H. Alqahtani, and A. S. Aljumah, "Maximum Power Point Tracking Algorithm of Photo-Voltaic Array through Determination of Boost Converter Conduction Mode," *Applied Sciences,* vol. 13, no. 14, 2023, doi: 10.3390/app13148033.

[43] D. Baimel, S. Tapuchi, Y. Levron, and J. Belikov, "Improved Fractional Open Circuit Voltage MPPT Methods for PV Systems," *Electronics,* vol. 8, no. 3, 2019, doi: 10.3390/electronics8030321.

[44] A. Elkhateb, N. Abd Rahim, J. Selvaraj, and B. W. Williams, "DC-to-DC converter with low input current ripple for maximum photovoltaic power extraction," *IEEE Transactions on Industrial Electronics,* vol. 62, no. 4, pp. 2246–2256, 2014.

[45] N. D. Benavides and P. L. Chapman, "Modeling the effect of voltage ripple on the power output of photovoltaic modules," *IEEE Transactions on Industrial Electronics,* vol. 55, no. 7, pp. 2638–2643, 2008, doi: 10.1109/tie.2008.921442.

[46] X. Li, H. Wen, L. Jiang, W. Xiao, Y. Du, and C. Zhao, "An Improved MPPT Method for PV System With Fast-Converging Speed and Zero Oscillation," *IEEE Transactions on Industry Applications,* vol. 52, no. 6, pp. 5051–5064, 2016, doi: 10.1109/tia.2016.2599899.

[47] J. L. Seguel, S. I. Seleme, and L. M. F. Morais, "Comparative Study of Buck-Boost, SEPIC, Cuk and Zeta DC-DC Converters Using Different MPPT Methods for Photovoltaic Applications," *Energies,* vol. 15, no. 21, 2022, doi: 10.3390/en15217936.

[48] M. Cacciato, A. Consoli, R. Attanasio, and F. Gennaro, "Soft-Switching Converter With HF Transformer for Grid-Connected Photovoltaic Systems," *IEEE Transactions on Industrial Electronics,* vol. 57, no. 5, pp. 1678–1686, 2010, doi: 10.1109/tie.2009.2032201.

[49] W. Luo *et al.*, "Potential-induced degradation in photovoltaic modules: a critical review," *Energy & Environmental Science,* vol. 10, no. 1, pp. 43–68, 2017, doi: 10.1039/c6ee02271e.

[50] A. M. Latham, R. Pilawa-Podgurski, K. M. Odame, and C. R. Sullivan, "Analysis and optimization of maximum power point tracking algorithms in the presence of noise," *IEEE Transactions on Power Electronics,* vol. 28, no. 7, pp. 3479–3494, 2012.

[51] K. S. Tey and S. Mekhilef, "Modified incremental conductance MPPT algorithm to mitigate inaccurate responses under fast-changing solar irradiation level," *Solar Energy,* vol. 101, pp. 333–342, 2014, doi: 10.1016/j.solener.2014.01.003.

[52] T. Sutikno, A. S. Samosir, R. A. Aprilianto, H. S. Purnama, W. Arsadiando, and S. Padmanaban, "Advanced DC–DC converter topologies for solar energy harvesting applications: a review," *Clean Energy,* vol. 7, no. 3, pp. 555–570, 2023, doi: 10.1093/ce/zkad003.

[53] D.-Y. Jung, Y.-H. Ji, S.-H. Park, Y.-C. Jung, and C.-Y. Won, "Interleaved Soft-Switching Boost Converter for Photovoltaic Power-Generation System," *IEEE Transactions on Power Electronics,* vol. 26, no. 4, pp. 1137–1145, 2011, doi: 10.1109/tpel.2010.2090948.

[54] B. Axelrod, Y. Berkovich, and A. Ioinovici, "Switched-Capacitor/Switched-Inductor Structures for Getting Transformerless Hybrid DC–DC PWM Converters," *IEEE Transactions on Circuits and Systems I: Regular Papers,* vol. 55, no. 2, pp. 687–696, 2008, doi: 10.1109/tcsi.2008.916403.

[55] A. Alkhaldi, A. Elkhateb, and D. Laverty, "Voltage lifting techniques for non-isolated dc/dc converters," *Electronics,* vol. 12, no. 3, p. 718, 2023.

[56] Y.-P. Hsieh, J.-F. Chen, T.-J. Liang, and L.-S. Yang, "Novel High Step-Up DC–DC Converter With Coupled-Inductor and Switched-Capacitor Techniques," *IEEE Transactions on Industrial Electronics,* vol. 59, no. 2, pp. 998–1007, 2012, doi: 10.1109/tie.2011.2151828.

[57] A. Imanlou, E. S. Najmi, R. Behkam, M. Nazari-Heris, and G. B. Gharehpetian, "A New High Voltage Gain Active Switched-Inductor Based High Step-Up DC–DC Converter With Coupled-Inductor," *IEEE Access,* vol. 11, pp. 56749–56765, 2023, doi: 10.1109/access.2023.3283471.

[58] A. Amir, A. Amir, H. S. Che, A. Elkhateb, and N. A. Rahim, "Comparative analysis of high voltage gain DC-DC converter topologies for photovoltaic systems," *Renewable Energy,* vol. 136, pp. 1147–1163, 2019, doi: 10.1016/j.renene.2018.09.089.

[59] K.-C. Tseng, C.-C. Huang, and C.-A. Cheng, "A High Step-Up Converter With Voltage-Multiplier Modules for Sustainable Energy Applications," *IEEE Journal of Emerging and Selected Topics in Power Electronics,* vol. 3, no. 4, pp. 1100–1108, 2015, doi: 10.1109/jestpe.2015.2404943.

[60] B. York, W. Yu, and J.-S. Lai, "An Integrated Boost Resonant Converter for Photovoltaic Applications," *IEEE Transactions on Power Electronics,* vol. 28, no. 3, pp. 1199–1207, 2013, doi: 10.1109/tpel.2012.2207127.

[61] N. Femia, G. Petrone, G. Spagnuolo, and M. Vitelli, "Optimization of Perturb and Observe Maximum Power Point Tracking Method," *IEEE Transactions on Power Electronics,* vol. 20, no. 4, pp. 963–973, 2005, doi: 10.1109/tpel.2005.850975.

[62] A. Forsyth and S. Mollov, "Modelling and control of DC-DC converters," *Power Engineer,* vol. 12, no. 5, pp. 229–236, 1998.

[63] J. S. L. Johnsana and R. S. Kumar, "Optimizing solar energy for EVs with advanced converters and MPPT," *Electric Power Systems Research,* vol. 256, 2026, doi: 10.1016/j.epsr.2026.112905.

[64] S. Mohanty, B. Subudhi, and P. K. Ray, "A Grey Wolf-Assisted Perturb & Observe MPPT Algorithm for a PV System," *IEEE Transactions on Energy Conversion,* vol. 32, no. 1, pp. 340–347, 2017, doi: 10.1109/tec.2016.2633722.

[65] M. L. Katche, A. B. Makokha, S. O. Zachary, and M. S. Adaramola, "A Comprehensive Review of Maximum Power Point Tracking (MPPT) Techniques Used in Solar PV Systems," *Energies,* vol. 16, no. 5, 2023, doi: 10.3390/en16052206.

[66] S. Motahhir, A. El Hammoumi, and A. El Ghzizal, "The most used MPPT algorithms: Review and the suitable low-cost embedded board for each algorithm," *Journal of Cleaner Production,* vol. 246, 2020, doi: 10.1016/j.jclepro.2019.118983.

[67] S. Jiang, D. Cao, Y. Li, and F. Z. Peng, "Grid-Connected Boost-Half-Bridge Photovoltaic Microinverter System Using Repetitive Current Control and Maximum Power Point Tracking," *IEEE Transactions on Power Electronics,* vol. 27, no. 11, pp. 4711–4722, 2012, doi: 10.1109/tpel.2012.2183389.

[68] S. B. Kjær, "Evaluation of the “Hill Climbing” and the “Incremental Conductance” Maximum Power Point Trackers for Photovoltaic Power Systems," *IEEE Transactions on Energy Conversion,* vol. 27, no. 4, pp. 922–929, 2012, doi: 10.1109/tec.2012.2218816.

[69] S. Lyden and M. E. Haque, "Maximum Power Point Tracking techniques for photovoltaic systems: A comprehensive review and comparative analysis," *Renewable and Sustainable Energy Reviews,* vol. 52, pp. 1504–1518, 2015, doi: 10.1016/j.rser.2015.07.172.

[70] M. A. Elgendy, B. Zahawi, and D. J. Atkinson, "Assessment of the Incremental Conductance Maximum Power Point Tracking Algorithm," *IEEE Transactions on Sustainable Energy,* vol. 4, no. 1, pp. 108–117, 2013, doi: 10.1109/tste.2012.2202698.

[71] M. A. Elgendy, B. Zahawi, and D. J. Atkinson, "Comparison of Directly Connected and Constant Voltage Controlled Photovoltaic Pumping Systems," *IEEE Transactions on Sustainable Energy,* vol. 1, no. 3, pp. 184–192, 2010, doi: 10.1109/tste.2010.2052936.

[72] H. A. Sher, A. F. Murtaza, A. Noman, K. E. Addoweesh, K. Al-Haddad, and M. Chiaberge, "A New Sensorless Hybrid MPPT Algorithm Based on Fractional Short-Circuit Current Measurement and P&O MPPT," *IEEE Transactions on Sustainable Energy,* vol. 6, no. 4, pp. 1426–1434, 2015, doi: 10.1109/tste.2015.2438781.

[73] K. Ishaque, Z. Salam, M. Amjad, and S. Mekhilef, "An Improved Particle Swarm Optimization (PSO)–Based MPPT for PV With Reduced Steady-State Oscillation," *IEEE Transactions on Power Electronics,* vol. 27, no. 8, pp. 3627–3638, 2012, doi: 10.1109/tpel.2012.2185713.

[74] M. Fannakh, M. L. Elhafyani, and S. Zouggar, "Hardware implementation of the fuzzy logic MPPT in an Arduino card using a Simulink support package for PV application," *IET Renewable Power Generation,* vol. 13, no. 3, pp. 510–518, 2018, doi: 10.1049/iet-rpg.2018.5667.

[75] T. Sutikno, A. C. Subrata, and A. Elkhateb, "Evaluation of Fuzzy Membership Function Effects for Maximum Power Point Tracking Technique of Photovoltaic System," *IEEE Access,* vol. 9, pp. 109157–109165, 2021, doi: 10.1109/access.2021.3102050.

[76] M. Veerachary, T. Senjyu, and K. Uezato, "Neural-network-based maximum-power-point tracking of coupled-inductor interleaved-boost-converter-supplied pv system using fuzzy controller," *IEEE Transactions on Industrial Electronics,* vol. 50, no. 4, pp. 749–758, 2003, doi: 10.1109/tie.2003.814762.

[77] K. Kaced, C. Larbes, N. Ramzan, M. Bounabi, and Z. e. Dahmane, "Bat algorithm based maximum power point tracking for photovoltaic system under partial shading conditions," *Solar Energy,* vol. 158, pp. 490–503, 2017, doi: 10.1016/j.solener.2017.09.063.

[78] A. Messai, A. Mellit, A. Guessoum, and S. A. Kalogirou, "Maximum power point tracking using a GA optimized fuzzy logic controller and its FPGA implementation," *Solar Energy,* vol. 85, no. 2, pp. 265–277, 2011, doi: 10.1016/j.solener.2010.12.004.

[79] L. L. Jiang, D. L. Maskell, and J. C. Patra, "A novel ant colony optimization-based maximum power point tracking for photovoltaic systems under partially shaded conditions," *Energy and Buildings,* vol. 58, pp. 227–236, 2013, doi: 10.1016/j.enbuild.2012.12.001.

[80] J. Ahmed and Z. Salam, "A Maximum Power Point Tracking (MPPT) for PV system using Cuckoo Search with partial shading capability," *Applied Energy,* vol. 119, pp. 118–130, 2014, doi: 10.1016/j.apenergy.2013.12.062.

[81] Y.-P. Huang, M.-Y. Huang, and C.-E. Ye, "A Fusion Firefly Algorithm With Simplified Propagation for Photovoltaic MPPT Under Partial Shading Conditions," *IEEE Transactions on Sustainable Energy,* vol. 11, no. 4, pp. 2641–2652, 2020, doi: 10.1109/tste.2020.2968752.

[82] G. Li, Y. Jin, M. W. Akram, X. Chen, and J. Ji, "Application of bio-inspired algorithms in maximum power point tracking for PV systems under partial shading conditions – A review," *Renewable and Sustainable Energy Reviews,* vol. 81, pp. 840–873, 2018, doi: 10.1016/j.rser.2017.08.034.

[83] A. Kheldoun, R. Bradai, R. Boukenoui, and A. Mellit, "A new Golden Section method-based maximum power point tracking algorithm for photovoltaic systems," *Energy Conversion and Management,* vol. 111, pp. 125–136, 2016, doi: 10.1016/j.enconman.2015.12.039.

[84] Y. Mahmoud, M. Abdelwahed, and E. F. El-Saadany, "An Enhanced MPPT Method Combining Model-Based and Heuristic Techniques," *IEEE Transactions on Sustainable Energy,* vol. 7, no. 2, pp. 576–585, 2016, doi: 10.1109/tste.2015.2504504.

[85] R. C. N. Pilawa-Podgurski and D. J. Perreault, "Submodule Integrated Distributed Maximum Power Point Tracking for Solar Photovoltaic Applications," *IEEE Transactions on Power Electronics,* vol. 28, no. 6, pp. 2957–2967, 2013, doi: 10.1109/tpel.2012.2220861.

[86] C. G. Villegas-Mier, J. Rodriguez-Resendiz, J. M. Alvarez-Alvarado, H. Rodriguez-Resendiz, A. M. Herrera-Navarro, and O. Rodriguez-Abreo, "Artificial Neural Networks in MPPT Algorithms for Optimization of Photovoltaic Power Systems: A Review," *Micromachines (Basel),* vol. 12, no. 10, Oct 17 2021, doi: 10.3390/mi12101260.

[87] P. Agrawal, H. O. Bansal, A. R. Gautam, O. P. Mahela, and B. Khan, "Transformer-based time series prediction of the maximum power point for solar photovoltaic cells," *Energy Science & Engineering,* vol. 10, no. 9, pp. 3397–3410, 2022, doi: 10.1002/ese3.1226.

[88] S. A. Fayaz, S. Jahangeer Sidiq, M. Zaman, and M. A. Butt, "Machine learning: An introduction to reinforcement learning," *Machine learning and data science: Fundamentals and applications,* pp. 1–22, 2022.

[89] L. Avila, M. De Paula, M. Trimboli, and I. Carlucho, "Deep reinforcement learning approach for MPPT control of partially shaded PV systems in Smart Grids," *Applied Soft Computing,* vol. 97, 2020, doi: 10.1016/j.asoc.2020.106711.

[90] V. Jaiswal, A. Wadehra, S. Bhalla, K. P. S. Rana, and V. Kumar, "Comment on “Deep reinforcement learning approach for MPPT control of partially shaded PV systems in Smart Grids”," *Applied Soft Computing,* vol. 146, 2023, doi: 10.1016/j.asoc.2023.110577.

[91] S. Kouro, P. Cortes, R. Vargas, U. Ammann, and J. Rodriguez, "Model Predictive Control—A Simple and Powerful Method to Control Power Converters," *IEEE Transactions on Industrial Electronics,* vol. 56, no. 6, pp. 1826–1838, 2009, doi: 10.1109/tie.2008.2008349.

[92] P. E. Kakosimos and A. G. Kladas, "Implementation of photovoltaic array MPPT through fixed step predictive control technique," *Renewable Energy,* vol. 36, no. 9, pp. 2508–2514, 2011, doi: 10.1016/j.renene.2011.02.021.

[93] M. B. Shadmand, R. S. Balog, and H. Abu-Rub, "Model Predictive Control of PV Sources in a Smart DC Distribution System: Maximum Power Point Tracking and Droop Control," *IEEE Transactions on Energy Conversion,* vol. 29, no. 4, pp. 913–921, 2014, doi: 10.1109/tec.2014.2362934.

[94] O. Abdel-Rahim and H. Wang, "A new high gain DC-DC converter with model-predictive-control based MPPT technique for photovoltaic systems," *CPSS Transactions on Power Electronics and Applications,* vol. 5, no. 2, pp. 191–200, 2020.

[95] M. Ahmed, I. Harbi, C. M. Hackl, R. Kennel, J. Rodriguez, and M. Abdelrahem, "Maximum power point tracking-based model predictive control with reduced sensor count for PV applications," *IET Renewable Power Generation,* vol. 19, no. 1, 2022, doi: 10.1049/rpg2.12535.

[96] T. Siew-Chong, Y. M. Lai, and C. K. Tse, "General Design Issues of Sliding-Mode Controllers in DC–DC Converters," *IEEE Transactions on Industrial Electronics,* vol. 55, no. 3, pp. 1160–1174, 2008, doi: 10.1109/tie.2007.909058.

[97] M. R. Mostafa, N. H. Saad, and A. A. El-sattar, "Tracking the maximum power point of PV array by sliding mode control method," *Ain Shams Engineering Journal,* vol. 11, no. 1, pp. 119–131, 2020, doi: 10.1016/j.asej.2019.09.003.

[98] N. Tiwary, V. Naik N, A. K. Panda, A. Narendra, and R. K. Lenka, "A Robust Voltage Control of DAB Converter With Super-Twisting Sliding Mode Approach," *IEEE Journal of Emerging and Selected Topics in Industrial Electronics,* vol. 4, no. 1, pp. 288–298, 2023, doi: 10.1109/jestie.2022.3227007.

[99] P. J. Hueros-Barrios *et al.*, "Digital twin approach for fault diagnosis in photovoltaic plant DC–DC converters," *Sensors,* vol. 25, no. 14, p. 4323, 2025.

[100] A. Raj, S. R. Arya, and J. Gupta, "Solar PV array-based DC–DC converter with MPPT for low power applications," *Renewable Energy Focus,* vol. 34, pp. 109–119, 2020, doi: 10.1016/j.ref.2020.05.003.

[101] L. A. Soriano, P. Ponce, and A. Molina, "Analysis of DC-DC converters for photovoltaic applications based on conventional MPPT algorithms," in *2017 14th International Conference on Electrical Engineering, Computing Science and Automatic Control (CCE),* Mexico City, Mexico, Sep. 20–22, 2017.

[102] K. Akter, S. M. A. Motakabeer, A. H. M. Zahirul Alam, S. H. B. Yusoff, R. K. Pachauri, H. Malik, and V. K. Jadoun, "A novel MPPT approach for photovoltaic system using Pelican optimization and high-gain DC–DC converter," *Scientific Reports,* vol. 15, art. no. 40451, 2025, doi: 10.1038/s41598-025-24000-z.

[103] IEA, *Renewables 2025: Analysis and Forecasts to 2030.* Paris, France: International Energy Agency, 2025.

[104] Downtowngal, "Solar panel roof 6th St," *Wikimedia Commons*, 2021. [Online]. Available: https://commons.wikimedia.org/wiki/File:Solar_panel_roof_6th_St.jpg. Licence: CC BY-SA 4.0. Accessed: Oct. 7, 2026.

[105] Roofjockey, "Commercial Solar PV," *Wikimedia Commons*, 2013. [Online]. Available: https://commons.wikimedia.org/wiki/File:Commercial_Solar_PV.jpg. Licence: CC BY-SA 4.0. Accessed: Oct. 7, 2026.

[106] N. Y. Barclay, U.S. Air Force, "Giant photovoltaic array," *Wikimedia Commons*, 2007. [Online]. Available: https://commons.wikimedia.org/wiki/File:Giant_photovoltaic_array.jpg. Public domain. Accessed: Oct. 7, 2026.

[107] "1 MW 4 MWh Turner Energy Storage Project in Pullman, WA," *Wikimedia Commons*, May 22, 2015. [Online]. Available: https://commons.wikimedia.org/wiki/File:1_MW_4_MWh_Turner_Energy_Storage_Project_in_Pullman,_WA.jpg. Licence: CC BY-SA 4.0. Accessed: Oct. 7, 2026.
[108] SanTan Solar, "What kind of inverter does my solar panel system need?," *SanTan Solar Blog*, Sept. 8, 2021 (updated Jan. 14, 2026). [Online]. Available: https://www.santansolar.com/what-inverter-does-my-solar-panel-need/. Accessed: Oct. 7, 2026.
[109] SanTan Solar, "2kW panels with LV2424 off grid inverter solar kit," product page. [Online]. Available: https://www.santansolar.com/product/2kw-panels-with-lv2424-off-grid-inverter-solar-kit/. Accessed: Oct. 7, 2026.
[110] G. Vellut, "Close-up of a polycrystalline solar PV panel," *Wikimedia Commons*, 2021. [Online]. Available: https://commons.wikimedia.org/wiki/File:Close-up_of_a_polycrystalline_solar_PV_panel.jpg. Licence: CC BY 2.0. Accessed: Oct. 7, 2026.
[111] C. Domínguez, "PV module layout," *Wikimedia Commons*, 2023. [Online]. Available: https://commons.wikimedia.org/wiki/File:PV_module_layout.jpg. Licence: CC BY-SA 4.0. Accessed: Oct. 7, 2026.
[112] D. Schroeder, National Renewable Energy Laboratory, "Solar panels in the desert," *Wikimedia Commons*, 2013. [Online]. Available: https://commons.wikimedia.org/wiki/File:Solar_panels_in_the_desert.jpg. Public domain. Accessed: Oct. 7, 2026.
[113] Z. Liu, Y. Gong, Z. Wang, Y. Li, and D. Liu, "Revealing the intrinsic mechanisms of hot and cold spots within a locally shaded photovoltaic module based on micro-electrical characteristics," *Energies,* vol. 17, no. 17, art. no. 4462, 2024, doi: 10.3390/en17174462.
[114] M. Markowitz, "Enphase M190," *Wikimedia Commons*, 2011. [Online]. Available: https://commons.wikimedia.org/wiki/File:Enphase_M190.jpg. Accessed: Oct. 7, 2026.
[115] ROHM Co., Ltd., "Isolated flyback converter basics: Flyback converter operation and snubber," *TechWeb*, Jan. 28, 2016. [Online]. Available: https://techweb.rohm.com/product/power-ic/acdc/1150/. Accessed: Oct. 8, 2026.
[116] H. Li, D. Liu, and C. A. Luongo, "Investigation of potential benefits of MOSFETs hard-switching and soft-switching converters at cryogenic temperature," *IEEE Trans. Appl. Supercond.,* vol. 15, no. 2, pp. 2376–2379, Jun. 2005, doi: 10.1109/TASC.2005.849672.
[117] A. Suresh Kumar and P. Krishna Reddy, "Design & implementation of zero voltage switching buck converter," *Int. J. Eng. Res. Appl.,* vol. 4, no. 9 (Version 5), pp. 193–198, Sept. 2014.
[118] N. Hinov and T. Grigorova, "A comprehensive analysis of losses and efficiency in a buck ZCS quasi-resonant DC/DC converter," *J. Low Power Electron. Appl.,* vol. 15, no. 2, art. no. 34, 2025, doi: 10.3390/jlpea15020034.
[119] POWER4ALL, "Buck-boost converter simulation," [Online]. Available: https://power4all.in/Buck-Boost_Converter-Simulation.php. Accessed: Oct. 9, 2026.
[120] S.-Y. Tseng and J.-H. Fan, "Zeta/flyback hybrid converter for solar power applications," *Sustainability,* vol. 14, no. 5, art. no. 2924, 2022, doi: 10.3390/su14052924.
[121] G. Zhang, J. Zeng, W. Xiao, S. S. Yu, B. Zhang, and Y. Zhang, "A self-protected single-stage LLC resonant rectifier," *IEEE J. Emerg. Sel. Topics Power Electron.,* 2020, doi: 10.1109/JESTPE.2020.3024893.
[122] F. Spertino, J. Ahmad, A. Ciocia, and P. Di Leo, "A technique for tracking the global maximum power point of photovoltaic arrays under partial shading conditions," in IEEE conference proceedings, 2015, ISBN 978-1-4799-8586-9.